Title
Multiple-Quantum NMR Studies of Spin Clusters in Liquied Crystals and Zeolites

Author
Pearson, J.

Publication Date
1991-07-01

LBL-31123

Lawrence Berkeley Laboratory
UNIVERSITY OF CALIFORNIA

Materials & Chemical
Sciences Division

Multiple-Quantum NMR Studies of Spin Clusters in Liquid Crystals and Zeolites

J. Pearson
(Ph.D. Thesis)

July 1991

Prepared for the U.S. Department of Energy under Contract Number DE-AC03-76SF00098

DISCLAIMER

LBL-31123

Multiple-Quantum NMR Studies of Spin Clusters in Liquid Crystals and Zeolites

John Pearson

Department of Chemistry
University of California

and

Materials Sciences Division
Lawrence Berkeley Laboratory
University of California
Berkeley, California 94720

July 1991

This work was supported by the Director, Office of Energy Research, Office of Basic Energy Sciences, Materials Sciences Division, of the U.S. Department of Energy under Contract No. DE-AC03-76SF00098.

Contents

List of Figures

Acknowledgements

Homini sapienti magno gratias ago

I would like to express my appreciation to Professor Alex Pines for his support during my graduate studies. Alex's energy and enthusiam for all matters pertaining to science are inspirational and a joy to behold. I also wish to thank him for the number of exceptionally talented people he has attracted to Berkeley that I have interacted with.

I would like to thank Dr. Dieter Suter for introducing me to the density matrix and for getting me started in multiple-quantum NMR. I have found that increasingly more of what he said makes sense as time goes on. I would like to thank Dr. David Shykind for introducing me to NMR in general and for his technical expertise in particular. Discussions with Dr. Marianne Koenig were extremely helpful in understanding coherent averaging theory and numerical simulations of MQ NMR, in addition to learning about Luxembourg. Dr. Brad Chmelka helped me understand the wonderful world of zeolites, and Dr. Margaret Eastman built the most stable quad box ever to grace the gamma. I would especially like to thank Dr. Gerry Chingas for all the help, both technical and theoretical, he has given me.

I would like to thank the rest of the Pinenuts for their support, especially Steve Rucker and Mark Rosen for their splendid work on oriented n-alkanes. I am deeply indebted to Karl Mueller for our getting lost on some of the prettier trails in the East Bay, and to Tom Jarvie and Malaine Trecoske for our not getting lost on some of the prettier trails of the Coastal Ranges. To the forty+ Pinenuts I have not named, thanks.

Finally, I wish to thank my friends Alan and Bill and my wife Julie for their encouragement and support. I also wish to thank my parents, Bob and Helene, without whom I would not have been possible.

1

Introduction

Multi-photon transitions in nuclear magnetic resonance (NMR) experiments were observed and understood [1] soon after the first successful NMR experiments, but the continuous wave (CW) techniques available at the time were not well suited to the study of these higher order transitions. In part, this was due to the need to resort to higher order perturbation theory to understand transitions due to multi-photon processes, while single-photon processes require only first order perturbation theory. The wide applicability of single-photon CW-NMR adsorption spectra in the study of many physical systems in addition to the relative difficulty involved with observing multi-photon transitions led to muti-photon NMR being barely mentioned in both the literature and standard texts on magnetic resonance.

The advent of two dimensional (2D) Fourier transform (FT) NMR [2,3] made it possible to routinely observe the effects of multi-photon adsorption and emission by indirect observation of the multiple-quantum (MQ) coherences created by these processes. Those wishing a detailed description of 2D NMR will find it elsewhere [4,5], especially in Ernst, et al.[6]. All the experiments performed in this work are two dimensional NMR experiments in the sense that the evolution of the normally 'invisible' MQ coherences during a time t_1 are observed indirectly by the effect they haveon the single-quantum coherences detected during a latter time t_2. The experimental data is collected as a function of the Hamiltonian during only the time t_1, creating one dimensional projections of two dimensional data sets. (The last experiment described in this work differs from this description by being a two dimensional projection of a three dimensional experiment, with variable time periods t_1

and t'_1 influencing the signal detected at $t_2 = 0$, but the principle is similar.)

This work will describe the use of MQ NMR to study spin clusters in anisotropic materials. A technique known as multiple-quantum spin counting was used to determine average spin cluster sizes in liquid crystalline materials and in faujacitic zeolites containing aromatic hydrocarbons. The average number of protium nuclei per spin cluster was determined for each material, and this was used to determine the molecular distribution between the spin clusters. The first half of the thesis will describe MQ NMR and the MQ spin counting technique (chapters 2-3), and the second half of the thesis will describe the actual experiments and their results (chapters 4-6).

Chapter 2 begins with a discussion of conventional (i.e., single-quantum) NMR experiments and the relationship between these and MQ NMR experiments. The utility of both methods to study various material systems will be compared by examining the density operator ρ for spins influenced by a variety of interactions. The ability of each method to determine ρ will be used as a measure of each method's applicability to extract information from the system. The chapter ends with a discussion of the general form of a MQ NMR experiment, including a brief review of coherent averaging theory.

Chapter 3 describes the design of MQ NMR spin counting experiments, where MQ NMR is used to determine the number of spins in an isolated spin cluster. The relationship between the observed size of a spin cluster and the actual number of spins in a cluster is discussed, followed by a section describing the three pulse sequences used to perform MQ NMR spin counting experiments in this work. The final section in this chapter discusses some of the technical problems typically encountered when using this technique, and how to minimize or eliminate these problems through improvement of the apparatus and design of the experimental pulse sequence.

Chapter 4 reports the results of MQ NMR spin counting studies performed on

molecules oriented in liquid crystalline mesophases. These systems contain perfectly isolated spin clusters with high signal to noise, making them ideal test cases for the technique. A brief review of the nematic and smectic A liquid crystalline mesophases will be followed by a discussion of the expected spin cluster structures for the various experiments. The coupling of elements in the density matrix will be examined for three and four spin clusters, using an effective Hamiltonian proportional to the dipole couplings between the spins. Results for MQ NMR spin counting experiments on n-alkanes oriented in nematic p-pentyphenyl-2-chloro-(4-p-pentylbenzoyloxy)benzoate (i.e., Kodak 11650 or EK 11650) will be presented and discussed, followed by the results from experiments on spin clusters on cyanobiphenyl liquid crystal molecules in the nematic and smectic A mesophases.

Chapter 5 reports the results from MQ NMR spin counting experiments on samples containing spatially isolated spin clusters, namely protium nuclei on benzene and hexamethylbenzene molecules in NaY zeolite. The guest molecules and the zeolite matrix will be reviewed and the possible sites for guest adsorption through guest/host electrostatic interaction will be discussed. The results of experiments on NaY zeolite samples containing a range of guest concentrations for both hydrocarbons will be presented, first for hexamethylbenzene and then for benzene. The observed spin cluster sizes determined from these experiments will be used to determine the distribution modes of the two hydrocarbons between zeolite supercages.

Chapter 6 concludes this work by expressing the evolution of ρ in terms of irreducible tensor operators. The results of the previous two chapters are revisited, and an additional experiment to measure both the l and m quantum numbers of T_{lm}'s in adamantane is presented.

A final note to close this introduction. The lightest isotope of hydrogen possess the proper name of protium, which will be used throughout this work. When

the term 'hydrogen' is referred to, as in 'hydrogen site', it is to signify the element of hydrogen in all its isotopic forms. A hydrogen site may be occupied by protium, deuterium or tritium, for example. A protium site contains only protium, such as the observed hydrogen sites in the experiments described in chapters four, five and six.

2

Multiple-Quantum NMR Fundamentals

2.1 Introduction

Nuclear magnetic resonance (NMR) is the branch of spectroscopy concerned with the study of nuclear spin energy levels by the interactions between radio frequency (rf) electromagnetic radiation and nuclear spins in an external magnetic field. Originally, NMR experiments were performed by irradiating a sample of interest with weak rf radiation while varying a large external magnetic field [7-11]. Spectra were measured peak by peak as resonance conditions for the various energy level transitions were met in these continuous wave (CW) experiments. More recently, Fourier transform (FT) techniques have been widely used [12], where a short, intense rf pulse is applied to a sample in a fixed external magnetic field, which induces transverse magnetization within the sample. Fourier transformation of the signal generated by the precessing transverse magnetization generates a spectrum theoretically identical to one measured in a CW experiment [13].

The spectra measured by both methods may be referred to as single-quantum spectra. This is a consequence of photons being spin 1 particles and the principle of conservation of angular momentum. The absorption of a photon must change the z component of the spin's angular momentum by an amount equal to the z component of the photon's angular momentum (i.e., ± 1), therefore the net change in energy of the photon-spin system is zero. The possibility of multiple-photon, and hence multiple-quantum, effects appearing in a CW spectrum is eliminated by requiring weak rf irradiation. The single-quantum nature of standard CW (and the equivalent FT)

NMR spectra have led to the widespread modeling of nuclear spin ensembles as collections of two level systems, with each spectral peak corresponding to a transition between a pair of energy levels present in the sample, as depicted in Figure 2.1. Differences in the resonant frequency are explained as minor perturbations of a spin by its surroundings [14]. These differences allow for the investigation of the chemical environment at spin sites in a substance. In the limit of perfectly homogeneous magnetic fields and spins one half experiencing only minor perturbations from sources other than the external magnetic field, NMR spectra may be expressed as a series of sharp lines:

$$I(\omega) \;\alpha\; \sum_{i>j} |\langle i | I_+ | j \rangle|^2 \; \delta(\omega - \omega_{ij}) \qquad (2.1)$$

where $\delta(x)$ is the Kronecker delta function, the states $| i >$ and $| j >$ are the eigenstates of the unperturbed spin Hamiltonian, and I_+ is the angular momentum raising operator.

Although the above model of nuclear spin systems is extremely useful in the study of many different material systems, there are limitations to this model. In the case of dipole-dipole coupled spins one half (e.g. protium in solids), these limitations are exhibited by broad lines in NMR spectra, thus limiting the amount of information which can be extracted from such spectra. Experiments based upon a more accurate model would provide additional information about the system under study. This may be done by considering spins in the sample to be part of networks of coupled spins capable of absorbing and emitting more than one photon of rf radiation [15], as depicted in Figure 2.2. Observation of higher order, or multiple-quantum (MQ), transitions increases the available information, improving the utility of NMR spectroscopy for investigating materials containing strongly coupled spin systems.

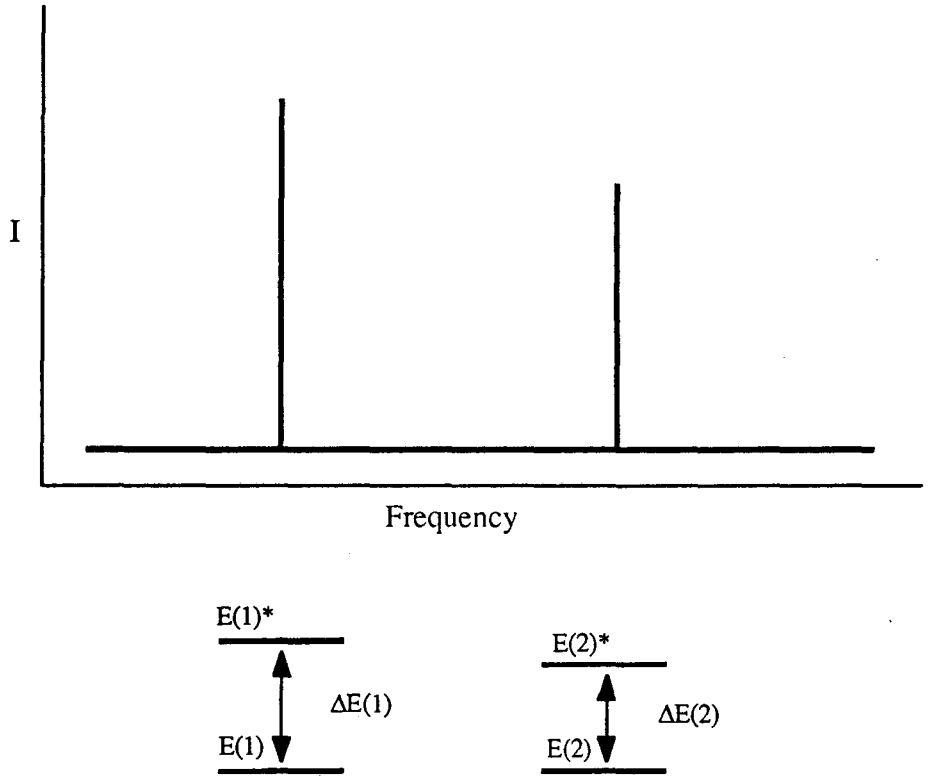

Figure 2.1. A ∂ function spectrum of a system containing two non-equivalent spin sites, 1 and 2. Each line corresponds to the energy difference in a two level system based on one spin one half.

To illustrate the applicability of single-quantum and multiple-quantum NMR to obtain information from spins under the influence of interactions arising from differing physical properties of a material, we will use a density operator formalism in the interaction picture (i.e., the 'rotating frame'). Also, experimental time scales shall be assumed to be much shorter than the spin-lattice relaxation time to allow us to ignore spin-lattice relaxation effects. Lattice temperatures will be assumed to be comparable to room temperature (i.e., 150K< T < 450K).

2.2 Models, Basis States, and The Density Operator

The following discussion on density matrix theory is intended as a brief review of the subject, with those desiring a more detailed treatment referred to any modern text on quantum mechanics, with even more thorough treatments given by Fano [16] and Blum [17].

Quantum mechanical systems are measured by extracting information from the system in the form of the eigenvalues of a set of commuting observable operators. Observation of these eigenvalues allow us to determine populations of eigenstates corresponding to the set of commuting operators. Thus, one of the requirements for the interpretation of spectra is the selection of a complete set of basis states which are eigenstates of the operators being utilized in the experiment. The selection of a set of basis states allows the expansion of a system's state vector in terms of the basis:

$$|\psi_n\rangle = \sum_m a_m^{(n)} |\phi_m\rangle \qquad (2.2)$$

where the $|\phi_m\rangle$'s represent the basis states and $a_m^{(n)}$'s the coefficients for the nth state. The selection of a set of basis states also fixes the form of the density operator, ρ:

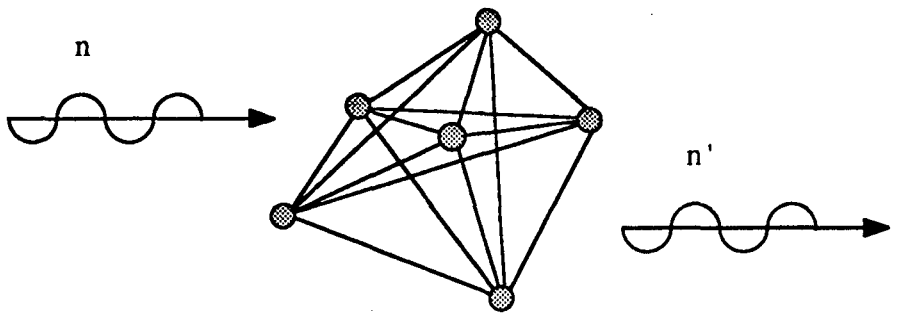

Figure 2.2. A group of spins one half, represented as shaded circles, forming a spin network capable of adsorbing n photons and emitting n' photons, where generally $n \neq n' \neq 1$. The difference in angular momentum between the n absorbed and n' emitted photons is added to the angular momentum of the spin cluster.

$$\rho = \sum_n W_n |\psi_n\rangle\langle\psi_n| = \sum_{nmm'} W_n a_m^{(n)} a_{m'}^{(n)*} |\phi_m\rangle\langle\phi_{m'}| \qquad (2.3)$$

where W_n is the statistical weight for the nth state. The density operator is often expressed as the density matrix:

$$\langle\phi_i|\rho|\phi_j\rangle = \rho_{ij} = \sum_n W_n a_i^{(n)} a_j^{(n)*} \qquad (2.4)$$

allowing visualization of ρ as a collection of elements ρ_{ij}. The density matrix may be used to find the expectation value of any operator, Q:

$$\langle Q\rangle = \frac{tr(\rho Q)}{tr\rho} \qquad (2.5)$$

where tr(x) signifies the taking of the trace of a matrix. Thus, the density matrix contains all the physically significant information concerning the system.

Standard NMR experiments [18] extract information about a substance by measuring the expectation value of the observable I_z, with:

$$I_{kz}|k\rangle = m_k|k\rangle \qquad (2.6)$$

where m_k is the z component of the kth spin's angular momentum. This limits the selection of basis states to eigenstates of the operators I and I_z. For a sample containing N spins one half, the most general basis will include 2^N eigenstates,

spanning the space of product states of N spins one half:

$$|\pm_1\rangle \otimes |\pm_2\rangle \otimes .. \otimes |\pm_N\rangle = |\pm_1 \pm_2 \ldots \pm_N\rangle \qquad (2.7)$$

where the eigenstates states of single spins one half have been designated as $|+\rangle$ and $|-\rangle$. The density matrix generated by this basis will contain 2^{2N} elements, where N will be quite large for an experimentally observable sample (i.e., $N \geq 10^{18}$ spins). Therefore, it is desirable to construct a model for the spin system which will allow us to select the smallest possible basis set necessary to adequately describe the system. The resulting reduced density matrix should retain all the physically significant information concerning the system while eliminating terms which are either irrelevant or redundant, as defined by the obsevables $\mathbf{I}$ and I_z.

As an illustration, assume collections of N spins one half under a variety of Hamiltonians in a large external magnetic field. A model will be constructed for each case, with the aim of simplifying the basis set of eigenstates of $\mathbf{I}$ and I_z needed to adequately describe the model and therefore the system. The reduced density matrix generated by the set of basis states should contain all the physically relevant information concerning the system, including time evolution of the system under various influences as described by the Liouville-von Neumann equation:

$$i\hbar \frac{\partial \rho(t)}{\partial t} = [H(t), \rho(t)] \qquad (2.8)$$

which can be derived from Schoedinger's equation. In other words, in the limit that we are able to neglect spin-lattice interactions, relaxation should be absent from our

description of the spin system. All evolution of the spin polarization should be observable in the evolution of the density matrix.

Beginning with only the Zeeman interaction, a system of containing N spins one half in a large external magnetic field can be thought of as an ensemble of two level systems, with each spin in either an "up" state or a "down" state. The energy difference between the two levels is identical for each site and is determined by the strength of the external field and the gyromagnetic ratio of the spins:

$$\Delta E = 2\mu B_0 \tag{2.9}$$

where μ is the gyromagnetic ratio and B_0 is the strength of the external field. This system's spectrum would be composed of one infinitely narrow line.

The choice of a complete basis set for the above system is obvious: an "up" state, which we shall represent as $|+\rangle$, and a "down" state, which we shall represent as $|-\rangle$. A general state vector can always be written as a linear superposition of the basis states:

$$|\psi\rangle = \sum_n a_n |\phi_n\rangle = a_1|+\rangle + a_2|-\rangle \tag{2.10}$$

where $|\phi_n\rangle$ is the nth element of the basis set. Since the basis set contains only two states, the density operator ρ is comprised of four elements:

$$\rho = \sum_{nmm'} W_n a_m^{(n)} a_{m'}^{(n)*} |\phi_m><\phi_{m'}|$$

$$= \sum_n W_n \left(a_1^{(n)} a_1^{(n)*} |+><+| + a_1^{(n)} a_2^{(n)*} |+><-| \right.$$

$$\left. + a_2^{(n)} a_1^{(n)*} |-><+| + a_2^{(n)} a_2^{(n)*} |-><-| \right) \qquad (2.11)$$

where n is the spin index and W_n is the statistical weight of the nth spin.

The density matrix is found by applying the basis set to ρ from both the left and the right, as was seen in equation 2.4:

$$<\phi_i | \rho | \phi_j> = \rho_{ij} = \sum_n W_n a_i^{(n)} a_j^{(n)*}$$

with each resulting element being the i,jth element of the density matrix in the $\{|\phi_n>\}$ representation. Basis state populations are represented by the diagonal elements of the density matrix (i=j), while the off diagonal elements ($i \neq j$) represent the amplitudes of coherent superpositions of the basis states. It is convenient to label coherent superpositions of the ith and jth basis states by the difference in the magnetic quantum numbers m between the two basis states:

$$n_{ij} = \Delta m = \frac{[\, I_z, |\phi_i><\phi_j| \,]}{|\phi_i><\phi_j|} \qquad (2.12)$$

where n_{ij} is the order of the coherence. The current example's density matrix contains two off diagonal terms and expression (2.12) labels them as ± 1 quantum coherences. The Hermitian property of the density matrix [16] indicates that these terms are of

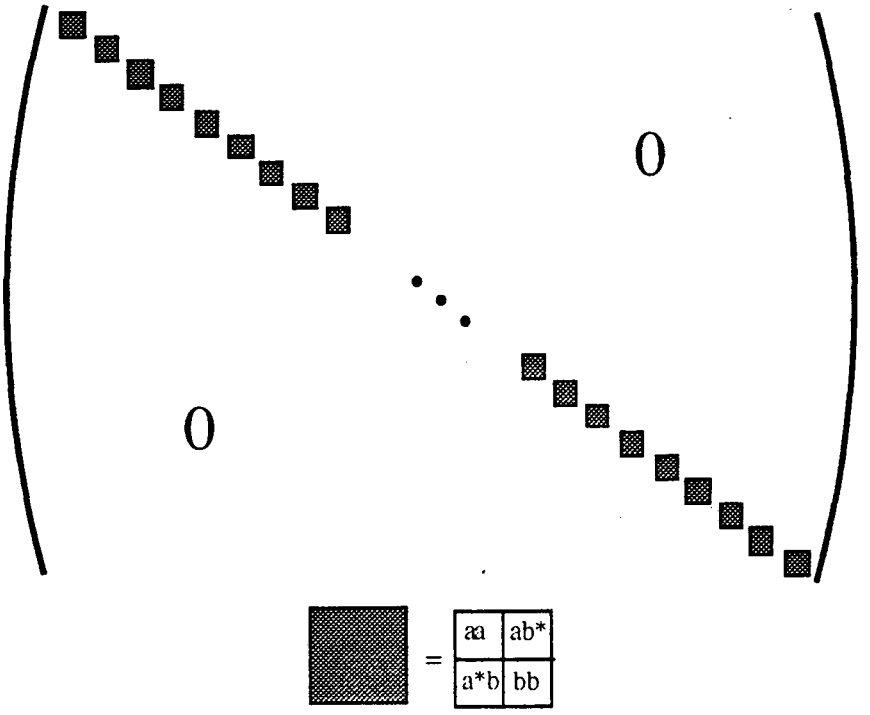

Figure 2.3. Schematic depiction of the density matrix for a collection of uncoupled spins one half. The matrix is block diagonal, with each block containing matrix elements dependent upon the state of a single spin.

equal magnitude, and FT-NMR allows the conversion of single-quantum coherence amplitudes to basis state populations by a $\pi/2$ pulse [13]. Taken together, this enables the full determination of the density matrix for the system. Full determination of the density matrix indicates that the maximum amount of information has been extracted from the system, for the density matrix contains all physically relevant information about the spin system, in this case the strength of the Zeeman interaction.

Let us now allow for a slight variation in the magnetic field strength experienced by the resonating nuclei. This effect may be caused by electronic shielding and ring current effects, collectively known as the chemical shift [14], and it may also be caused by inhomogeneities in the external magnetic field. The result in either case is to cause variation in the resonance frequency for the various elements in the spin ensemble. The system can still be accurately modeled as a collection of two level systems, for the N spin essentially density matrix is block diagonal with each block corresponding to a two level system, as depicted in Figure 2.3. Since the spins have no influence upon one another, examination of the N spin density matrix will reveal that many of the diagonal blocks are redundant, due to the 2^{N-1} possible orientations of spins which are stationary in each diagonal block. The remaining N diagonal blocks form density matrices for single spins one half, with characteristic resonance frequencies ω_i. In general, an absorption spectra of the system will reveal N infinitely narrow lines, one for each unique diagonal block. Assuming a homogeneous external magnetic field, frequency shifts from the Zeeman frequency are indicative of the electronic environment surrounding the resonating nuclei. As above, single-quantum absorption spectra can be used to fully determine the density matrix, since the system can be described as a combination of basis state populations and single-quantum coherences.

Next, let us allow weak scalar, or J, couplings between resonating spins. These couplings are propagated by electrons between resonating spins via the electron

nucleus hyperfine coupling and take the form

$$H_J = \hbar J\, \mathbf{I}_1 \cdot \mathbf{I}_2 \qquad (2.13)$$

where J is the scalar coupling constant [19]. J coupling strengths are generally on the order of a few to a few hundred hertz, usually less than one part per million of the Zeeman interaction for protium nuclei in commercially available magnets. J couplings are also short range in nature, essentially being limited to coupling spins on neighboring chemical sites, such as neighboring carbon and heteroatoms for protium in organic molecules. Therefore, the coupled spin networks generated by J couplings evolve slowly, due to weak couplings, and contain a limited number of spins, due to the short range nature of the couplings. The absence of direct dipole-dipole couplings between spins in close proximity implies isotropic motion of the small spin networks with respect to each other and isotropic tumbling of the spin networks themselves, as found for molecules in a fluid.

The choice of basis states is not as obvious as in the case without bilinear couplings, for our spin system can no longer be modeled as an ensemble of individual spins one half. We now have an ensemble of networks of N' spins one half, where N' is the number of resonant spins in each molecule. Therefore, one choice of basis would be the product states of N' spins one half,

$$|\pm_1\rangle \otimes |\pm_2\rangle \otimes \ldots \otimes |\pm_{N'}\rangle = |\pm_1\ \pm_2 \ldots \pm_{N'}\rangle \qquad (2.14)$$

which would be composed of $2^{N'}$ states. The corresponding density matrix in this representation would therefore contain $2^{2N'}$ elements, with the amplitudes of only those elements where $\Delta m = \pm 1$ being directly measurable. Fortunately, the weakness of the J

couplings indicates that elements of the density matrix other than initial populations and their rf pulse related single-quantum coherences will require a relatively long period of time to gain appreciable amplitude, on the order of many tens of milliseconds to a few seconds. Additionally, weak scalar couplings are often smaller in magnitude than chemical shift differences between nuclei [19], precluding higher order evolution due to the principle of conservation of energy. It is therefore common to treat J couplings as a minor perturbation of the resonance frequency [18], inducing a splitting pattern indicative of the J coupling strength and the number of spins immediately coupled to the site. Amplitudes of density matrix elements other than populations or single-quantum coherences are assumed to be negligible, again allowing for full determination of the density matrix using single-quantum spectra. This accounts for the great success NMR spectroscopy has enjoyed in the study of organic liquids.

Finally, isotropic motion is removed from the material. The spins in the sample may be constrained to move anisotropically, as in a liquid crystal or a "plastic-like" solid (e.g., adamantane), or we may assume rigid lattice conditions. The lack of isotropic motion in the presence of resonant spins one half in close proximity causes direct dipole-dipole couplings to dominate the interaction Hamiltonian. (The J couplings also increase in magnitude and behave in a fashion similar to dipole couplings, but generally are weaker than the dipole couplings.) In the high field limit, homonuclear dipole-dipole coupling takes the form:

$$H'_D = \sum_{k<l} \frac{\mu_0 \gamma^2 \hbar^2}{4\pi r_{kl}^3} (1 - 3\cos^2\theta_{kl}) \left(I_{kz} I_{lz} - \frac{1}{4} (I_{k+} I_{l-} + I_{k-} I_{l+}) \right) \qquad (2.15)$$

where r_{kl} is the distance between spins k and l and θ_{kl} is the angle between the

internuclear vector and the external magnetic field. The magnitude of homonuclear dipole-dipole coupling varies from vanishingly small in low gamma, isotopically dilute spin systems (e.g., carbon-13) to 50+ kilohertz for protium under rigid-lattice conditions [20] . Strong bilinear couplings between spins in a sample introduce line widths which obliterate all fine structure in a spectrum, primarily due to spin diffusion. (An alternate phrase for spin diffusion, spin-spin relaxation, has been avoided due to the connotation of irreversibility generally associated with relaxation processes.)

Choosing a set of basis states for a system of strongly coupled spins is straightforward. We must assume the product space of N' spins one half, where N' is the number of spins present in the strongly coupled spin network. A nematic liquid crystal contains strongly coupled spin networks spanning individual molecules, with N' on the order of tens of spins. A protium bearing rigid lattice contains a strongly coupled spin network spanning the entire sample, with N' being infinite for all intensive purposes. In either case, the basis contains $2^{N'}$ states, and the density matrix in this basis contains $2^{2N'}$ elements. Ordering these elements by Δm allows us to collect these elements into 2N'+1 groups (i.e., N,..., minus one, zero , one ,...,N quantum coherences), as depicted in Figure 2.4. With the exception of the $\pm N'$ coherences, each of these groups contain more than one element, with the elements in each group coupled to one another by the "flip-flop" portion of the high field dipole-dipole Hamiltonian. Coupling between elements of the same order allows polarization to diffuse between these elements during the detection period of a standard FT-NMR experiment, shortening the lifetime of each individual coherent superposition of state. The exchange of amplitude between elements in the ± 1 quantum coherence groups is the source of the line broadening observed in the single-quantum spectrum.

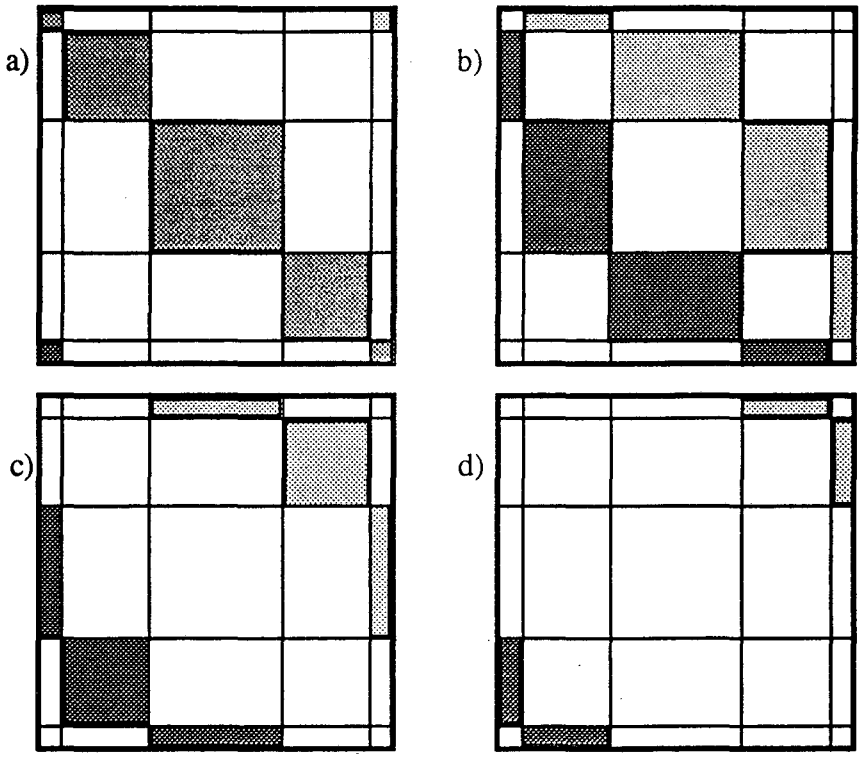

Figure 2.4. Schematic representations of the density matrix for a four spin one half system with elements highlighted by order n. The darkest shading is for $n < 0$ and the lightest shading is for $n > 0$. The nine element groups are highlighted on four copies of the matrix representation for clarity, with a) highlighting $n = 0, \pm 4$, b) highlighting $n = \pm 1$, c) highlighting $n = \pm 2$, and d) highlighting $n = \pm 3$. Elements of the same order n are linked via spin diffusion. Basis states are ranked by quantum number l, from highest to lowest.

The high field homonuclear dipole-dipole Hamiltonian does not allow couplings between density matrix elements of different orders due to the truncation of the dipole-dipole Hamiltonian by the external magnetic field, which is due to the Zeeman interaction energy still being several orders of magnitude greater than the homonuclear dipole-dipole interaction energy.

Couplings between elements of different order can be established by the use of strong rf radiation. Indeed, the first observations of the evolution of higher order coherent superpositions of state were made in CW-NMR experiments when the rf radiation power level was increased [1]. The use of strong rf pulses indicates the routine excitation of unobserved higher order coherences in FT-NMR experiments involving samples with bilinear couplings between spins. As shown below, these 'multiple-quantum' coherences can be indirectly observed by employing two dimensional spectral acquisition techniques.

The indirect observation of higher order coherences theoretically allows the measurement of each element of the density matrix and therefore the extraction of all physically significant information concerning the system. Observation of multiple-quantum coherences is particularly useful in the study of bilinear couplings, since the non-zero amplitude of higher order coherences is a direct consequence of these couplings.

2.3 Excitation, Evolution, and Detection of All Orders of Coherence

The directly observed signal in FT-NMR experiments is limited to image currents caused by single-quantum coherent superpositions of state. The coil geometry prevents the spectrometer from detecting any higher order coherences. Theoretically, one could directly detect any order coherence by constructing a coil with the proper symmetry, but the coil would detect only coherences of one particular order n_i and

generally would not be capable of producing rf pulses. It would be necessary to nest n coils of differing symmetries to detect n orders of coherence, where n is generally a large number.

The addition of a second spectral dimension allows us to indirectly detect all orders of coherence while directly observing only single-quantum coherences. Inclusion of a second evolution time in pulsed NMR experiments and the use of a two dimensional Fourier transform to obtain a two dimensional spectra was suggested shortly after the advent pulsed NMR [2], and has been used in many different applications in the intervening years [6]. In our case, the use of two evolution periods allows evolution of 'invisible' modes in the first period to be observed by their effect on the single-quantum signal detected in the second period. Fourier transformation in the first dimension will generate multiple-quantum spectra, while Fourier transformation in the second dimension will generate single-quantum spectra.

In general, multiple-quantum Fourier transform NMR (MQ-NMR) experiments can be divided into four time periods: preparation (τ), evolution (t_1), mixing (τ'), and detection (t_2), as depicted in Figure 2.5. Multiple-quantum coherences are created during the preparation period, evolve during the evolution period, undergo a second period of excitation during the mixing period, and indirectly detected by observation of the single-quantum coherences during the detection period. Details concerning particular sequences depend upon exactly what interactions and orders of coherence one wishes to study. Sequences can be designed to be order selective [21], to minimize particular experimental artifacts, to simplify spectra by eliminating parts of the Hamiltonian [22], or combinations of the above. For now, we will limit discussion to MQ-NMR experiments in general. Specific pulse sequences will be discussed in the next chapter.

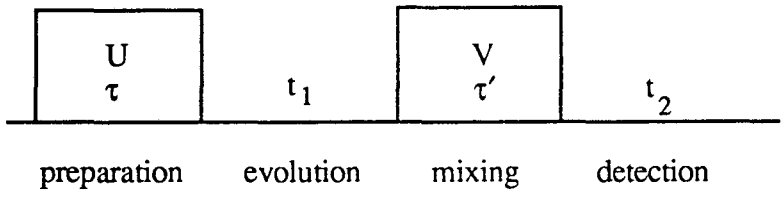

Figure 2.5. A schematic diagram of the generalized multiple-quantum experiment. MQ coherences are excited during the prepation period, interact with their environment during the evolution period, are converted into observable modes during the mixing period, and indirectly detected during the detection period. The propagator U determines the order selectivity of the excitation, and the propagator V determines the efficiency of the conversion between invisible modes and visible modes.

2.3.1 Excitation

Excitation of multiple-quantum coherences occurs during both the preparation and mixing periods of a generalized MQ experiment and is achieved by irradiating a bilinear coupled spin system with pulses of rf radiation. The timing and orientation of these pulses determine which orders of coherence are excited, and the duration of the excitation influences the amplitudes of the excited coherences. Control of excitation selection rules through the use of rf pulse sequences makes it possible to control both the form of the density matrix at the beginning of the evolution period and the effect of the mixing process, allowing indirect detection of non-single-quantum coherences[23-26].

Exact calculation of spin system dynamics during a multiple pulse experiment can be quite difficult, and is often unnecessary. Coherent averaging theory provides a straightforward method of calculating the time-independent effective Hamiltonian of a complex pulse sequence, provided that the time dependent perturbations to be averaged over are cyclic and periodic [22,27]. The effective Hamiltonian produces the same net evolution as the complex time-dependent Hamiltonian, as depicted in Figure 2.6, within the restrictions of the formalism. The effective Hamiltonian determines the selection rules for coherence excitation and influences the information content of the resulting spectra. This formalism, also known as average Hamiltonian theory (AHT), has been presented in several texts on NMR spectroscopy, so discussion here will be minimal.

Coherent averaging theory simplifies calculation of the evolution of a spin system under the influence of a periodic time-dependent Hamiltonian. The time-dependent Hamiltonian in a multiple-pulse NMR experiment can be divided into time independent and dependent parts:

$$\mathcal{H} = \mathcal{H}_0 + \mathcal{H}_1(t) \qquad (2.16)$$

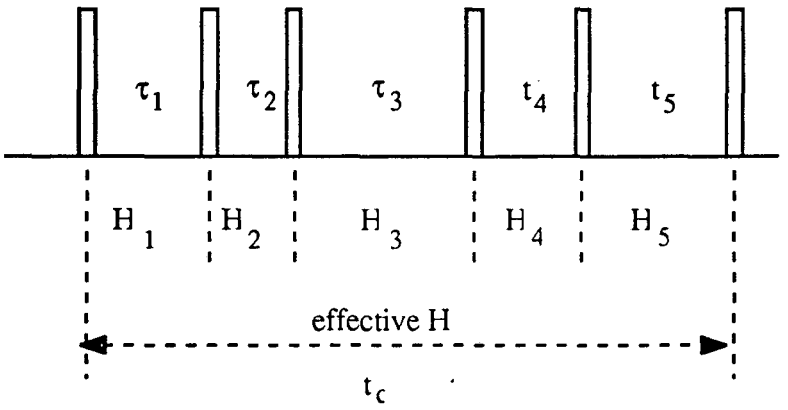

Figure 2.6. A schematic illustration of an arbitrary effective Hamiltonian. Coherent averaging theory is used to calculate the effective Hamiltonian such that ρ at the end of the cycle is the same under calculations using either the effective H or the sequential application of the actual time-dependent perturbations.

where $\mathcal{H}_0$ corresponds to the time independent internal Hamiltonian normally associated with the rotating frame, and $\mathcal{H}_1(t)$ corresponds to the time dependent rf pulse sequence.

As stated above, one restriction on the rf pulse sequence is periodicity:

$$\mathcal{H}_{rf}(t) = \mathcal{H}_{rf}(t + nt_c) \tag{2.17}$$

where t_c is the cycle time and n is an integer. The other restriction is for the propagator created by the pulse sequence to be cyclic:

$$U\ (t_c) = T \exp\left(-i \int_0^{t_c} dt \mathcal{H}(t)\right) = 1 \tag{2.18}$$

The cyclic nature of the pulse sequence allows us to infer evolution of the density matrix in the rotating frame from behavior in the toggling frame:

$$\overline{\mathcal{H}}_0 = U^{-1}(t)\ \mathcal{H}_0 U(t) \tag{2.19}$$

where $\mathcal{H}_0$ is the effective Hamiltonian, for the toggling frame coincides with the rotating frame after each cycle. The density matrix will appear to evolve under the effective Hamiltonian if observations are also periodic with the cycle time t_c.

To calculate the effective Hamiltonian, the Magnus expansion is used to express the time dependent effective Hamiltonian from expression (2.19) as [28]:

$$\overline{\mathcal{H}}_0 = \overline{\mathcal{H}}_0^{(0)} + \overline{\mathcal{H}}_0^{(1)} + \overline{\mathcal{H}}_0^{(2)} + \ldots \tag{2.20}$$

with:

$$\overline{\mathcal{H}}_0^{(0)} = \frac{1}{t_c} \sum_i H_i \tau_i$$

$$\overline{\mathcal{H}}_0^{(1)} = \frac{-i}{2t_c} \sum_{i<j} [H_j \tau_j, H_i \tau_i]$$

$$\overline{\mathcal{H}}_0^{(2)} = \frac{-1}{6t_c} \sum_{i<j<k} ([H_k \tau_k, [H_j \tau_j, H_i \tau_i]] + [[H_k \tau_k, H_j \tau_j], H_i \tau_i]$$

$$+ \frac{1}{2}([H_j \tau_j, [H_j \tau_j, H_i \tau_i]] + [[H_j \tau_j, H_i \tau_i], H_i \tau_i])) \quad (2.21)$$

where H_i's are the internal Hamiltonians in the toggling frame between the infinitely narrow pulses, and τ's are the corresponding time intervals. Accounting for finite pulse width is necessary when the pulse widths become comparable to the delay times, and this can be done by considering each pulse to be composed of an infinite number of infinitely narrow pulses. Calculations for actual sequences are included in the next chapter.

The first term of the effective Hamiltonian is simply the toggling frame internal Hamiltonian averaged over one cycle. It is also the only term in the effective Hamiltonian that is both cycle time independent and easily calculable, making the elimination of all higher order terms desirable. Odd order terms in the expansion may be eliminated by requiring the propagator over one period of length t_c to be symmetric with respect to the center of the period [22], in addition to being cyclic. For 'symmetrized' pulse sequences, the first significant error term is $\mathcal{H}_0^{(2)}$. As $1/t_c$ becomes much greater than the bilinear coupling strength, the higher order terms diminish and the average Hamiltonian, $\mathcal{H}_0^{(0)}$, closely approximates the effective

Hamiltonian.

If desired, the length of the excitation period, τ, can be altered by varying either the number of cycles over which the effective Hamiltonian operates or the time spent on each cycle, t_c. The first method produces an effective Hamiltonian which is independent of the length of the excitation time, τ. The second method can be used to study the effect of any higher order contributions to the effective Hamiltonian.

The effective Hamiltonian during the preparation period determines the selection rules for exciting multiple-quantum coherences. For example, an all order selective sequence would require:

$$\overline{\mathcal{H}_0} = C \sum_{i<j} (I_{i+} I_{jz} + I_{iz} I_{j-}) \qquad (2.22)$$

where C is a bilinear coupling constant. The time period the effective Hamiltonian is applied, nt_c, determines the effect of the propagator, U, over the excitation period:

$$U = \exp \{ i \overline{\mathcal{H}_0} nt_c \} \qquad (2.23)$$

which in turn determines the evolution of the density matrix.

The purpose of the mixing period in a MQ-NMR experiment is to 'excite' the density matrix present at the end of the evolution period to a state which allows for the non-selective indirect observation of these same elements, $\rho_{ij}(\tau+t_1)$. This is done by 'mixing' the elements of the density matrix until either the population or single-quantum terms of ρ contain a representative sampling of all $\rho_{ij}(\tau+t_1)$. Any phases acquired during the evolution period (see below) will appear as modulation of the

single-quantum signal. Thus the multiple-quantum coherences are indirectly observed by the effect they have upon spins which participate in single-quantum coherences during the detection period.

Mixing is accomplished by two methods. The first method is to subject the excited system to a single hard pulse, such as in the three pulse experiment [3] depicted in Figure 2.7. The mixing achieved is 'random' in the respect that the observed single-quantum coherence contains only representative contributions from the higher order coherences, leading to less than optimal absolute intensity in the single-quantum spectrum. The second method is to use the mixing period to reverse the excitation of the preparation period [21], commonly referred to as 'time reversal'. The effect of this method is to refocus all of the spin polarization back to the population terms of the density matrix, allowing the maximum single-quantum signal after a $\pi/2$ pulse, as depicted in Figure 2.8.

'Time reversal' in a spin network is accomplished by using coherent averaging theory to create an effective Hamiltonian proportional to the Hamiltonian of an earlier period but opposite in sign:

$$\overline{\mathcal{H}}_0^{\,rev} = -C\,\overline{\mathcal{H}}_0 \tag{2.24}$$

where C is a proportionality constant. 'Time reversal' occurs when the propagators generated during the two periods cancel:

$$U_2^{-1}\,U_1^{-1}\,\rho\,U_1\,U_2 =$$

$$\exp\left(-i\overline{\mathcal{H}}_0^{\,rev}t_2\right)\,\exp\left(-i\,\overline{\mathcal{H}}_0 t_1\right)\,\rho\,\exp\left(i\,\overline{\mathcal{H}}_0 t_1\right)\exp\left(i\,\overline{\mathcal{H}}_0^{\,rev}t_2\right)$$

$$= \rho \tag{2.25}$$

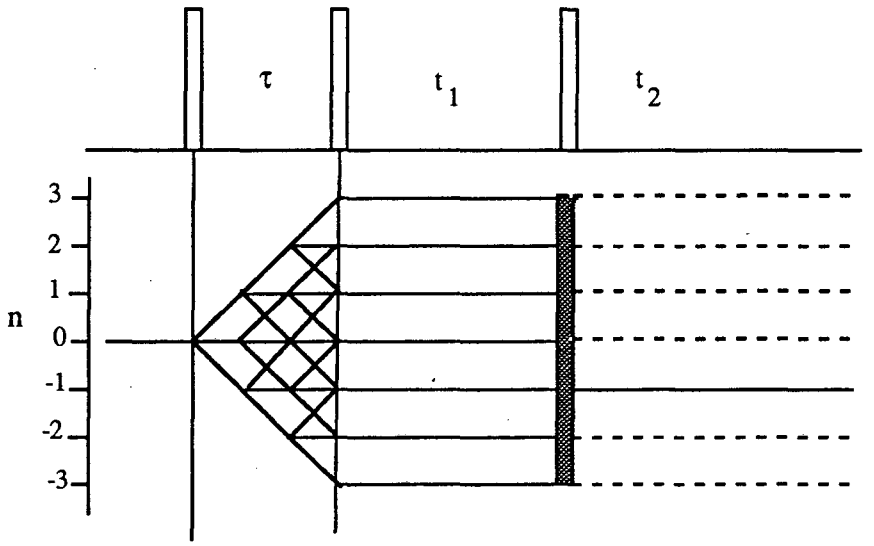

Figure 2.7. Schematic diagram of the three pulse sequence, with a coherence pathway diagram below. All order excitation during the preparation period is assumed, and the mixing of signals from coherence orders into observable magnetization is achieved by a single $\pi/2$ pulse. All orders n still exist during the detection period with only n = -1 being observable.

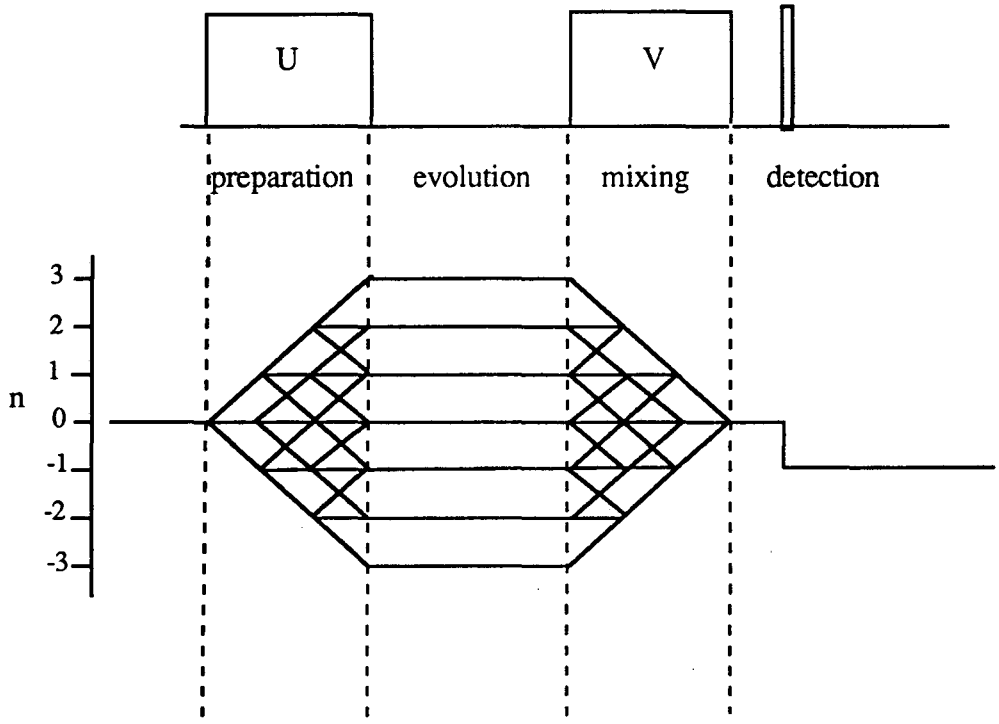

Figure 2.8. Schematic diagram of a time-reversed MQ NMR experiment, with a coherence pathway diagram below. All order excitation during the preparation period is assumed, and the mixing of signals from coherence orders into observable magnetization is achieved by refocusing polarization to population terms, followed by a $\pi/2$ pulse. Maximum signal amplitude is observed.

where $t_1 = Ct_2$. The simplest example of a time reversal experiment in NMR is the Hahn spin echo [29], where a π pulse is used to 'time reverse' spin evolution due to linear terms of the high field Hamiltonian. A more complicated example is that of the 'magic sandwich' [30-31], where a complex pulse sequence is used to 'time reverse' spin evolution due to homonuclear dipole-dipole couplings.

A time reversed MQ-NMR experiment is complicated by the addition of an evolution period between the two halves of the time reversal sequence. The interaction between the excited spin system and the effective Hamiltonian during the evolution period will not be reversed by the mixing period and will dominate the behavior of the time reversed signal.

2.3.2 Evolution

Time evolution of the density matrix is governed by the Liouville-von Neumann equation:

$$i\hbar \frac{\partial \rho(t)}{\partial t} = [\, H(t), \rho(t)]$$

where, in the absence of rf pulses, H is the internal Hamiltonian. It will be convenient to partition the internal Hamiltonian into collections of linear and bilinear terms when determining the time evolution of ρ under H. It will also be desirable to consider the evolution of the density matrix in terms of its orthogonal elements, ρ_{ij}, since these elements are what we wish to eventually measure.

Linear terms of the internal Hamiltonian are those terms which are proportional to the operator I_z, namely the resonance offset and chemical shift terms for each spin. We may define the linear Hamiltonian, H^z:

$$H^z = \sum_i (\delta\omega_i + \Omega_i) I_z \qquad (2.26)$$

where $\Delta\omega_i$ is the resonance offset experienced by the ith spin and Ω_i is the chemical shift experienced by the ith spin. The former may vary from spin to spin due to inhomogeneous magnetic fields while the latter is a function of both the chemical environment around the ith spin and the orientation of this environment with respect to the magnetic field.

The effect of H^z upon ρ_{ij} is described by equation (2.8). Expressing ρ_{ij} in the eigenoperator basis, (2.8) becomes:

$$i\hbar \frac{\partial \rho_{ij}(t)}{\partial t} = [\sum_k (\delta\omega_k + \Omega_k) I_z , |i><j|] \qquad (2.27)$$

The effect of H^z is to cause each element ρ_{ij} to acquire a time dependent phase, ϕ:

$$\phi = \sum_k (\delta\omega_k + \Omega_k) (I_{zk}^{(i)} - I_{zk}^{(j)}) \qquad (2.28)$$

which contains contributions from 'flipping' spins in the operator ρ_{ij}. The acquired phase can be used to label spins involved in an n order coherence, for each element of ρ will acquire a phase dependent upon its order:

$$\begin{aligned} \frac{i\hbar}{2\pi} \frac{\partial \rho_{ij}}{\partial t} &= \Delta\omega\, I_z |i><j| - |i><j| I_z \Delta\omega \\ &= n_{ij} \Delta\omega\, |i><j| \,, \end{aligned} \qquad (2.29)$$

where $\Delta\omega$ is the average resonance offset for all spins and $|i><j|$ is an n_{ij} quantum operator. Labeling of spins in this manner allows the separation of contributions to MQ spectra by the coherence order n_{ij}, greatly simplifying analysis of such spectra. The drawback with this particular technique, the use of a resonance offset, is that this will also cause dephasing of elements ρ_{ij} at a rate roughly proportional to their order n_{ij} [32]. The dephasing is due to the variation of resonance frequencies between the spins due to static field inhomogeneities and differences in chemical shift, for variations in resonance frequency are also amplified by order n_{ij}. Spectral lines due to higher order transitions will be progressively broader.

The dephasing described above will be exhibited as line broadening for all transitions of order higher than zero, making it desirable to eliminate this contribution to the evolution of ρ. It is well known in single-quantum NMR that such effects can be reversed by the application of a π pulse at the midpoint of the evolution period. This is true for any non-zero order coherence, for the effect of a π pulse upon an n quantum operator is to convert it into a -n quantum operator. In the limit of a ∂ pulse applied at the midpoint of the evolution period t_1 and in the absence of diffusion, the dephasing due to the spread in larmour frequencies $\Delta\omega$ becomes:

$$\rho_{ij}(t_1) = \exp\left(in_{ij}\Delta\omega\frac{t_1}{2}\right)\exp\left(-in_{ij}\Delta\omega\frac{t_1}{2}\right)\rho_{ij}(0)\exp\left(in_{ij}\Delta\omega\frac{t_1}{2}\right)\exp\left(-in_{ij}\Delta\omega\frac{t_1}{2}\right) \qquad 2.30$$

which is zero for arbitrary order n_{ij}. Of course, this also removes the desired spin labeling due to a resonance offset.

Spin labeling which is independent of variations in resonance offset may be

achieved by use of a phase shift of the rf carrier frequency during the evolution period [33]. Such a phase shift is equivalent to an rf pulse along the z axis and contributes a time independent term to the Hamiltonian:

$$H_{ps} = \Delta\phi\, I_z \qquad (2.31)$$

where $\Delta\,\phi$ value of the phase shift of the rf radiation. Phase shifts may be used in conjunction with a refocusing π pulse to acquire order separated MQ spectra without order dependent line broadening. Incrementation of the radiation phase is done in proportion to the increment of the evolution time t_1 in the two dimensional experiment, so the only effect of the phase shift is to separate the signal by coherence order upon Fourier transform. This method is known as time proportional phase incrementation (TPPI).

The bilinear terms of the high field internal Hamiltonian are:

$$H^{zz} = H^{D} + H^{J} + H^{Q} \qquad (2.32)$$

where H^D is the high field homonuclear dipole-dipole Hamiltonian, H^J is the indirect coupling Hamiltonian and H^Q is the electric quadrupole Hamiltonian. The quadrupole coupling term is included here for completeness only, for our model system of coupled spins one half precludes quadrupolar nuclei. MQ-NMR has been used to study quadrupolar nuclei [34-36], mainly as a method of side stepping the first order quadrupole moment. The work presented below is concerned with the dipolar and scalar terms of the bilinear Hamiltonian.

In the limit of strong couplings, both the dipolar and scalar terms have a similar

effect on the evolution of ρ, and the dipolar term invariably dominates. The high field homonuclear dipole-dipole Hamiltonian may be divided into two parts:

$$H'_D = D_{kl}\,(I_{kz}I_{lz} - \frac{1}{4}(I_{k+}I_{l-} + I_{k-}I_{l+})) \qquad 2.33$$

where D_{kl} is the dipolar coupling constant between the kth and lth spins. The first part of H^D contributes a splitting of 0.5 D_{kl} to the spectrum for each D_{kl} between a 'flipping' spin and a 'stationary' spin in the eigenoperator basis. The second part of H^D causes spins with differing values of m to undergo a 'flip-flop'. While this changes the z component of the spin angular momentum for the spins involved, it does not change the total z component for the element ρ_{kl}. In other words, density matrix elements of the same order n are strongly coupled to one another in the absence of strong rf radiation. Elements of different order are not coupled, assuming that the Zeeman interaction is much stronger than the dipolar or scalar interactions.

2.3.3 Detection

The detection period of a MQ-NMR experiment is technically no different from conventional pulsed NMR experiments. The difference lies in the behavior of the detected single-quantum signal as a function of the density matrix and effective Hamiltonian during the evolution period. This behavior is studied by collecting a two dimensional data set [2], $S(t_1,t_2)$, containing single-quantum fid's in the t_2 dimension and a multiple-quantum interferograms in the t_1 dimension.

The t_1 dependence of $S(t_1,t_2)$ is found by examining the propagation of the density matrix over the experiment:

$$\rho(\tau + t_1 + \tau') = U_m^{-1} U_e^{-1} U_p^{-1} \rho_0 U_p U_e U_m \quad (2.34)$$

Assuming time reversal symmetry between the preparation and mixing periods:

$$\rho(\tau + t_1 + \tau') = U_p U_e^{-1} U_p^{-1} \rho_0 U_p U_e U_p^{-1} \quad (2.35)$$

we see that successful refocusing of the density matrix depends upon the effective Hamiltonian of the evolution period. Maximum refocusing will occur when:

$$U_e^{-1}(U_p^{-1} \rho_0 U_p) U_e = \phi_{ij} (U_p^{-1} \rho_0 U_p) \quad (2.36)$$

allowing the preparation and mixing propagators to cancel. The result is the modulation of the detected single-quantum signal by the interaction of the excited density matrix with the evolution period effective Hamiltonian.

Fourier transformation of $S(t_1,t_2)$ along the t_1 dimension and projection to the t_2=0 axis generates the multiple-quantum spectrum [33]. A MQ spectrum contains many more lines than a standard single-quantum spectrum, all overlapping one another without the use of TPPI or a resonance offset to separate the transitions according to the order n. This is due to detection occurring within the rotating frame, which removes the frequency differences caused by the Zeeman interaction. TPPI separates the transitions in frequency space upon Fourier transformation, simplifying the spectrum. It is also convenient to group transitions by order n, for coherences of the same order interact with one another during the evolution period.

3

Multiple-Quantum Spin Counting

3.1 Introduction

This chapter will concentrate upon the design of MQ-NMR experiments for the study of homonuclear spin cluster sizes in anisotropic materials. Examples of such materials include nematic and smectic liquid crystals, aromatic hydrocarbons adsorbed upon a catalytic support, and spin clusters of varying size due to isotopic dilution in a solid. Determination of average spin network sizes for such systems helps determine the distribution of, and possible interactions between, molecules that constitute the system. For example, the spin cluster size observed for a hydrocarbon dispersed over a catalytic support would indicate possible molecular distributions between active sites on the support, and even possibly the distribution of the sites themselves.

Before discussing the design of MQ-NMR spin counting experiments it will be useful to consider the behavior of coupled spin networks during the excitation process and how this behavior can be manipulated to indicate the number of spins in the network. The design of the particular rf pulse sequences used during the experiments follows, beginning with an assumption of infinitely narrow rf pulses and ending with the incorporation of idealized square pulses into the calculation of the average Hamiltonian. The final section of this chapter will discuss experimental techniques available to help an experimental apparatus approximate an ideal square rf pulse source.

3.2 Spin Clusters & Dipole Coupled Networks

One of the concepts used to describe multiple-quantum spin counting experiments is 'growth' of a spin network [37- 38]. This terminology is misleading,

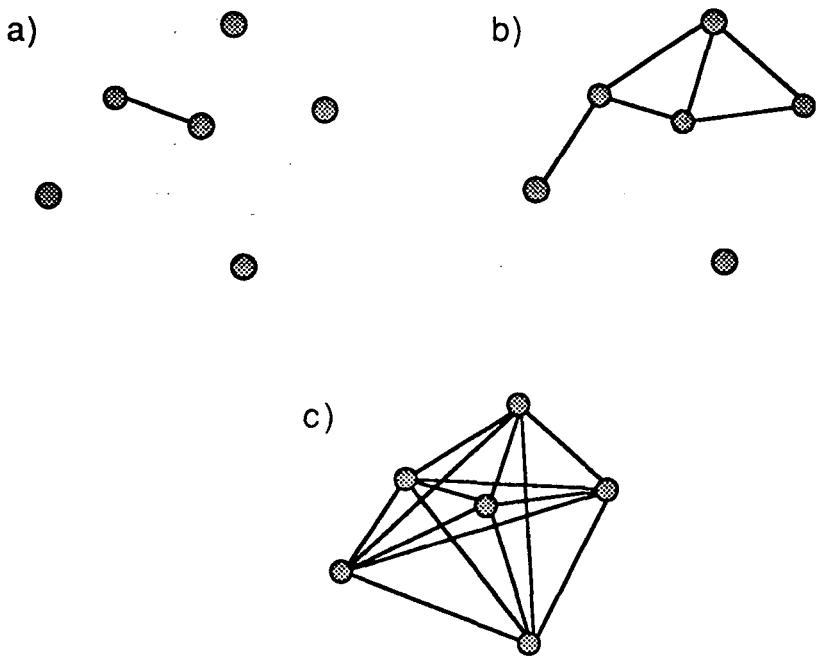

Figure 3.1. A group of spins one half, represented as shaded circles, 'growing' into a spin cluster via dipole-dipole couplings. The figures above differ in the length of the excitation process, with a) representing spin network growth at small preparation times, b) at somewhat longer times and c) at long preparation times.

for networks of dipole-dipole coupled spins exist independent of our experiments and certainly do not grow during them, for rf pulses neither create new spins nor new couplings between spins. The spin network 'growth' we observe in MQ-NMR is a measure of the strength of the couplings between spins and the rate at which spins in the network correlate to one another. Still, it is convenient to picture the 'growth' of a spin network as a net of spins with increasing interconnection as excitation time is increased, as depicted in Figure 3.1. Once the limit of the spin cluster is reached, the 'net' cannot grow further, indicated by a constant network size equal to N, the number of spins in the cluster.

To differentiate between growth of the spin network and an increase in the measured size of the spin network, the size of the spin network measured as a function of excitation time will be referred to as the apparent spin network size, N_{app}, with the assumption:

$$N_{app} \rightarrow N \quad \text{as} \quad \tau \rightarrow \infty \tag{3.1}$$

where τ is the length of the preparation period in the MQ-NMR experiment. At preparation times much longer than those necessary to excite the range of spin-spin couplings present in the material the multiple-quantum spectrum will reach a steady state, for all possible modes of coherence will have been excited [38].

The number of spins present in an isolated cluster can be found by comparing the relative intensities of multiple-quantum transitions summed by order n. Once the spectrum no longer changes with increased preparation time the density matrix is assumed to have reached the statistical limit, with each element ρ_{ij} permissible under the selection rules being equal in amplitude [37]. To illustrate the density matrix evolution from the initial condition to the statistical limit, consider ρ for an isolated cluster of four

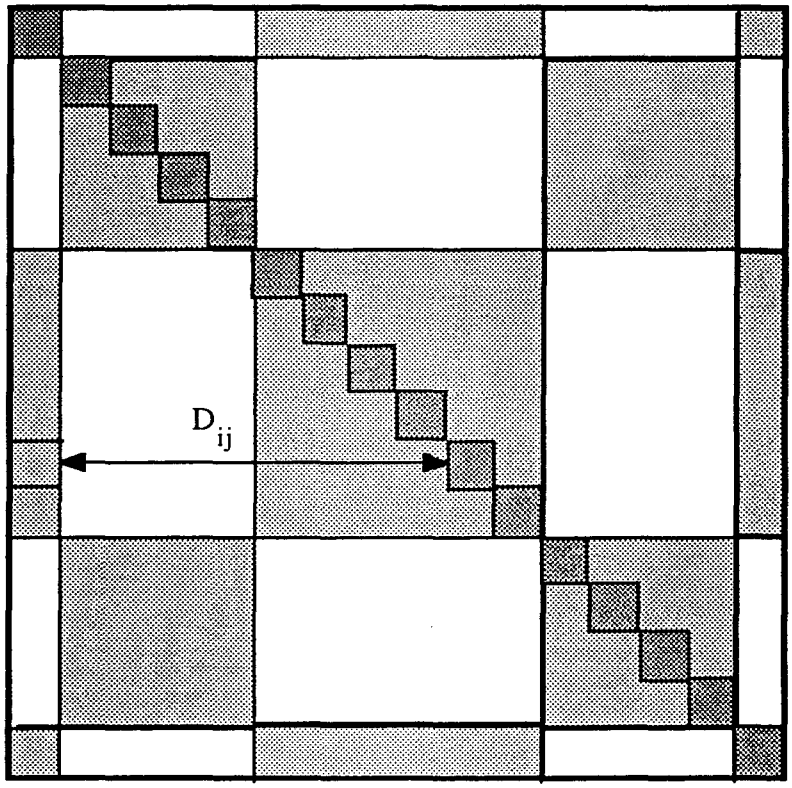

Figure 3.2. Diagram of the density matrix for a four spin system, with the 16 basis states ranked by Σm (i.e., |++++>, |+++->, etc.). The matrix contains 256 elements, with the population terms highlighted with the darker shading and the even order terms highlighted with the lighter shading. Elements are directly coupled by the dipole couplings between spins, as shown for two elements above.

dipole-dipole coupled spins, as depicted in Figure 3.2.

Initially, all spin polarization is localized along the diagonal in the population terms of ρ [16]. At time τ_0, an even order selective effective Hamiltonian is created by the use of rf pulses:

$$\overline{\mathcal{H}_0} = \frac{1}{3}\sum_{i<j}^{N} D_{ij}\,(I_{i+}I_{j+} + I_{i-}I_{j-}) \tag{3.2}$$

where D_{ij} is the homonuclear dipole-dipole coupling constant between the ith and jth spins. The evolution of density matrix elements is governed by the Liouville-von Neumann equation:

$$\left(\frac{ih}{2\pi}\right)\frac{\partial \rho_{ij}}{\partial t} = \left(\overline{\mathcal{H}_0}\,|\,i><j\,|\,-\,|\,i><j\,|\,\overline{\mathcal{H}_0}\right)\;\alpha\;(|\,r><j\,|\,-\,|\,i><s\,|) \tag{3.3}$$

where $n_{ts} = n_{rs} \pm 2$ and $n_{ru} = n_{rs} \pm 2$. Therefore, only elements of even order may be excited due to the initial state being composed of elements of zero order. The strength of the direct coupling between elements is determined by the individual D_{ij}'s, with amplitude oscillating between coupled elements at the frequency D_{ij}. Obviously, each ρ_{ij} is coupled to many other elements of the density matrix, for each possible transition allowed by the effective Hamiltonian will couple ρ_{ij} to another element. In general, the mode oscillations will not be at the same frequency, dampening one another through interference [38]. In a sense, the evolution of ρ under the effective Hamiltonian may be thought of as a spin-spin 'relaxation' process with all elements ρ_{ij} coupled under the effective Hamiltonian being equally probable due to the energy provided by the rf fields. Of course, the evolution of ρ is a highly deterministic process, the calculation of

which is limited only by computer speed and time available. Unfortunately, calculations involving more than ten coupled spins require times approaching the age of the universe. It seems reasonable to assume that all allowed modes of coherence will be equally excited after sufficiently long preparation times.

To determine the size of a spin cluster, we assume excitation has reached the statistical limit [38], with the intensity of all allowed transitions being equivalent, regardless of order. The sum of transition intensities according to n will not be equivalent, however, due to the differing number of transitions in each order. For example, there are many possible one quantum transitions in an N spin cluster, but there is only one possible N quantum transition. In general, the number of nth order elements in a density matrix describing N coupled spins one half is

$$\binom{2N}{N-n} = \frac{2N!}{(N-n)!\,(N+n)!} \tag{3.4}$$

which grows very rapidly for large N. In the limit that Sterling's approximation is valid (i.e., $(N-n) \geq 6$), the relative intensities of the sums of n order transitions approximates a gaussian distribution

$$I(n) = A \exp\left(\frac{-(n)^2}{N}\right) \tag{3.5}$$

where A is a constant and N is the number of spins in the cluster. The evolution of ρ before the statistical limit has been reached is in general quite complex, for the range of D_{ij}'s present within each cluster may vary from cluster to cluster, owing to the anisotropic nature of dipole coupling strengths. Therefore, N is determined by measuring the *apparent* cluster size as a function of preparation time, $N_{app}(\tau)$. N_{app} is

determined by performing a two parameter least squares gaussian fit of I(n), with the assumption that N_{app} accurately reflects the size of a coupled spin network only when the evolution of the density matrix reaches the statistical limit. Indeed, I(n) generally will not be closely approximated by a gaussian distribution before ρ has reached the statistical limit [37-38], due to the differing weights of each transition in the multiple-quantum spectrum. Experimentally, N is determined by:

$$N = N_{app}(\tau') \text{ if } \left(\frac{\partial(N_{app}(\tau))}{\partial\tau}\right)_{\tau=\tau'} = 0 \qquad (3.6)$$

3.3 Experimental Design

Measurement of a multiple-quantum spectrum requires the use of a pulse sequence to create the desired effective Hamiltonians for different periods of the experiment. In particular, three different pulse sequences and their variants have been used to perform the MQ spin counting experiments presented in the following chapters. The sequences differ from one another according to the propagators desired during the preparation and mixing periods of the experiment, with the evolution and detection periods being identical. They will be presented in chronological order, for the latter two were derived from the first and require many of the same experimental considerations.

3.3.1 The Eight Pulse Even Order Sequence

First for consideration is the eight pulse sequence of Baum, et al. [37], which is an adaptation of an earlier sequence [21]. The sequence is designed to create an even order selective propagator during the preparation period and its time reversed compliment during the mixing period by utilization of homonuclear dipole-dipole couplings. Since sums of the transition intensities in each order n are desired, the

signal is detected by a $\pi/2$ pulse followed by a pulsed spin lock [39]. Detection by this technique projects the observed signal $S(t_1,t_2)$ along the $t_2 = 0$ axis, enabling the collection of multiple-quantum spectra without requiring the manipulation of large 2D data sets. The evolution period is reduced to constant minimum time t_1 with a variable phase shift $\Delta\phi$ for the implementation of TPPI, effecting a summation of I by order n and minimizing the influence of H_{int} upon the system. Signal intensity in the observed spectra will be a function of the effective Hamiltonian, the preparation time, and the homonuclear dipole-dipole couplings present in the system,

$$I(n) = I(n, \bar{\mathcal{H}}_0, \tau, D_{ij}'s) \tag{3.7}$$

Implementation of the detection period is depicted in Figure 3.3(a). The spin systems' polarization has been refocused into the population terms of the density matrix at the end of the mixing period, 'freezing' the spins by placing them in states which are constants of the motion. The detection period begins with a one to two millisecond delay, allowing any residual transverse magnetization to vanish via spin diffusion while the desired time-reversed signal is stored along the z axis. The magnetization is then converted into single-quantum coherences by a $\pi/2$ pulse along the x axis, followed by a pulsed spinlock to maximize t_2 signal to noise. The use of a pulsed spinlock introduces artifacts to the observed signal, mainly due to probe and transmitter ringing. These effects are removed by acquiring each t_1 point in the data set $S(\Delta\phi)$ twice, once with a 'tipping' pulse phase of x and once with a tipping pulse phase of -x [40]. The desired signal will be inverted between the two experiments while the artifacts will not, allowing enhancement of signal and removal of artifacts by taking the difference of the

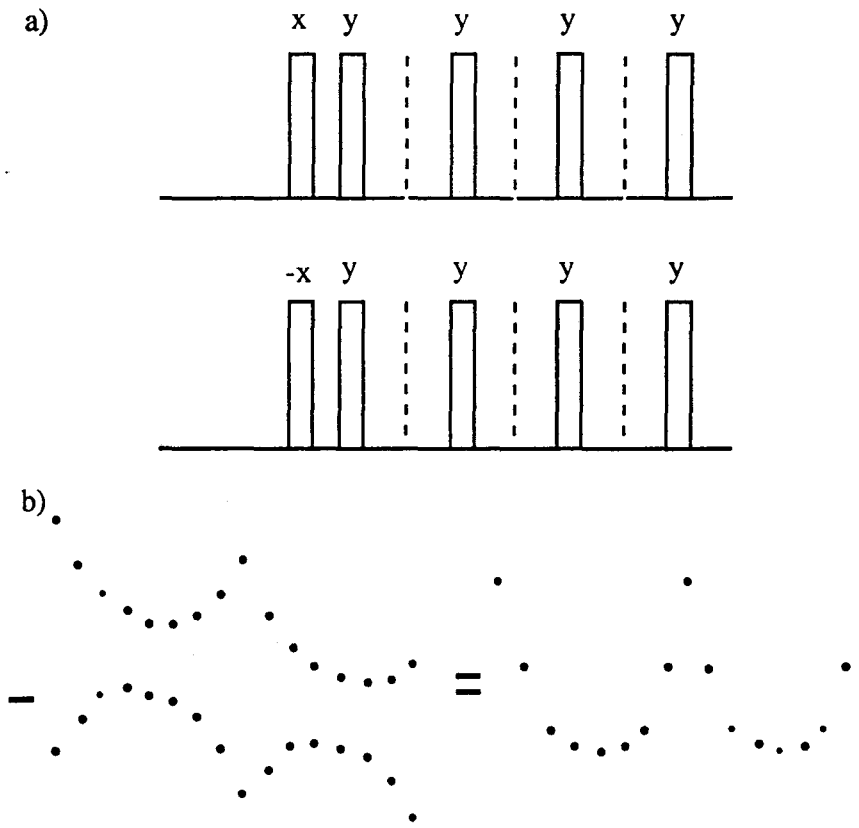

Figure 3.3. a) Schematic diagram of the phase cycled detection period for MQ cluster counting experiments. Each $\Delta\phi$ point is aquired twice, once with an 'x' detection pulse, once with a '-x' detection pulse. This is to remove artifacts due to receiver ringing. b) Depiction of the doubly aquired MQ interferogram, incremented from 0 to 2π in 16 steps. The difference of these two interferograms is shown at right, free of baseline drift and other artifacts.

acquired signals. Successful application of this receiver phase cycling technique removes baseline drift from the detected multiple-quantum interferogram, as depicted in Figure 3.3(b).

The effective Hamiltonian of the preparation period is found using coherent averaging theory [22, 27]. The calculation is performed in the toggling frame, with rotations caused by rf ∂ pulses. The first term in the expansion:

$$\overline{\mathcal{H}_0} = \overline{\mathcal{H}_0^{(0)}} + \overline{\mathcal{H}_0^{(1)}} + \overline{\mathcal{H}_0^{(2)}} + \ldots \tag{2.20}$$

is the average Hamiltonian in the toggling frame:

$$\overline{\mathcal{H}_0^{(0)}} = \frac{1}{t_c}\sum_i H_i\tau_i \tag{2.21}$$

and by convention is denoted as the zero order term. The eight pulse sequence is schematically depicted in Figure 3.4 along with the toggling frame Hamiltonian during the delays between the pulses. The average Hamiltonian can be divided into two terms, the average of the linear contributions to the Hamiltonian and the average of the bilinear contributions to the Hamiltonian. The average of the linear terms is:

$$\overline{\mathcal{H}_0^{(0)^z}} = \frac{1}{t_c}\left(2\Delta I_z - 2\Delta I_z + 4\Delta I_y - 4\Delta I_y\right) = 0 \tag{3.8}$$

removing the effects of chemical shift and static field inhomogeneity, assuming broadband excitation. This can also be seen by realizing that the effect of the pulse sequence on an isolated spin one half would be to perform one full rotation about the x axis followed by the reverse rotation. The average Hamiltonian is therefore determined by the average of the bilinear terms:

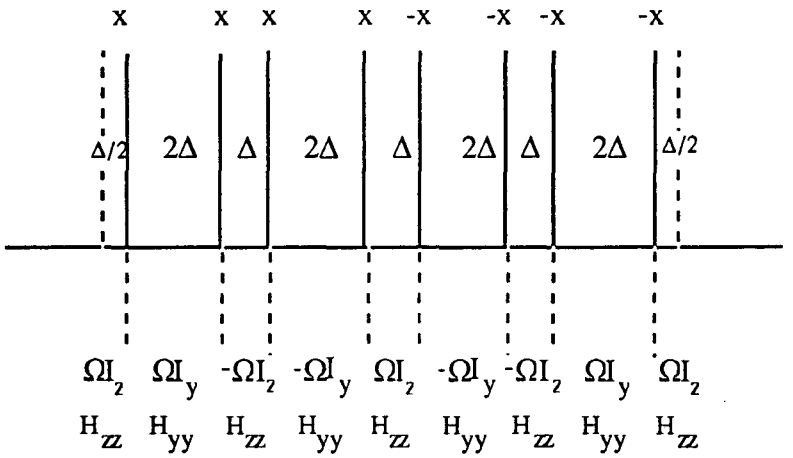

Figure 3.4. Schematic diagram of one pulse cycle in the time-reversed MQ spin counting pulse sequence. All pulses rotate the toggling frame Hamiltonian by $\pi/2$ along the noted axis, with the rotations being instantaneous (i.e., delta function pulses). The delay periods are expressed in terms of a timing constant, Δ. The toggling frame Hamiltonians are noted below the sequence, with the average Hamiltonian being proportional to (Hyy-Hxx).

$$\overline{\mathcal{H}_0^{(0)zz}} = \frac{1}{t_c}\left(4\Delta H_{zz} + 8\Delta H_{yy}\right) = \frac{4}{t_c}(H_{yy} - H_{xx}) \qquad (3.9)$$

$$\alpha \; D_{ij}(I_{i+}I_{j+} + I_{i-}I_{j-})$$

$$(\text{note} : H_{xx} + H_{yy} + H_{zz} = 0)$$

coupling elements of ρ where $\Delta n = \pm 2$. Only even order coherences will be excited, due to ρ initially containing only population terms.

To construct the effective Hamiltonian for the mixing period, note:

$$\exp(-i\,\pi/2\, I_z)(\, H_{yy} - H_{xx}\,)\exp(i\,\pi/2\, I_z) = -\,(\, H_{yy} - H_{xx}\,) \qquad (3.10)$$

satisfying the condition for time reversal. The mixing period pulse sequence is simply the preparation period pulse sequence rotated about the z axis by $\pm\pi/2$ (i.e., x pulses become y pulses).

Spins participating in the coherences are labeled using TPPI during the evolution period. The evolution time is constant, being just long enough to execute a small phase shift $\Delta\phi$ in the rf before the start of the mixing period, about 3μs. The Fourier transform will be a phase Fourier transform [41-42], with the incremented phase shift mimicking incrementation of the evolution time. A phase increment of $\pi/16$ allows for the observation of coherence orders from zero to ± 16. The spectrum should be symmetric about $n = 0$, for ρ is a Hermitian matrix.

The eight pulses and their separating delays comprise one cycle of the sequence. The preparation time τ is varied by changing the number of cycles executed, for changes in the cycle time t_c may alter the effective Hamiltonian . While the average Hamiltonian is cycle time independent, higher order terms in the effective Hamiltonian are explicit functions of t_c:

$$\overline{\mathcal{H}_0^{(1)}} \propto \frac{-i}{t_c}\Delta\cdot\Delta = \frac{-i}{t_c}\left(\frac{t_c}{12}\right)^2$$
$$\overline{\mathcal{H}_0^{(2)}} \propto \frac{-1}{t_c}\Delta\cdot\Delta\cdot\Delta = \frac{-1}{t_c}\left(\frac{t_c}{12}\right)^3 \qquad (3.11)$$

where the delay times τ_i have been expressed as fractions of t_c. Clearly, it is desirable to minimize the influence of these higher order terms upon the effective Hamiltonian, leaving only the average Hamiltonian. Odd order terms the effective Hamiltonian can be eliminated by restricting the toggling frame Hamiltonian to be symmetric about the center of the cycle [22], causing the cancellation of terms contributing to each odd order. The even order terms remain, and must be minimized by keeping t_c as short as possible. If the product of the cycle time and the average dipole coupling magnitude is much less than one, the effective Hamiltonian will be dominated by the average Hamiltonian with the second order contribution being the most significant error term.

To demonstrate the contribution of higher order terms to the effective Hamiltonian, calculation of one of the nested commutators in (2.21) will be examined. The first non-zero nested commutator in the expansion of the second order term is:

$$\begin{aligned}\left[H_3\tau_3, \left[H_2\tau_2, H_1\tau_1\right]\right] &= \frac{1}{t_c}\left[(\Omega I_y + H_{yy})\, 2\Delta\ ,\ \left[(\Omega I_z + H_{zz})\,\Delta, (\Omega I_y + H_{zz})\, 2\Delta\right]\right] \\ &\approx (t_c)^2\ [H_{yy},\ [H_{zz},\ H_{yy}]]\end{aligned} \qquad (3.12)$$

which is a collection of four spin terms with $-4 \le \Delta m \le 4$. The second order contribution to the effective Hamiltonian for the eight pulse sequence contains many nested commutators such as (3.12), and the terms contained in these commutators do not entirely cancel upon summation. Since most of these terms contain I_{iz} operators,

the effective Hamiltonian will now contain terms which are anti-phase to the average Hamiltonian in addition to Δm other than ± 2. Similar calculations can be performed to find the higher order effective Hamiltonian terms for the mixing period. Effects from higher order terms from the preparation period which have 'time reversed' compliments in the mixing period will be refocused along with the average Hamiltonian, enabling their influence to be observed in multiple-quantum spectra. The rest of the terms are not reversed in the mixing period, causing a loss of signal which discriminates against the observation of the most strongly coupled spins, due to the D_{ij} dependence of the higher order coherent averaging terms. Since the strongest of these error terms scale as:

$$\overline{H_0^{(2)}} \propto \overline{|D_{ij}|}\,(\overline{|D_{ij}|}\,t_c)^2 \tag{3.13}$$

where $|D_{ij}|$ is the dipole coupling magnitude between the ith and jth spins, keeping the cycle time short enough so that:

$$(\overline{|D_{ij}|}\,t_c) < 0.1 \tag{3.14}$$

reduces the difference between the effective Hamiltonian and the average Hamiltonian to less than one percent.

3.3.2 The All-Order Time Reversed Sequence

A direct descendant of the eight pulse sequence depicted in Figure. 3.4 is the all order time reversed MQ-NMR sequence [43], depicted in Figure. 3.5. The similarity between the two is not coincidence, for the latter is essentially a $\pi/4$ rotation of the former about the y axis:

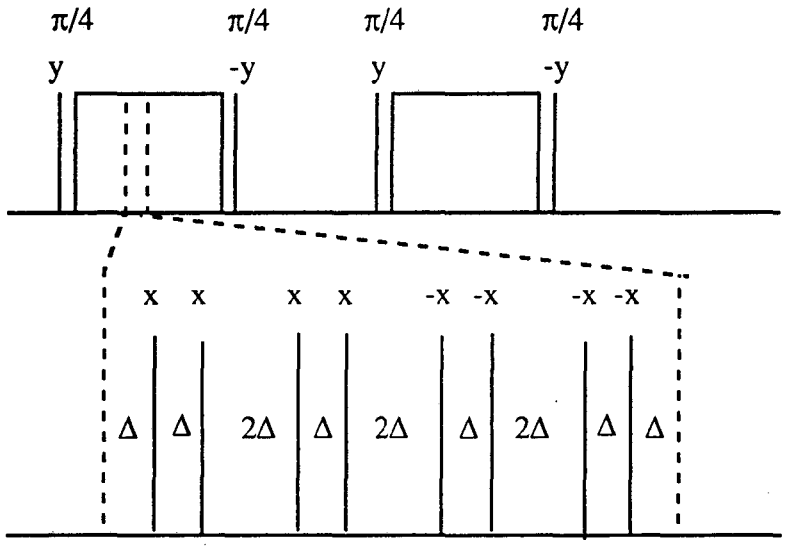

Figure 3.5. Schematic diagram of the all-order selective time-reversed MQ spin counting pulse sequence, with one cycle expanded and diagramed below. All pulses in the cycle rotate the toggling frame Hamiltonian by $\pi/2$ along the noted axis, with the rotations being instantaneous (i.e., delta function pulses). The delay periods are expressed in terms of a timing constant, Δ. The sequence is basically that displayed in Figure 3.4 with the delays exchanged and the entire preparation and mixing periods rotated $\pi/4$ along the y axis.

$$\exp(-i\,\pi/4\,I_y)(H_{zz} - H_{xx})\exp(i\,\pi/4\,I_y) = \frac{1}{3}\sum_{i<j}^{N} D_{ij}\,(I_{i+}I_{jz} - I_{i-}I_{jz}) \qquad (3.15)$$

where N is the number of spins in the sample. An all order sequence is desirable for the study of small spin clusters due to the limited number of MQ transition orders available. Use of the above all order sequence allows the observation of all transitions in a MQ spectra with increased signal due to time reversal symmetry. One disadvantage of an all order sequence when compared to an even order sequence is the detection of deviation from the average Hamiltonian by the effective Hamiltonian. Detection of odd order transitions while using an even order sequence is a clear sign of errors due to either $D_{ij}t_c$ being too large or experimental errors (e.g., drifting rf power, etc.). Errors are not as easily detected in an all order MQ spectrum. A second difficulty associated with rotating the entire sequence as above is dependence upon a pair of $\pi/4$ pulses, which may or may not be accurately timed by setting the pulse duration to one quarter that needed during a π pulse. In general, the best method of testing an all order sequences performance is to run back to back all and even order MQ experiments. Proper performance is indicated by the lack of odd order signal in the even order spectrum and similar transition intensity ratios between even order transitions in both spectra.

The above effective Hamiltonian calculations assumed rf pulses of negligible duration when compared to the intervening delays. This is generally not the situation encountered when conducting experiments with materials containing strongly dipole-dipole coupled spins. This can be seen by calculating t_c as a function of rf duty cycle:

$$t_c = 8t_p(\text{duty cycle})^{-1} \tag{3.16}$$

for the eight pulse sequence where t_p is the length of one rf pulse, and using expression (3.16) to estimate the maximum dipolar line width allowable for the sample. For a typical pulse length of 2 μs and a duty cycle of 0.1 (i.e., the sample is irradiated by strong rf 10% of the time), the maximum dipolar width becomes

$$|\overline{D_{ij}}| \sim (10t_c)^{-1} = 0.1\ (\ 160\ \mu s\ )^{-1} \tag{3.17}$$

or about 600 Hz, rather disappointing compared protium dipole-dipole couplings in solids of several to tens of kilohertz. (Observing protium clusters is of particular interest due to the near isotopic purity of hydrogen as protium and the abundance and importance of hydrogenated compounds.) Spin clusters with homonuclear dipole-dipole couplings of even a few kilohertz will require rf pulse lengths comparable to the free precession delay times to satisfy expression (3.14).

To calculate the contribution of rf pulses to the average Hamiltonian, each finite width pulse is approximated by an infinite number of infinitely narrow pulses. The toggling frame bilinear Hamiltonian during a pulse along the x axis becomes

$$H_{rf} = \phi\left(\frac{-H_{xx}}{2}\right| + \frac{3}{4}\sin 2\phi(I_{iz}I_{jz} - I_{iy}I_{jy}) + \frac{3}{2}\sin\phi^2(I_{iz}I_{jy} + I_{iy}I_{jz}) \tag{3.18}$$

where ϕ is the rotation angle. Both the experimental eight pulse sequence and the all order time reversed sequence are modified to account for finite pulse width, as depicted in Figures 3.6(a&b). Note that the modifications to these sequences are equivalent to treating the pulses as instantaneous rotations at the center of each pulse. The interference term in (3.18) is partially compensated for by reversing the orientation of

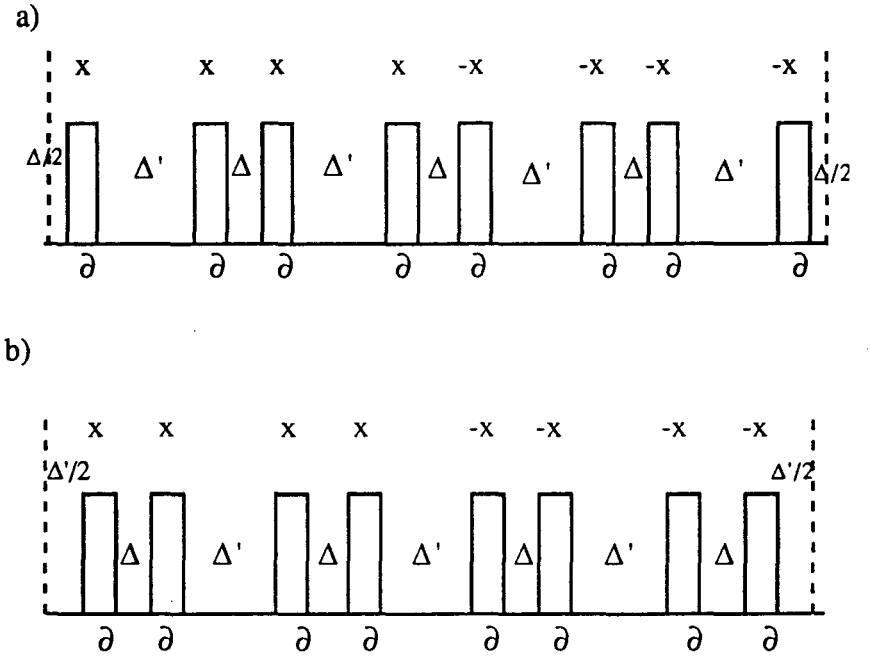

Figure 3.6. Schematic diagrams of one pulse cycle from:

a) the eight pulse even selective sequence, and

b) the all order selective time-reversed sequence.

Both pulse cycles have been modified to take into account the finite width of the rf pulses, ∂. The timing delays are Δ and Δ' in length, with $\Delta' = 2\Delta + \partial$.

the pulses in the second half of each cycle. This treatment assumes perfectly square pulses, requiring a low Q probe and delays of finite width between the pulses. The sequences diagramed in Figure 3.6(a&b) were found to function best with the short delay equal to t_p, with the shortest reproducibly 'square' pulse typically having a length t_p of 2.5 μs. The resulting cycle time is 60 μs, which leads to a maximum dipolar width of ~ 1700 Hertz. Relaxing the error tolerance from 1% to 5% increases the maximum dipolar width to ~ 4000 Hertz, which is comparable to the lower end of the range of dipole-dipole coupled protium cluster coupling magnitudes. More strongly coupled spins require either more powerful rf amplifiers, a new pulse sequence with a shorter t_c, or both.

3.3.3 A Four Pulse Even Order Sequence

Inspection of expression (3.18) for the toggling frame average Hamiltonian reveals that H_{rf} simplifies considerably for π pulses:

$$H_{rf} = \phi\left(\frac{-H_{kk}}{2}\right) \tag{3.19}$$

where k is the axis parallel to the pulse. This suggests the pulse sequence depicted in Figure 3.7. A prepulse is applied to rotate the toggling frame Hamiltonian π/2 along the x axis. Each cycle of the sequence is composed of two π pulses along the x axis followed by two π pulses along the -x axis, all separated by free precession delays. Average Hamiltonian contributions from terms linear in angular momentum cancel one another, as can be easily seen from Figure 3.7. Average Hamiltonian contributions from terms bilinear in angular momentum consist of $-(1/2)H_{xx}(t_\pi)$ terms acquired during the rf pulses and $H_{yy}\Delta$ acquired during the delays. Setting $\Delta = 0.5t_p(\pi)$, the

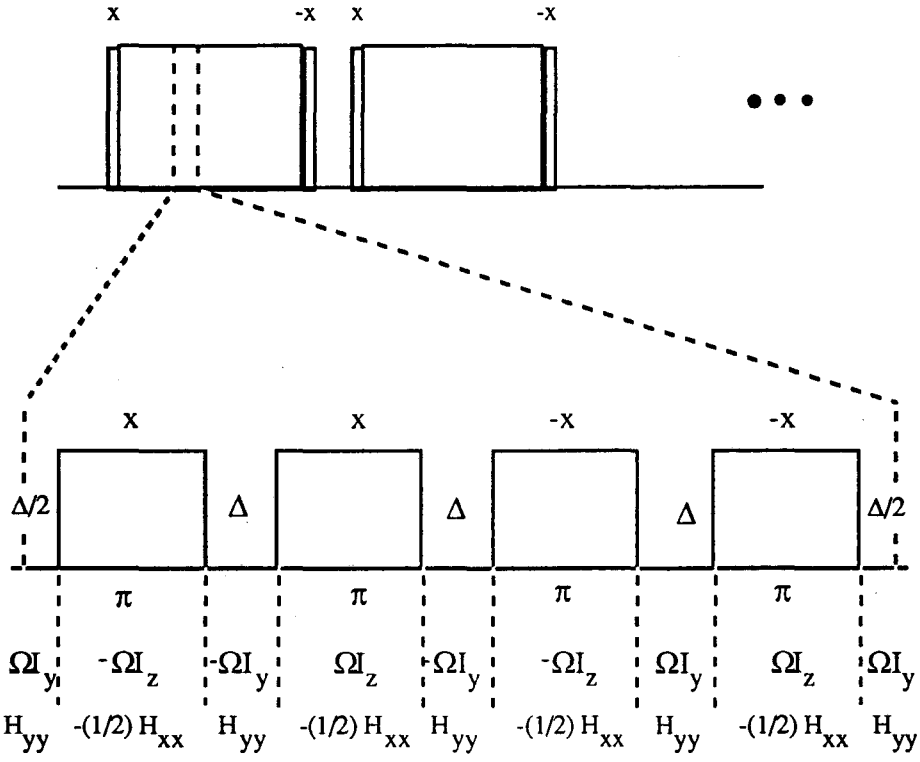

Figure 3.7. A schematic diagram of the four pulse even selective sequence with one of the pulse cycles expanded and diagramed. The outer pulses are timed to cause $\pi/2$ rotations while all the pulses within the cycles are π pulses. The time dependent toggling frame Hamiltonians are denoted below the expanded cycle.

average Hamiltonian becomes:

$$\overline{\mathcal{H}_0^{(0)}} \alpha (H_{yy} - H_{xx}) \tag{3.20}$$

as desired. An obvious disadvantage of this sequence is that the cycle time is determined entirely by the length of a π pulse:

$$t_c = 6t_p(\pi) \tag{3.21}$$

for the delay times cannot be varied independently of the pulse length. A second disadvantage is a high duty cycle (2/3) during the experiment, placing a strain on the rf amplifier and possibly overheating the sample. An obvious advantage of this sequence is that t_c is roughly half that of the eight pulse sequence, doubling the allowable dipole-dipole coupling in a material to be studied. A second advantage is the almost exclusive use of π pulses, the only pulse length easily set in a strongly coupled spin system. This sequence was found to perform best with a t_π of 6.0 μs (t_c = 36 μs), with the pulse amplitude being limited primarily by amplifier droop.

In each of the preceding cases pulses were assumed to be perfectly square in addition to being accurately timed and phased. Small errors in pulse shape, timing and/or phase tend to accumulate rapidly during multiple pulse experiments [44], for an experiment may contain hundreds of pulses at long preparation times. Sequences can be compensated for some small errors while other errors may be reduced or eliminated by apparatus design. For example, the basic pulse cycle in each of the preceding sequences contained one full rotation about the x axis followed by a full rotation about the -x axis, eliminating any pulse length error common to both x and -x pulses. Technical considerations common to all three sequences are described in the following

section.

3.4 Technical Considerations

The pulse sequences depicted in Figures 3.6 and 3.7 assume an ideal rf square pulse source to create the desired series of effective Hamiltonians and their propagators. The source is ideal in the sense that the pulse sequence is executed with no errors in pulse shape, phase, amplitude, or homogeneity across the sample. These and other technical problems can be overcome by a combination of pulse sequence and apparatus design.

First, there are a few deviations from ideality which have minimal impact upon the signal $S(\Delta\phi)$ as detected in the above experiments, where $\Delta\phi$ is the rf phase shift executed during the evolution period. Spin locking the detected signal greatly enhances the t_2 S/N in $S(\Delta\phi)$, so much so that experimental scatter is dominated by t_1 noise. All the above sequences restrict the evolution period to the minimum necessary to execute an rf phase shift, creating average Hamiltonians independent of chemical shifts and small resonance offsets during the preparation and mixing periods, causing $S(\Delta\phi)$ to be insensitive to minor variations in the static field. In general, detection of signal and resolution of spectra is not difficult assuming proper execution of the pulse sequence.

As alluded to above, the main problems encountered when conducting a multiple-quantum spin counting experiment involve imperfections in the transmitter side of the apparatus, causing non-ideal pulse sequence execution. In other words, while this technique is insensitive to the effects of t_2 noise, it is particularly vulnerable to the effects of t_1 noise. Potential sources of t_1 noise include misalignment of rf pulses (i.e., lack of transmitter quadrature), variation in amplitude between quadrature phases, variation in pulse amplitude within an experiment (amplifier ripple and droop), variation

in pulse amplitude between acquisitions along the t_1 axis (amplifier drift), non-ideal pulse shapes (pulse 'glitches'), rf inhomogeneity throughout the sample, and errors in phase shift during the evolution period. All of these non-idealities directly affect the spin network excitation processes, causing the 'noise' to be part of the signal, instead of being added to the signal. The effects of these non-idealities cannot be lessened by increasing the sample size or increasing spin polarization, for an increase in signal amplitude will lead to a proportional increase in the 'noise'. Reduction of the 'noise' requires either reduction of the non-idealities or of their effects upon the signal $S(\Delta\phi)$. The former is accomplished by improving the transmitter, the latter by crafting pulse sequences to compensate for non-idealities.

3.4.1 Hardware Considerations

All experiments included in this work were performed on a home-built heterodyne spectrometer with a static magnetic field of 4.2 Tesla and an intermediate frequency of 30 Megahertz. A more detailed description of the spectrometer can be found in the appendix, including diagrams of the hand-made components. The components described below can be used to enable most pulsed NMR spectrometers to perform time domain multiple-quantum experiments.

A SciTech digital frequency synthesizer was used to generate the intermediate frequency (IF), allowing accurate rf phase shifts by multiples of $.0005\pi$ radians, or 1/4000th of a cycle. The digital frequency synthesizer is controlled by a home-made interface, allowing the rf phase to be set by hand or by TTL pulses. The time required to implement a shift in the rf phase is limited by the time required for the interface to respond to TTL pulses during an experiment, somewhat less than 3 μs. As a result, the evolution period can be kept short enough to minimize the impact of the internal Hamiltonian upon ρ. In addition, the digitally synthesized IF amplitude is very stable, eliminating a potential source of rf power fluctuation.

Rf quadrature is generated by feeding the phase controlled IF into an analog quadrature generator (quad box) designed in the Pines lab [44]. A quad box is used in addition to a digital frequency synthesizer to allow the execution of quadrature phase shifts on a time scale faster than the spectrometer time increment of 50 ns, enabling the use of windowless and semi-windowless pulse sequences. When used in conjunction with tune up sequences as described in [45] and below, the transmitter quadrature can be set with effectively arbitrary accuracy using this device, minimizing differences in pulse amplitude between quadrature phases channels and errors in quadrature phase. This design has been found to be stable over long periods of time, requiring tuning less than once per week.

The next, and possibly most troublesome, transmitter component to worry about is the high power rf amplifier. In general, every watt of power which can be reliably supplied is desired, for the investigator is constantly trying to reduce the pulse sequence cycle time t_c. Although many high power rf amplifiers are commercially available, finding a constant high power amplifier can be troublesome, for the ideal amplifier would have both zero droop and zero ripple over several hundred pulses at high power (1000+ watts). The best rf amplifier encountered for our purposes was a tuned Henry amplifier driven by an ENI 4000L. The Henry amplifier had been modified to include an inductively coupled circuit on the high power side of the rf tube, a circuit which could be tuned to match a probe by adjusting a variable capacitor and manipulating the coupling elements. The Henry's high voltage power supply was replaced by one designed in the LBL electronics shop to eliminate power droop. The ENI was selected by testing all the 100W amplifiers in lab for stability using the 'flip-flip' sequence described below, with this amplifier being markedly more stable than the others (including two other ENI 4000L's). The ENI was run at ~ 50W to drive the modified Henry for a final output of ~500W with both droop and ripple well

below 1% of output.

The last transmitter element for consideration is the rf probe. The probe should have a low Q to prevent ringing and pulse distortion, placing even higher demands for rf power, and the tuning should be stable with respect to temperature fluctuations and over time. The static field homogeneity requirements are lax compared to most NMR experiments, so materials normally not used in NMR probes (e.g., 'non-magnetic' stainless steel) can be used for various accessories (e.g., cold N_2 transfer lines for variable temperature experiments). A many turn solenoid should be used for the sample coil for optimal rf field homogeneity. If the probe is to be used for variable temperature work, pains should be made to insure that the temperature control is steady to ± 1-2 K, for the tuned circuit will often respond to a change in temperature faster than the sample, especially at temperatures far from room temperature. Design of a variable temperature MQ-NMR probe is included in the appendix.

Once a transmitter is complete, it must be matched and tuned to allow the approximation of an ideal real rf source. The tune-up process is composed of two steps; tuning and matching the probe and amplifier to one another, and accurately setting the quadrature phases and amplitudes. The probe and amplifier are tuned to each other in order to achieve the best pulse shape at the desired resonance frequency. Matching the amplifier to the probe also appeared to stabilize the amplifier's output power as observed with a 'flip-flip' sequence. Tuning the transmitter quadrature phases and amplitudes minimizes errors introduced to the effective Hamiltonian due to improper pulse phase and rotation differences between quadrature phases.

The tuning and matching of the probe and amplifier is performed by placing a high-power directional coupler between the amplifier and the probe, allowing observation of shape and amplitude of the forward and reflected pulses. The probe is tuned by adjusting a variable tuning capacitor to minimize the reflected pulse amplitude,

and the amplifier is matched to the probe by observing the forward pulse shape, turning off the amplifier and adjusting the gap in the inductively coupled link in the Henry amplifier, turning on the amplifier and observing the pulse shape, etc. The desired result is a large forward square pulse without transient 'horns' at the pulse edges and minimal reflection from the probe.

Amplifier stability can be tested by running the 'flip-flip' experiment on a sample of isolated spins one half, such as a 2mm diameter sphere of doped acetone. The 'flip-flip' experiment is simply a train of rf pulses with signal acquisition between each pulse, as depicted in Figure 3.8(a). Rotation angles induced by the pulses can be determined from the observed signal pattern, especially if the rotation is an even divisor of 2π. The rotation angle can be set by varying the pulse amplitude while observing the signal until the desired pattern is found. Amplifier stability can be tested by repeating the experiment over long periods of time while observing fluctuations in the signal pattern (i.e., changes in pulse amplitude).

3.4.1.1 Optimizing Hardware

The sequences used for tuning the transmitter quadrature phase and amplitude have been described in detail elsewhere [45], so discussion here will be kept to a minimum. First, all four quadrature pulse amplitudes are set to correspond to a $\pi/2$ rotation of the magnetization by use of the 'flip-flip' sequence, as depicted in Figures 3.8(a&b). Then, the quadrature pulse phases are set using the 'Haubenreisser' sequence [46], as depicted in Figure 3.9, setting phase differences to $\pi/2$ between three of the four phase pairs: x&y, x&-y, -x&y, and -x&-y, for setting three of the angles determines the fourth. The signal observed for the 'Haubenreisser' sequence using the fourth pair of phases is a test of both the quadrature phase and the rotation angles for all four channels. Slight maladjustment of any of the phases or rotation angles will prevent observation of the desired signal pattern for all four phase pairs.

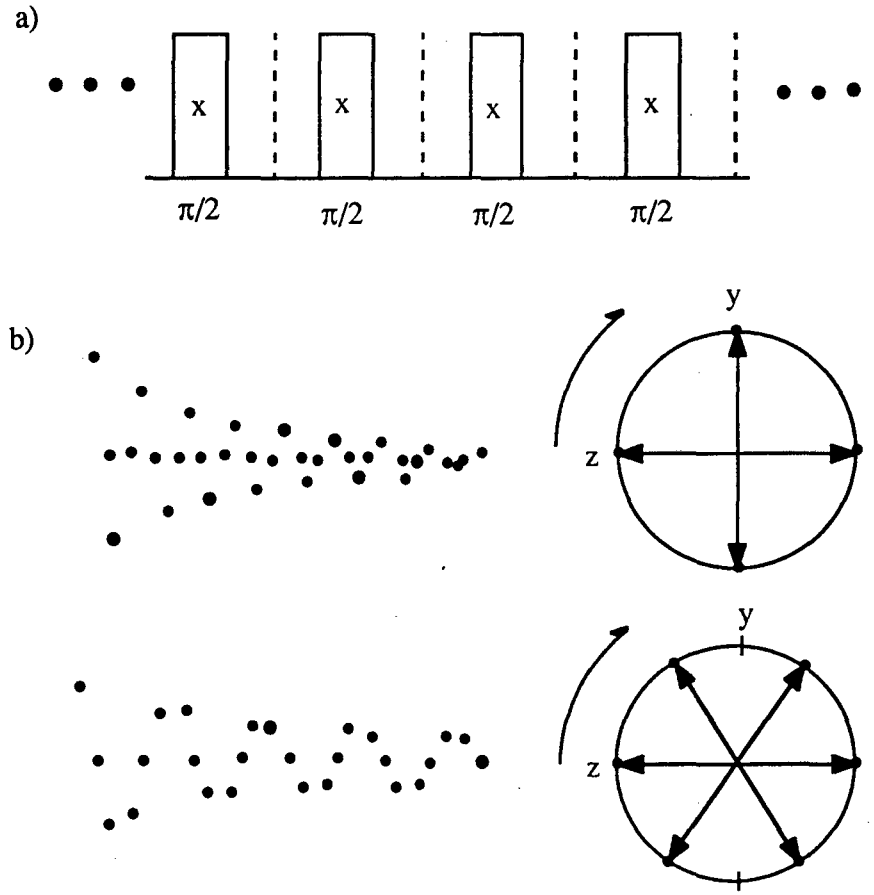

Figure 3.8. a) A schematic diagram of the 'flip-flip' sequence with $\pi/2$ x pulses. The sequence is convenient for setting pulse lengths which can be expressed as $2\pi/N$, where N is an integer. b) Depiction of the signal patterns anticipated from setting $\pi/2$ and $\pi/3$ pulses, with diagrams showing the rotation of the magnetization vector in the plane normal to the pulse axis.

Unfortunately, MQ-NMR experiments are conducted on materials which are worthless as samples for the above tune-up sequences, requiring tuning the transmitter with one sample and conducting MQ-NMR experiments upon another. Changing samples requires retuning the probe, rematching the amplifier to the probe, and resetting the transmitter power to achieve the desired rotation angle from the pulses. While it is easy to retune the probe, rematching the tuned amplifier is not trivial, so the amplifier is normally matched to the probe with the strongly dipole-dipole coupled sample in the coil. This will cause an acceptably slight mismatch during the tune-up procedure. The pulse amplitude is reset by varying the transmitter power to minimize the signal observed after a π pulse. Resetting the pulse amplitude by maximizing the observed time-reversed multiple-quantum signal is an alternate method. Since it is possible to increase the observed signal amplitude by increasing higher order contributions to the effective Hamiltonian, the latter method requires confirmation by checking the signal intensity following a π pulse. Appreciable transverse magnetization following a nominal π pulse is indicative of significant errors in pulse tip angles and phases, errors which often lead to the introduction of higher order terms to the effective Hamiltonian.

3.4.2 Software Considerations

Finally, the effects of t_1 noise sources can be reduced by the pulse sequence design [34,40,47]. All three sequences described above consist of pulse cycles which perform a net zero rotation of the toggling frame, preventing the accumulation of pulse amplitude errors between cycles. Only two quadrature phases are used, x and -x, and except for the rf phase shift the experimental preparation sequence is identical to the mixing sequence, reducing the number of components which can drift and contribute errors. Odd order contributions to the effective Hamiltonian from the internal Hamiltonian are eliminated by symmetrizing the toggling frame Hamiltonians about the

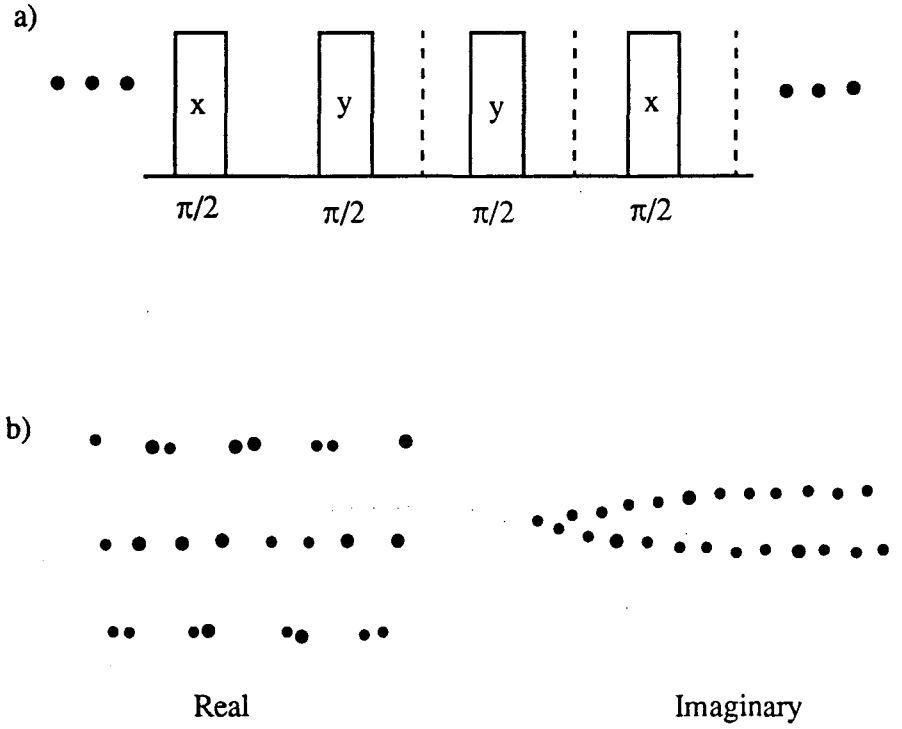

Figure 3.9. a) A schematic diagram of the 'Haubenreiser' sequence, used to check and set the quadrature phase of the rf transmitter. b) Depiction of the signal observed when a pair of phases are near the desired angular separation of $\pi/2$. The pattern observed in the imaginary buffer is quite sensitve to small errors in the phase relationship between the two phases and is ideally two overlapping flat lines.

center of the pulse cycle. Odd order contributions to the effective Hamiltonian from resonance offsets or rf inhomogeneity can be eliminated by symmetrizing their respective toggling frame Hamiltonians about the center of the pulse cycle [40], as depicted in Figure 3.10. The use of only one pulse length is eliminates problems in setting pulse lengths in relation to each other, for phase transients will often prevent the determination of the length of a π/x pulse as $1/x$ of that of a π pulse. Also, the use of π pulses is desired over other pulse lengths since the pulse amplitude can be set by observing the inversion of magnetization in a solid sample.

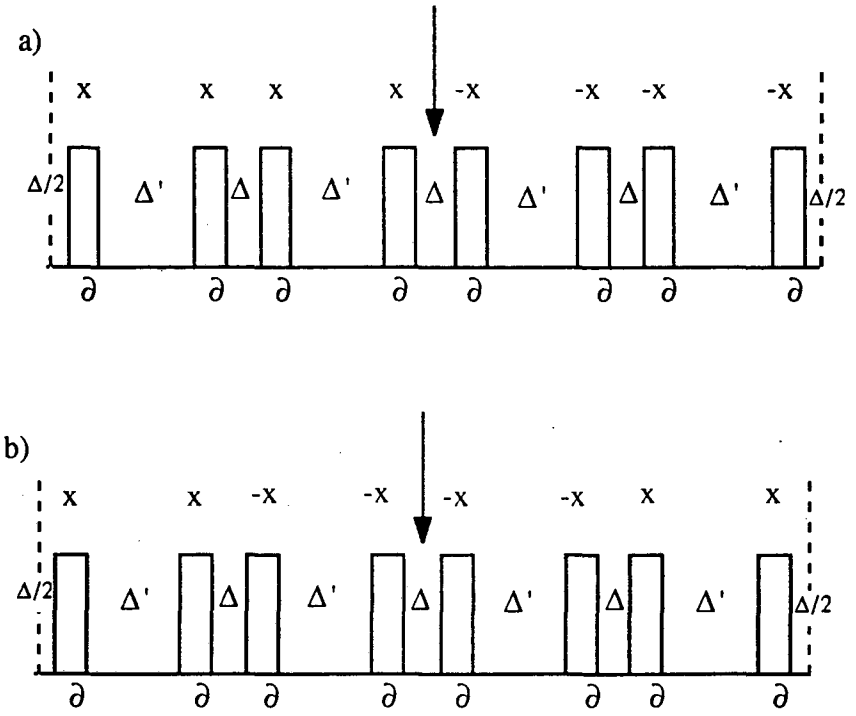

Figure 3.10. a) A schematic diagram of the even order selective eight pulse cycle with the symmetric point noted. This sequence is symmetrized to reduce the effects of resonance offset.
b) A schematic diagram of the even order selective eight pulse cycle with the symmetric point noted. This sequence is symmetrized to reduce the effects of rf inhomogeneity.
Both sequences possess the same zero order effective Hamiltonian

4

Oriented Molecules in Liquid Crystals

4.1 Introduction

The work presented in this chapter will concentrate upon the use of multiple-quantum NMR spin counting experiments to study spin networks on molecules oriented in liquid crystalline mesophases. The spin networks will be comprised of protium nuclei in alkanes dissolved in a liquid crystal, or of protium nuclei in the liquid crystal molecules themselves. Spin networks in liquid crystals form the simplest non-trivial group of systems to be studied by MQ-NMR, for the spin clusters are very well isolated from one another while retaining high a signal-to-noise ratio. This is due to the spin clusters being decoupled via diffusive motion of the molecular centers of mass while the separation of nearest neighbor molecules at any moment is small. Isolation of the spin clusters allows for the reduction of the density matrix size as discussed in chapter 2, limiting the complexity of the interactions responsible for observed phenomena. Indeed, the time evolution of isolated spin networks has been exactly calculated for small spin clusters [38].

It shall be useful to briefly review the structure of the two liquid crystal mesophases observed in this study before proceeding with a description of the experiments and their results. Experiments involving spin networks on the liquid crystal molecules themselves were performed on nematic and smectic A phases of various alkyl cyanobiphenyls, with structures depicted in Figure 4.1. Experiments involving spin networks on alkanes dissolved in a liquid crystal matrix were performed on both selectively deuterated and natural abundance n-alkanes oriented in a nematic

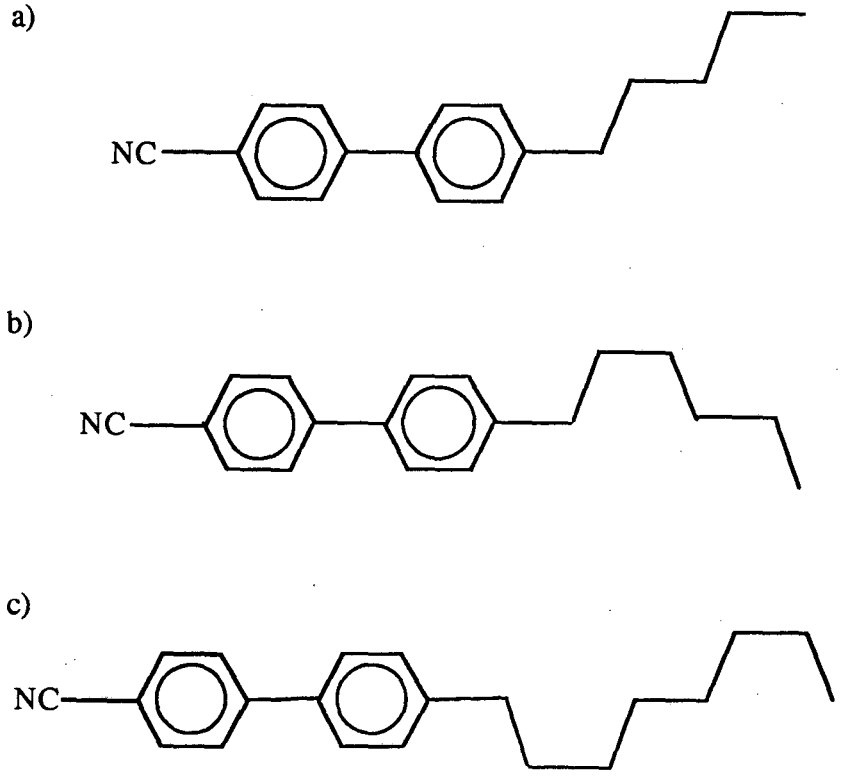

Figure 4.1. a) 4-pentyl-4'-cyanobiphenyl (5CB)

b) 4-hexyl-4'-cyanobiphenyl (6CB)

c) 4-octyl-4'-cyanobiphenyl (8CB)

liquid crystal, p-pentylphenyl 2-chloro-4-(p-pentylbenzoyloxy)-benzoate)-benzoate. Therefore, it will be desirable to review the structures of the nematic and smectic A mesophases. This will be followed by an examination of the likely average conformations of the spin cluster bearing molecules, for molecular geometry will strongly influence homonuclear dipole-dipole coupling within a spin cluster. Knowledge of the homonuclear dipole-dipole couplings present in a spin cluster will then be used to model the evolution of the density matrix for isolated spin clusters. These models will be compared with experimental results at the end of this chapter, both to verify the accuracy of the models and to gain insight into the structure of the systems studied.

4.2 Liquid Crystalline Mesophases

The experiments presented at the end of this chapter were performed on protium containing molecules oriented in liquid crystalline mesophases, both solutes and the liquid crystal molecules themselves. The description which follows is intended as a brief review of liquid crystals in nematic and smectic A mesophases in general. More information may be found in the many texts available on the subject of liquid crystals [48-50].

It is well known that several compounds exist which posses phases intermediate in structure between a crystalline solid and an isotropic liquid. These liquid crystalline mesophases combine a liquid-like diffusive motion of molecular centers of mass with a solid-like orientational order of individual molecules. In general, the translation of an individual molecule's center of mass is not correlated to any other molecule's center of mass, averaging the dipole-dipole couplings between molecules to zero over the NMR time scale. Molecular orientation within the bulk material is correlated to strong magnetic fields, with molecules tending to align parallel

and anti-parallel to an external magnetic field. The anisotropic nature of molecular tumbling in a liquid crystal mesophase allows non-zero average dipole couplings between protium nuclei on the same molecule, generating a spin network spanning the molecule. Motion which does occur, such as rotation about the molecular axis and internal rotations, is averaged over many cycles and conformations when observed in the NMR time scale [51-52]. The motional averaging causes dipole couplings between pairs of protium nuclei in a molecule to be identical from molecule to molecule, creating identical spin networks on each molecule. The allowed motions and conformations for liquid crystal molecules is dependent upon the many liquid crystalline mesophases. The two mesophases of concern in this work are the nematic and smectic A mesophases.

4.2.1 The Nematic Mesophase

The most commonly occurring and generally the first mesophase encountered upon cooling an isotropic liquid crystalline material is the nematic phase. This mesophase places fewer restrictions on molecular motion than any phase other than the isotropic phase. The molecular centers of mass translate isotropically, while the long molecular axis is constrained to be aligned parallel with an external magnetic field. In the absence of a strong magnetic field, the molecules will tend to aline with a nearby surface, or arbitrarily in the bulk. If the molecule does not possess a point of inflection, alignment is equally probable either parallel or anti-parallel to the director generated by an external field or surface. Thus, the nematic phase is neither ferroelectric or translationally ordered while it is orientationally ordered. Molecules rotate rapidly about their long axis, averaging intermolecular interactions as observed by NMR and allowing them to be modeled as cigar-shaped ellipsoids as depicted in

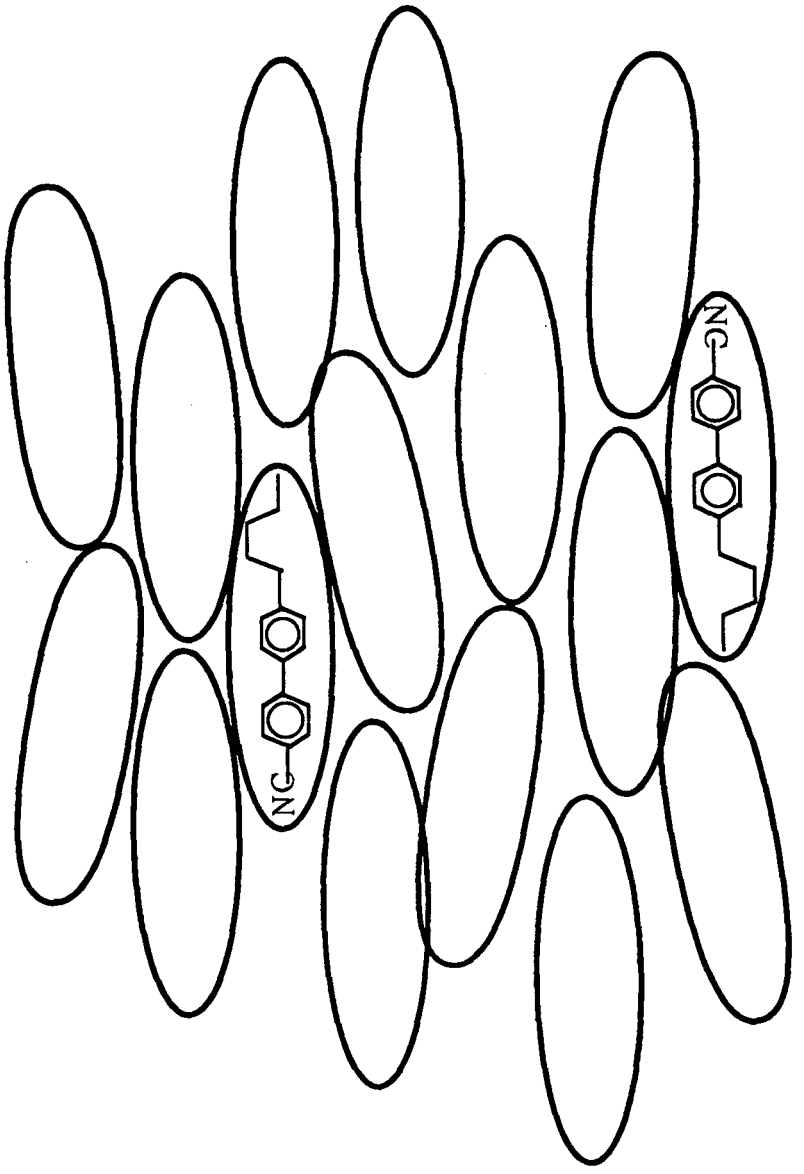

Figure 4.2. 5CB in the nematic mesophase.

Figure 4.2.

All of the liquid crystalline materials used in the experiments described later in this chapter possess a nematic phase. These phases either occur naturally at room temperature, or the nematic temperature range was lowered by adding a small amount of solvent.

4.2.2 The Smectic A Mesophase

Smectic A is the least ordered of the smectic mesophases, generally being the first, if any, smectic mesophase encountered upon cooling a nematic. Molecular centers of mass in a smectic A mesophase are restricted to move in a series of two dimensional planes normal to a director generated by either a surface or external field, in addition to possessing long range orientational order as in the nematic phase. The centers of mass are not correlated to one another within the plane of motion, and the molecules may aline either parallel or anti-parallel to the director. Rotation about the molecule's long axis and conversion between allowed conformers is rapid, averaging the dipole-dipole couplings as observed using NMR.

The only liquid crystalline material studied in a smectic A mesophase in this work was 4-octyl-4'-cyanobiphenyl. While this molecule has a length of ~22Å, the spacing between adjacent layers has been determined by x-ray diffraction [53] to be ~30Å, suggesting formation of one of the bilayer structures depicted in Figure 4.3.

4.3 Spin Cluster Geometries

Homonuclear dipole-dipole couplings are dependent upon the spatial arrangement of spins with respect to one another and the external magnetic field. Spin cluster geometry is in turn a function of both the molecules which comprise the cluster and the environment. Molecules in nematic and smectic liquid crystalline mesophases

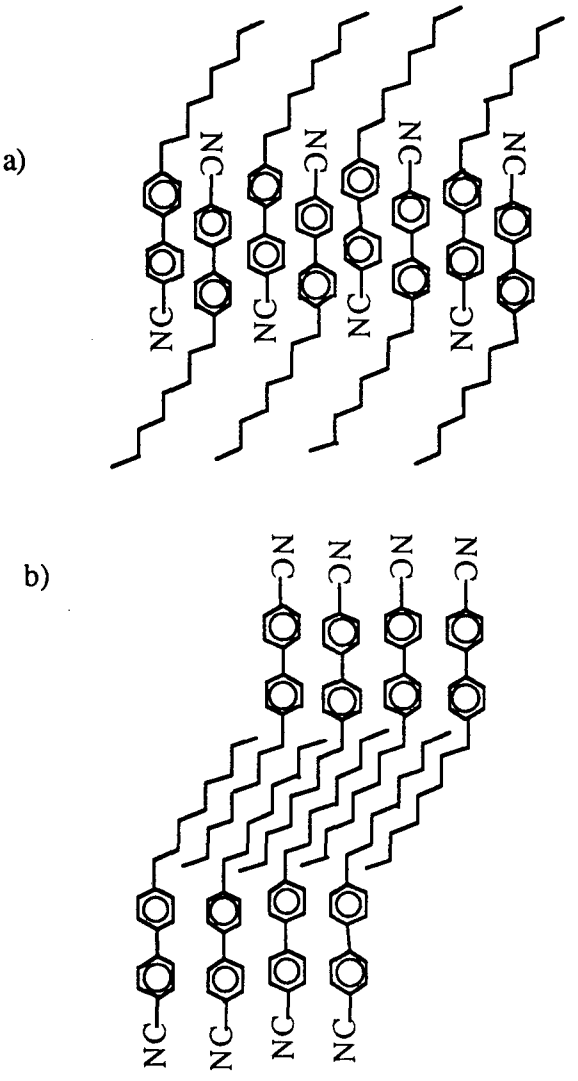

Figure 4.3. Possible bilayer structures for 8CB in the smectic A mesophase. Both are stablized by van der Waals interactions between the alkyl chains, requiring a bent molecular shape.

experience sufficient translational motion to average dipole-dipole couplings between spin pairs on different molecules to zero, limiting spin clusters to those upon single molecules and limiting spin cluster geometry to molecular geometry. The liquid crystal molecules examined as spin clusters in this work are 4-pentyl-4'-cyanobiphenyl (5CB) and 4-hexyl-4'-cyanobiphenyl (6CB) in the nematic mesophase and 4-octyl-4'-cyanobiphenyl (8CB) in the nematic and smectic A mesophases. The oriented alkane molecules examined as spin clusters in this work are n-hexane, n-octane, n-decane, and 5,6-d_4-n-decane. The cyanobiphenyl liquid crystals will be considered first, followed by the n-alkanes.

4.3.1 Cyanobiphenyl Liquid Crystals

Cyanobiphenyl liquid crystal molecules have polar 'heads' and nonpolar 'tails'. The polar head contains the cyano-aromatic part of the molecule and possess a strong electric dipole due to the cyano group. The tail contains the alkyl chain and is nonpolar. The long axis of the molecule tends to aline either parallel or anti-parallel to a director, an external magnetic field in the following experiments. All cyanobiphenyl liquid crystals with alkyl chains of nine or fewer carbons possess a nematic mesophase, and those with alkyl chains eight or more carbons in length possess a smectic A mesophase [54].

Both 5CB and 6CB posses nematic mesophases at room temperature, while the nematic temperature range of 8CB can be lowered to ~ 20 C by adding a small amount of deuterochloroform. Nematic liquid crystal molecules rotate about their long axis at a rate much faster than the NMR time scale [50], averaging the observed couplings between protium nuclei. These molecules also posses long range orientational order while translating isotropically through the sample. The combination of molecular orientation, isotropic translation, and rapid rotation about the long axis suggest modeling the molecules as cigar-shaped ellipsoids pointing parallel and anti-parallel to

the magnetic field. This motion would tend to restrict possible conformations of the alkyl tail of the molecule, making conformations which bend the molecule's long axis (e.g., all *trans*) unfavorable. Alkyl chains containing an odd number of carbons will tend to aline the final carbon-carbon bond with the external field, while chains containing an even number of carbon atoms will tend to aline the terminal C-C bond at an angle to the field. This effect on methyl alinement is depicted in Figure 4.4 and should be more pronounced for shorter alkyl chains, for there are fewer possible conformations and weaker van der Waals interactions in shorter alkyl chains.

8CB is normally found in the smectic A mesophase at room temperature. Molecules in a smectic A liquid crystal possess long range orientational order, alining their long molecular axis along an external magnetic field, and they also possess limited translational order, for the molecules are constrained to move in two dimensional sheets normal to the magnetic field with translation in the sheets being unconstrained. The polar nature of 8CB's cyano-aromatic head requires the formation of molecular bilayers in the sheets, both to allow the favorable electric dipole-dipole interactions and to make the mesophase non-ferroelectric. The existence of a molecular bilayer structure is indicated by a layer spacing (~30Å) [53] incommensurate with the molecular length (~22Å). Fitting an 8CB molecular bilayer in the measured layer spacing requires that the molecules assume a bent conformation, with the long axis of the alkyl chain being deflected ~35 degrees from the axis of the cyano-aromatic head. Such structures have been proposed for bulk 8CB from density measurements [55], and bent conformations of 8CB molecules have been observed directly using a scanning tunneling microscope on 8CB molecules adsorbed to a graphite surface [56]. A possible model based upon the polar cyano-aromatic heads forming the layer center [55], alternating orientation to

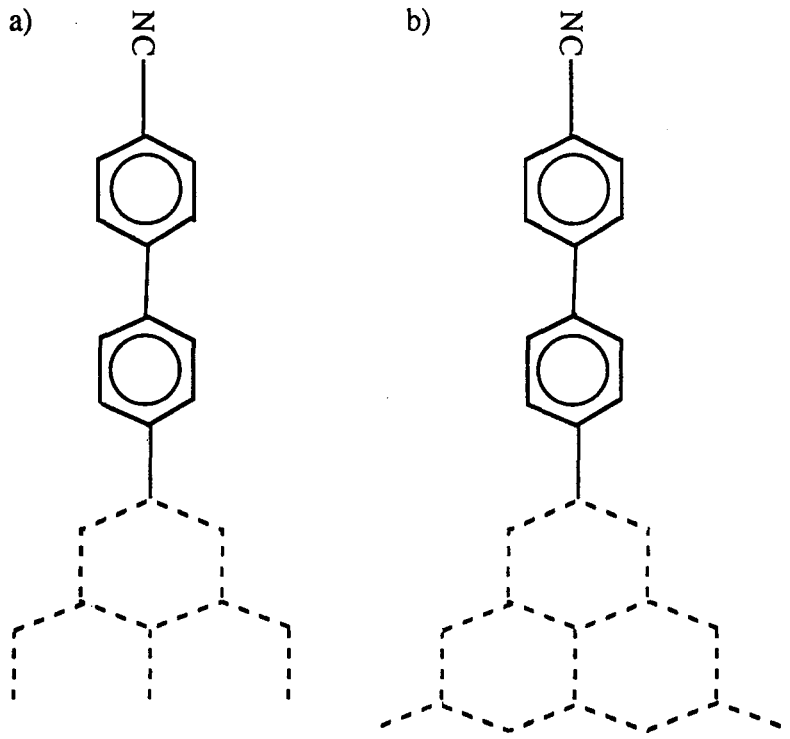

Figure 4.4. Diagrams illustrating possible conformations of alkyl chains in a) 5CB and b) 6CB. The dotted lines trace the possible orientations of C-C bonds in the alkyl tail, assuming the tail extends away from the cyanobiphenyl head. Chains containing an odd number of carbon atoms tend to orient the terminal C-C bond parallel to the director, while chains with an even number of carbon atoms orient the terminal C-C bond away from the director.

allow favorable electric dipole interaction with the nonpolar alkyl tails stabilizing the structure through van der Waals interactions, is depicted in Figure 4.5(a). An alternate model would pack the alkyl tails together in the layer center, lining up the cyano-aromatic heads along the layer boundaries, as depicted in Figure 4.5(b). Both packing arrangements require that the molecule be bent, with a 30 to 40 degree angle between the long axis of each part of the molecule, in order to create a layer spacing of ~30Å. This contrasts sharply with the expected average conformation of the same molecule in the nematic mesophase, where 8CB is, on average, assumed to be straight.

4.3.2 Oriented n-alkanes

The conformation of n-alkanes oriented in nematic liquid crystals has been studied extensively by use of 2-D NMR [57-59]. One product of these studies is a compilation of the homonuclear dipole-dipole couplings between protium nuclei in oriented n-hexane, n-octane, and n-decane. Prior determination of the dipole couplings between protium nuclei in a spin cluster generates the best possible test case for the study of spin cluster evolution under rf radiation, for the system is already fully determined.

Oriented n-alkane samples can be prepared by dissolving the alkane in p-pentylphenyl 2-chloro-4-(p-pentylbenzoyloxy)-benzoate, at a concentration of 20 mole % n-alkane to 80 mole % liquid crystal. The introduction of the n-alkane depresses the crystalline-nematic transition below room temperature, eliminating the need to heat the sample. The orientation of the liquid crystal molecules parallel to an external magnetic field tends to also aline the straight chain solutes, via collisions and van der Waals interactions.

The alkane molecules experience many conformations during the life time of an NMR experiment, so the observed interactions are averaged over the possible

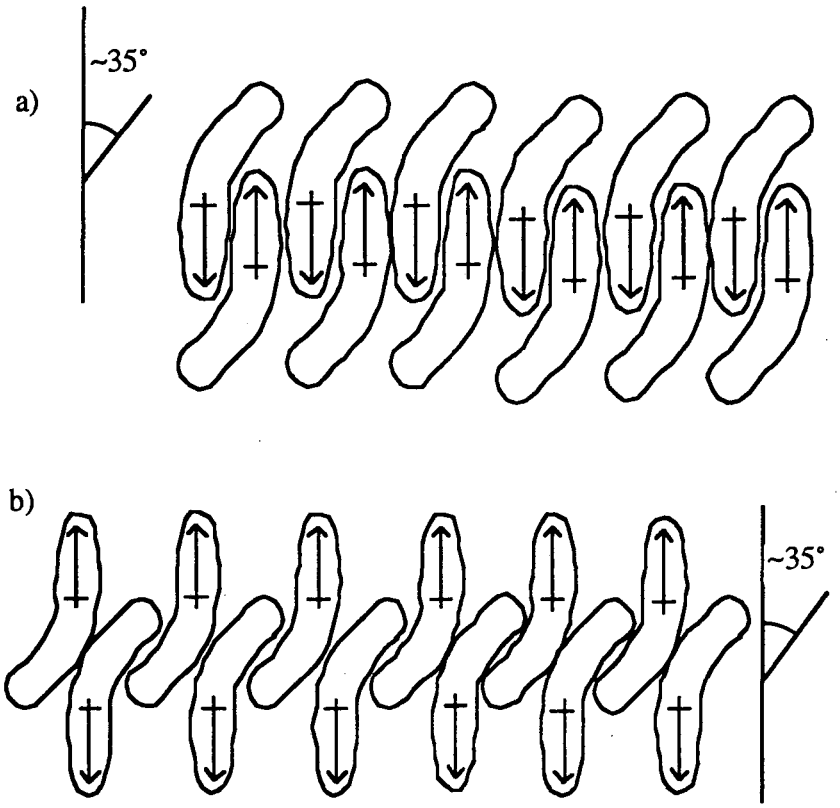

Figure 4.5. Possible bilayer structures for 8CB in the smectic A mesophase, emphasizing the molecular profile and electric dipole in each 8CB molecule.

a) Cyanoaromatic core and alkyl edges for optimal electric dipole interaction, and b) alkyl core and cyanoaromatic edges for optimal van der Waals interaction between alkyl chains.

conformations. Figure 4.6 depicts all *trans* n-hexane and n-octane with protium sites numbered and a some of the average dipole-dipole coupling strengths indicated, as reported in [57-58]. Generally, geminal protium nuclei are strongly coupled, followed by protium nuclei bonded to next nearest neighbor carbons, then those bonded to next next nearest neighbor carbons. Surprisingly, some of the weakest couplings are between protium nuclei bonded to neighboring carbon atoms. This is due to the internuclear vector between these protium sites being nearly alined along the 'magic' angle with respect to the external field [60], sharply reducing the dipole-dipole coupling. Also, the rotation of the terminal methyl groups on either end of the n-alkane reduces the dipole-dipole couplings experienced by protium nuclei bonded to these carbons, roughly cutting the geminal couplings in half and reducing couplings between methyl and methylene protium sites.

One of the samples contained 5,6-d_4-n-decane, depicted in Figure 4.7. Deuteration of the hydrogen sites on the central two carbon atoms of the straight chain hydrocarbon interrupts the spin network, and comparison of experimental data between this sample and n-decane should separate effects of the rotating methyl groups from the behavior of the strongly coupled methylene core.

4.4 Isolated Spin Clusters

Previously in this work it was stated that the evolution of the density matrix representing a spin cluster is determined by the effective Hamiltonian (e.g., $D_{ij}(I_{i+}I_{j+}+I_{i-}I_{j-})$), which is composed of a multiple-quantum transition operator and coupling constants between spin pairs, in this case the homonuclear dipole-dipole couplings. The purpose of this section is to examine exactly how the couplings between spins affect the evolution of the density matrix.

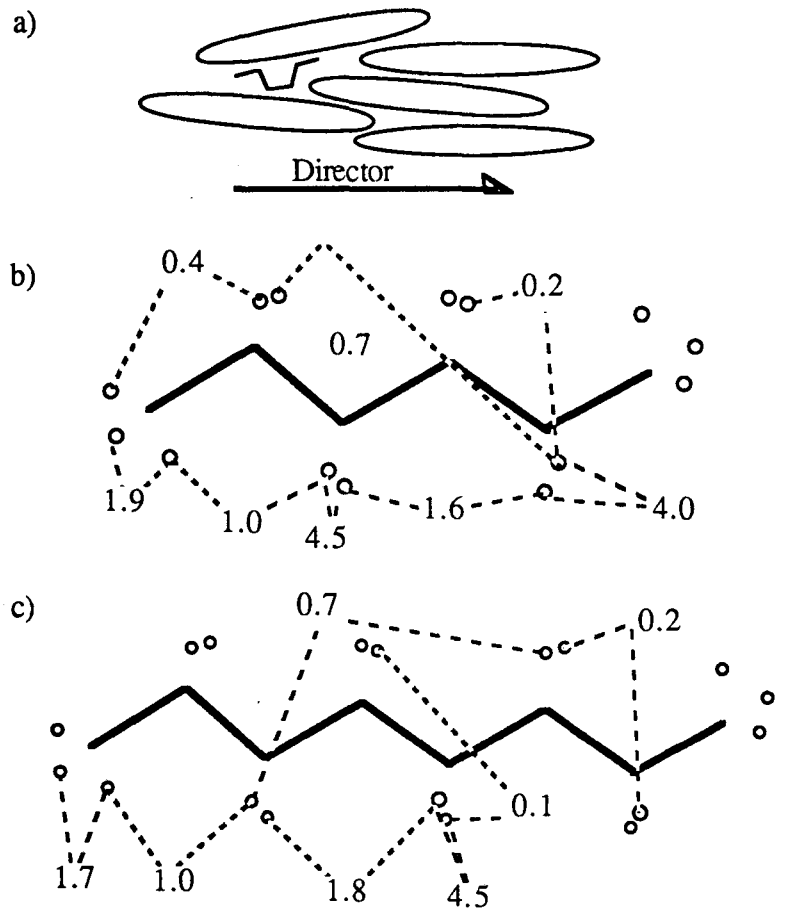

Figure 4.6. a) n-hexane oriented in a nematic liquid crystal b) Some typical dipole coupling magnitudes in KHz for protium pairs in oriented n-hexane[57]. The strongest couplings were selected between spins bonded to different carbon atoms.

c) Some dipole couplings in KHz for oriented n-octane[58], as in b).

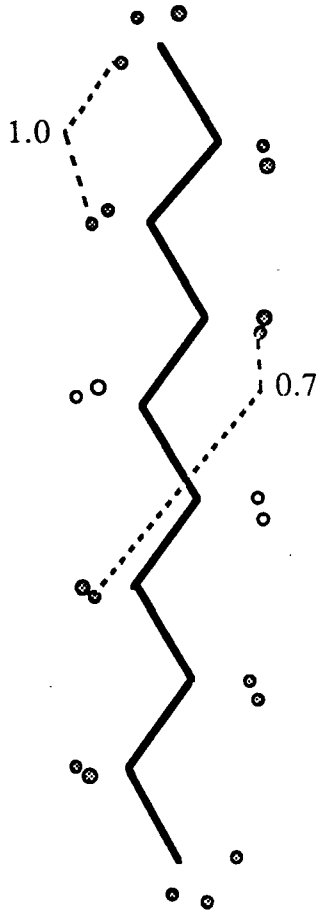

Figure 4.7. 5,5,6,6-deutero-n-decane, with protium sites represented by shaded circles and deuterium sites represented by open circles. Dipole couplings shown, in KHz, are the strongest between methyl-methylene spins and spins separated by the deuterated hydrogen sites.

As a starting point, consider the density matrix ρ for three dipole coupled spins one half depicted in Figure 4.8. There are three distinct dipole-dipole couplings which link all of the elements of ρ: D_{12}, D_{13}, and D_{23}. Elements of the same order n are coupled by the zero-quantum or flip-flop portion of the high-field homonuclear dipole-dipole Hamiltonian experienced during the evolution period, while elements of different orders $n \neq n'$ are coupled by multiple-quantum transition operators in the effective Hamiltonian created during the preparation period. The amplitude of each element ρ_{ij} will oscillate at a characteristic frequency ν_{ij}, but the coherence amplitude summed over each order of elements n will quickly dampen to an average value for all but the highest orders, as has been calculated for a six spin cluster [38]. This is due to the large number of elements contributing signal to each order n, especially when the difference between the size of the spin network, N, and the order of coherence, n, is sufficient to validate Stirling's approximation. Even with only three coupled spins one half there are ten zero-quantum transitions, fifteen one-quantum transitions, six two-quantum transitions, and one three-quantum transition.

The MQ-NMR spin counting experiment observes the sum of transition amplitudes according to transition order n, averaging out fluctuations of individual elements, as depicted in Figure 4.9(a). Amplitude of each coherence order in the Figure is normalized by the number of elements in each order, so the shading should become uniform as the spin cluster approaches the statistical limit at long excitation times. Evolution of the density matrix under a single-quantum Hamiltonian is depicted using this scheme in Figure 4.9(b). All amplitude is initially along the matrix diagonal, then entirely within the single-quantum elements after the first pulse. As the preparation period, and the rf irradiation, continues, higher order elements begin to acquire amplitude through the mediation of the dipole-dipole couplings. Eventually, the

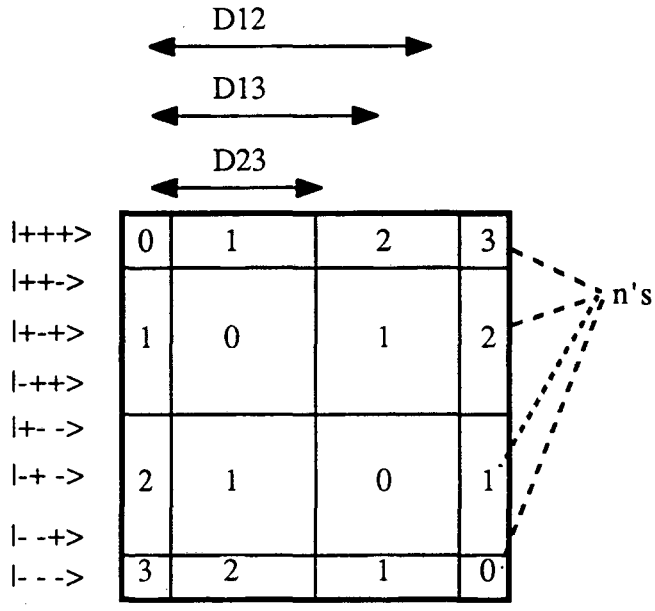

Figure 4.8. A diagram representing the density matrix of a three spins one half system. The eight basis states are listed along the left edge for reference, and the 64 density matrix elements are grouped by order n. The dipole-dipole couplings connect pairs of elements while under the influence of the preparation period's effective Hamiltonian, an even order selective Hamiltonian in this case. The couplings denoted above the matrix connect elements in the columns indicated by the arrows beneath the couplings.

amplitude of each coherence order will become constant and proportional to the number of elements in each order, represented by the uniform normalized amplitudes depicted in Figure 4.9(b).

Transfer of coherence amplitude between ρ_{ij}'s is mediated by the dipole-dipole couplings in the spin cluster. Transfer of coherence amplitude may occur directly between two elements, or the transfer may follow a less direct route. Direct transfer of coherence amplitude between two elements of ρ is illustrated in Figure 4.10(a). The spin cluster is composed of three spins one half, as in Figure 4.8, and the effective Hamiltonian is proportional to the double-quantum operator,

$$\overline{\mathcal{H}}_0 = \left\{\frac{1}{3}\right\} \sum_{i<j}^{N} D_{ij} \left(I_{i+}I_{j+} + I_{i-}I_{j-} \right) , \qquad (4.1)$$

where the proportionality constant is the dipole-dipole coupling constant for spins i and j. Coherence amplitude transfer between any two elements in this example depends upon a single coupling constant, such as the elements designated as α and β, and the coupling constant D_{12} in Figure 4.10(a). Indirect coupling schemes are possible, such as α to γ to δ to β, but all include the direct coupling constant (i.e., γ to δ coupling is identical to the α to β coupling). If this constant is large, the transfer will proceed quickly, if the constant is small, it will proceed slowly. Since the statistical limit is reached when all the elements are equally excited, the smallest coupling in a three spin cluster will determine when the statistical limit is reached.

The above behavior contrasts sharply with larger spin clusters, as depicted for a four spin cluster in Figure 4.10(b). While elements α and β are directly coupled by the dipole coupling between spins one and two, there are several indirect routes which

a)

b)

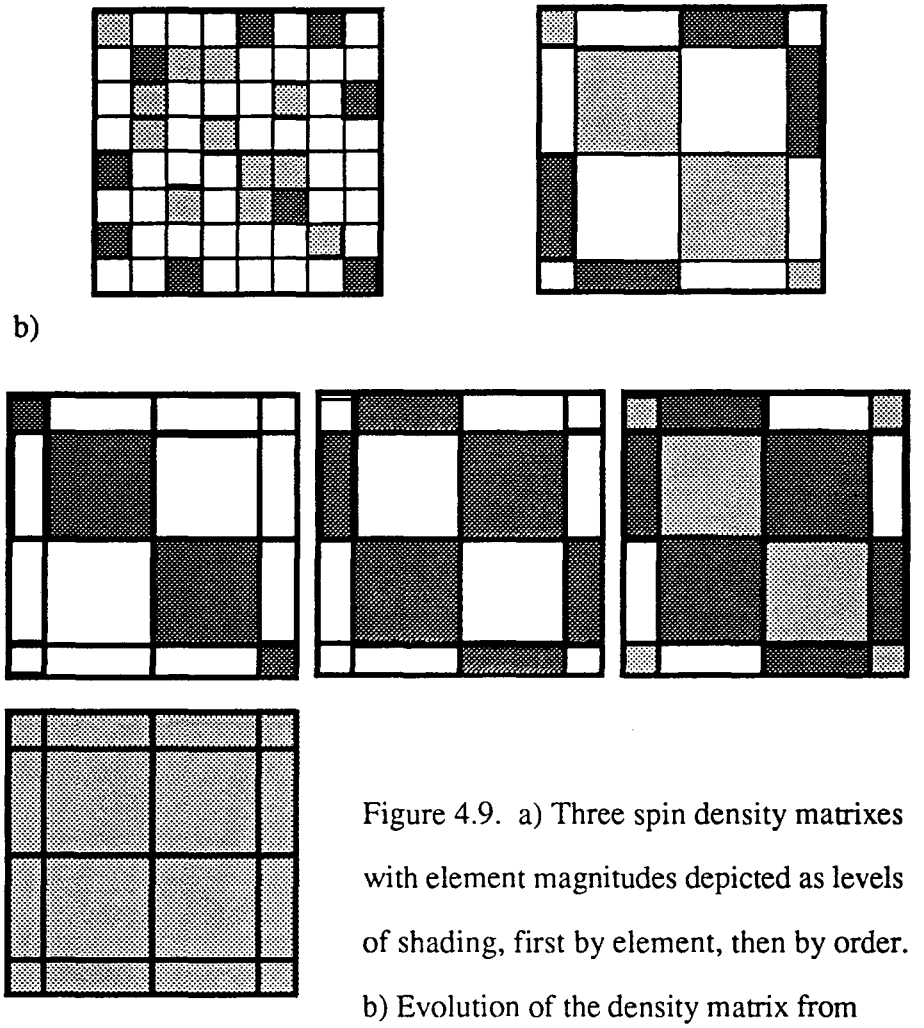

Figure 4.9. a) Three spin density matrixes with element magnitudes depicted as levels of shading, first by element, then by order. b) Evolution of the density matrix from initial polarization to statistical limit, as described in the text. Again, coherence magnitudes are represented by shading coherence orders.

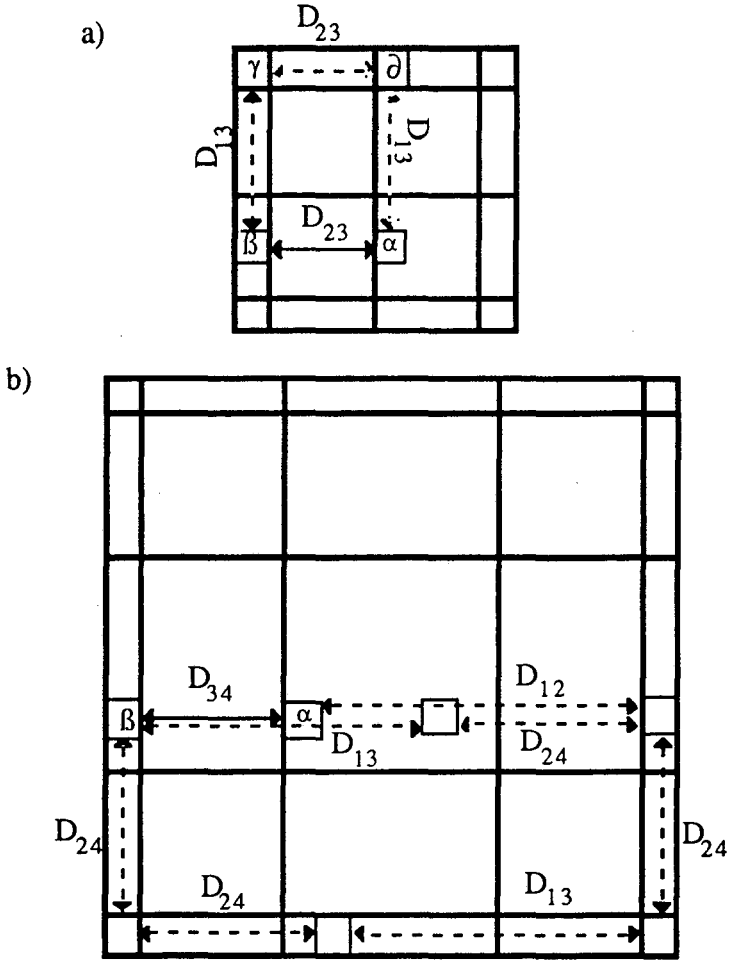

Figure 4.10. a) Density matrix for a three spin cluster with coupling routes between two elements shown. All possible routes between a and ß involve the direct coupling constant.

b) Density matrix for a four spin cluster with the direct coupling and two indirect coupling routes shown. Many indirect routes exist which do not involve the direct coupling constant.

do not involve D_{12}, two of which are designated with dotted lines in Figure 4.10(b).

Neither of these routes is limited by the coupling constant D_{12}, and similar routes can be found for any two elements connected by an allowed (i.e., $\Delta m=\pm 2$) transition. Therefore, while the density matrix of a three spin cluster approaches the statistical limit at a rate dominated by the slowest coupling present in the cluster, the density matrix evolution of larger clusters can 'bypass' weak couplings, quickening the approach to the statistical limit. Generally, larger spin clusters have more complex couplings of the spin network, and therefore more indirect coherence transfer routes. This leads to the evolution of ρ being dominated by the relatively strong couplings in larger clusters (i.e., $N > 4$).

4.5 Experiments

The experiments which follow were performed upon oriented molecules which are either linear or bent in shape. Dipole couplings between protium nuclei in n-alkanes have been measured [57-59], indicating that oriented linear hydrocarbons bear protium spin clusters which are strongly coupled between next nearest and next next nearest neighbor carbons. This network of strong dipole-dipole couplings should be sufficient to dominate the evolution of the density matrix as observed in the MQ-NMR spin counting experiment, for the statistical limit should be reached before the product of the preparation time and the relatively weak nearest neighbor couplings can become significant. A graph of the apparent cluster size N_{app} as a function of preparation time τ should show a uniform increase in N_{app} until the statistical limit is reached [37], assuming that relatively large couplings of approximately the same magnitude dominate the spin network, as depicted in Figure 4.11(a). A nonuniform rate of increase in

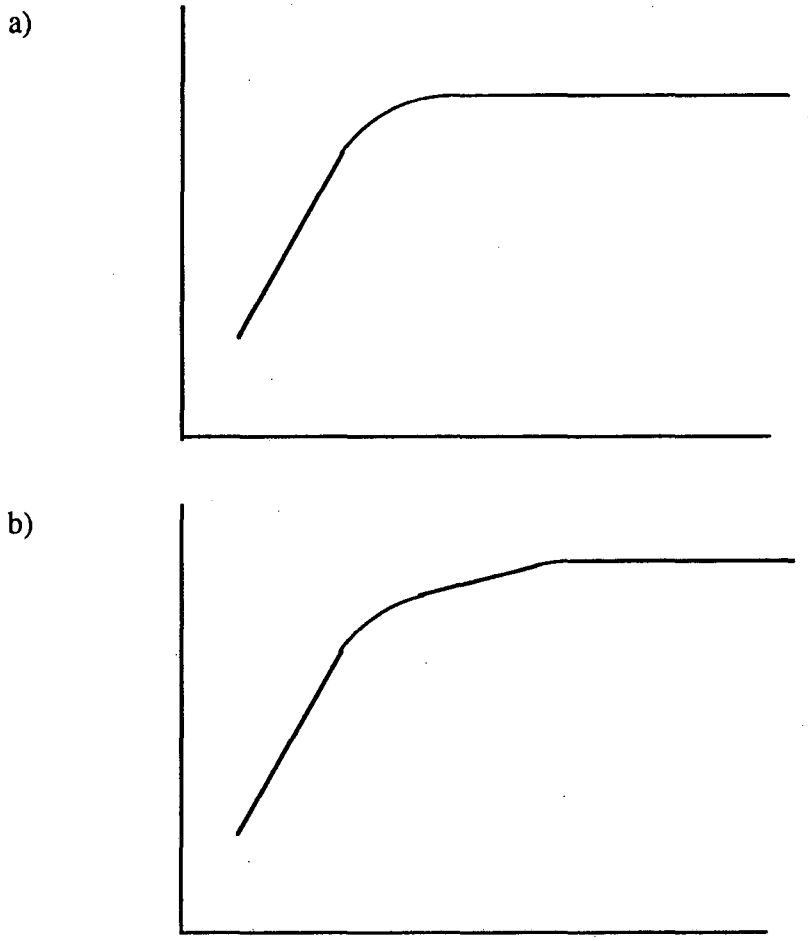

Figure 4.11. a) Expected behavior of N apparent as a function of preparation time for a collection of isolated spin clusters with uniform spin-spin coupling strength magnitude.
b) Expected behavior N apparent as a function of preparation time for a collection of isolated spin clusters with non-uniform spin-spin coupling strength magnitudes.

$N_{app}(\tau)$ is indicative of couplings of differing magnitudes dominating the observed behavior of the spin network, as depicted in Figure 4.11(b).

4.5.1 Napp(τ) for Oriented n-alkanes

Liquid crystalline solutions of 20 mol % n-alkane and 80 mol % p-pentylphenyl 2-chloro-4-(p-pentylbenzoyloxy)-benzoate were prepared and sealed in glass ampules. Selectively deuterated decane was obtained from Professor H. Zimmerman while naturally abundant n-hexane, n-octane and n-decane were commercially obtained. Sample temperature was maintained at 303 K by flowing N_2 gas through the temperature control apparatus (see appendix) and over the sample. MQ-NMR spin counting experiments were performed using the four (π) pulse sequence and tune up procedure described in chapter 3, with a π pulse length of 6 μs. This sequence creates an effective Hamiltonian during the preparation period proportional to the double quantum operator

$$\overline{\mathcal{H}}_0 = \left\{\frac{1}{3}\right\} \sum_{i<j}^{N} D_{ij} \left(I_{i+}I_{j+} + I_{i-}I_{j-} \right)$$

with a cycle time of 36 μs. The phase of the preparation period was incremented in 32 steps from 0 to 2π in order to generate the phase shift $\Delta\phi$. Each period form 0 to 2π contain two MQ interferogram echoes, and the signal $S(\Delta\phi)$ was averaged over sixteen MQ interferograms echoes ($0 \leq \Delta\phi \leq 16\pi$), as depicted in Figure 4.12. The detection period was altered to include a 2 ms delay between the tipping pulse and the spinlock pulses, in order to separate the signal from the alkane and the signal from the liquid crystal molecules, which have a much shorter T_2. Spectra were approximated by a gaussian least-squares fit, as described in chapter three, to obtain the apparent size of

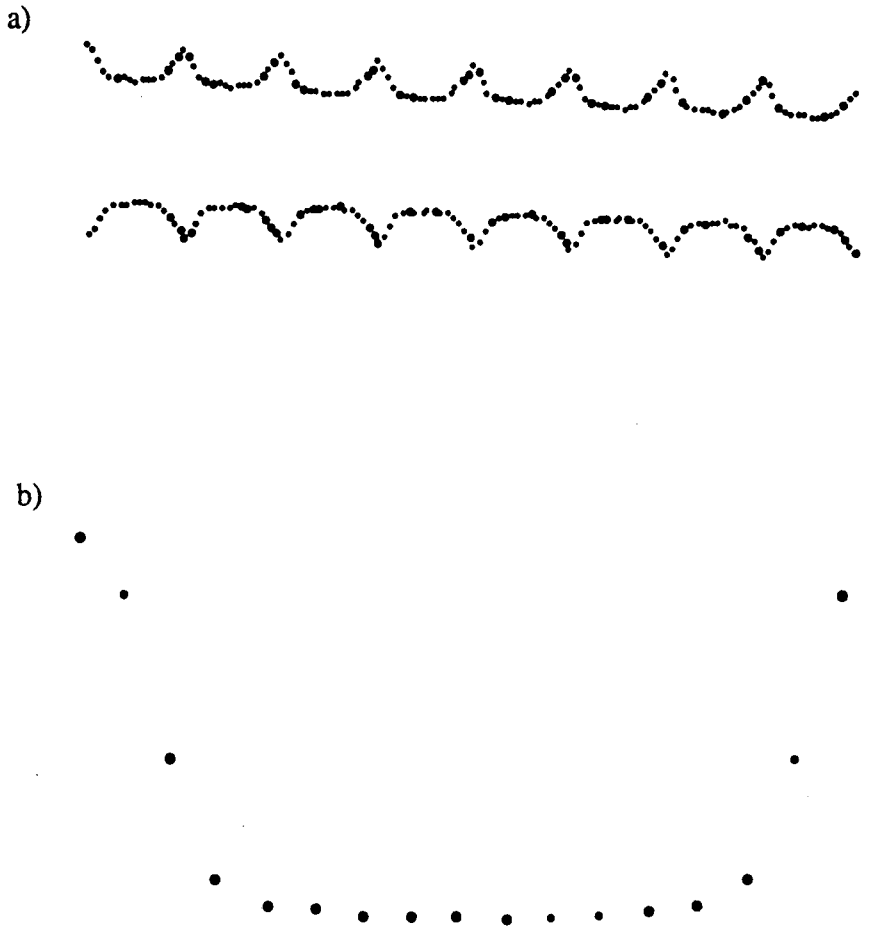

Figure 4.12. a) Simulated multiple-quantum interferograms as acquired in the experiments described in the text. The even order MQ signal inverts between the two interferograms while the error terms remain constant.

b) Difference between the two interferograms averaged to one echo (0 -> π). Subtracting one interferogram from the other reduces the effects of spectrometer drift.

the spin network as a function of preparation time, $N_{app}(\tau)$. The behavior of $N_{app}(\tau)$ was analyzed for each sample to determine the actual spin cluster size for oriented n-hexane, n-octane, n-decane, and 5,6-d_4-n-decane.

The first oriented molecule for study is n-hexane, depicted in Figure 4.6. This molecule bears a spin cluster of 14 protium nuclei, eight bonded to methylene carbons and six bonded to methyl carbons. As mentioned previously, dipole-dipole couplings have been measured for each unique pair of protium nuclei in this molecule [57]. Geminal protium nuclei bonded to methylene carbons are strongly coupled to one another (~4 kHz), while coupling between geminal protium nuclei bonded to the terminal carbons is weaker (~2 kHz), due to methyl rotation. The next stongest couplings are between protium nuclei on next nearest neighbor carbon atoms (~1.5 kHz), with methylene-methyl couplings being weaker than methylene-methylene couplings, in part due to methyl rotation. Couplings between protium nuclei bonded to next next nearest neighbor carbons are the strongest between sites on both sides of the long molecular axis (~ 0.6 kHz), with sites on nearest neighbor carbons being the most weakly coupled (~0.2 kHz).

The behavior of the apparent size of the spin network, N_{app}, in n-hexane as a function of preparation time is reported in Figure 4.13. The spin network appears to grow rapidly during the first ~200 μs of irradiation, followed by growth at a greatly lesser rate until ~1600 μs, when the cluster limit of 14 spins is reached. As discussed above, uneven growth of N_{app} in an isolated spin cluster is indicative of nonuniform coupling strengths throughout the cluster. The initial rapid growth of N_{app} is due to a region in the cluster containing relatively strongly coupled spins, while the slower growth is due to either a region containing more weakly coupled spins or due to weak

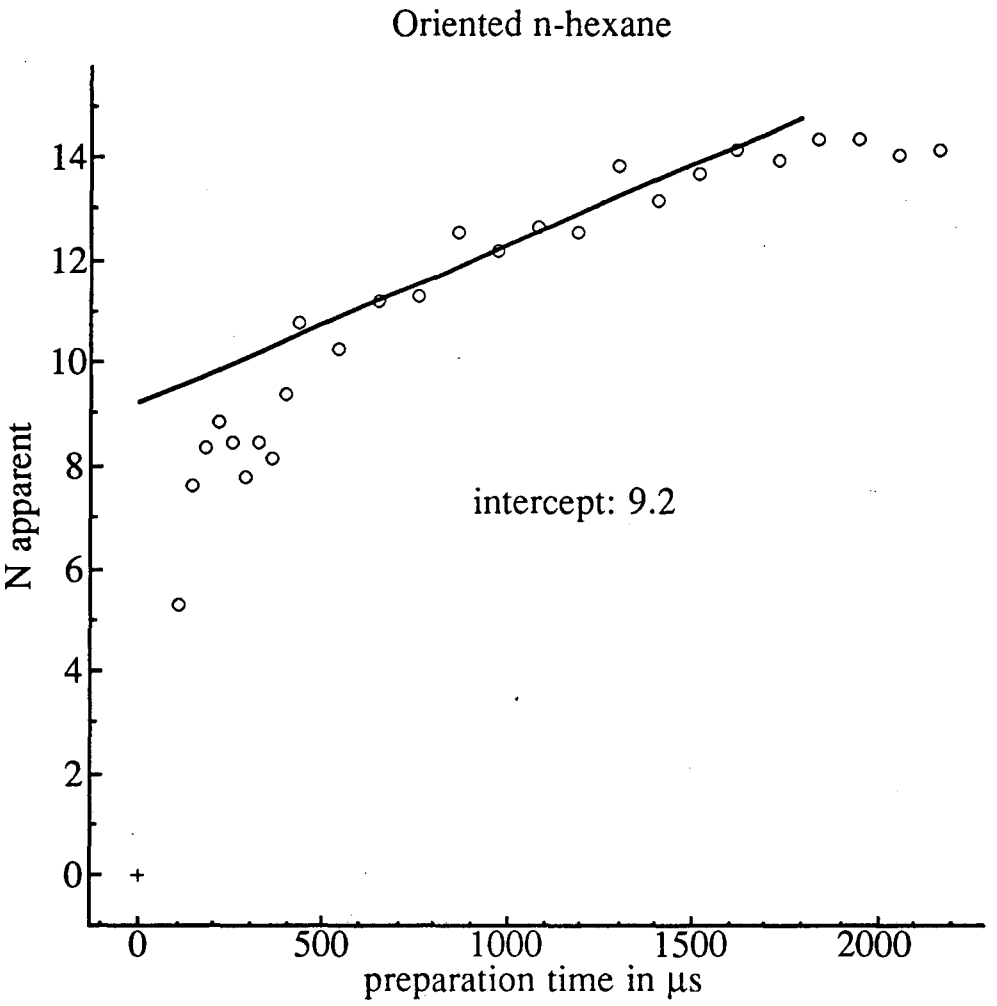

Figure 4.13. The apparent size of the spin network as a function of preparation time for n-hexane oriented in a nematic liquid crystal, as described in the text. Behavior at preparation times longer than ~1750 μs indicates a spin cluster of 14 protium nuclei, and the intercept of the least-squares fit line to times from 500μs - 1700μs indicates a strongly coupled subgroup of ~9 spins.

couplings between groups of strongly coupled spins. Strong couplings within a subgroup of spins on the molecule will cause the elements of ρ which describe the interaction of the spins in the subgroup to approach the statistical limit more rapidly than the elements describing interactions between spins outside the subgroup or between a spin within the subgroup and one outside it. Once the elements of the density matrix describing the subgroup reach the statistical limit, growth in the apparent size of the spin network ceases to be influenced by the strong couplings within the subgroup, leaving only the remaining relatively weaker couplings to increase N_{app}. The effects of the strong and weak couplings observed can be separated graphically by approximating the growth in N_{app} due to the weaker couplings with a linear least-squares fit of the data from 500 μs to 1500 μs in Figure 4.13, the region of steady slow growth in N_{app}. The intercept of the line approximating the slow growth in N_{app} indicates an average size of the spin subclusters, in this case ~ 9±1 spins. This corresponds well with the methylene 'core' of the n-hexane molecule, which contains eight spins. The more weakly coupled region(s) would then be the methyl groups at either end of the molecule, the evolution of which is apparently so slow as to not appear in the average subcluster size. In other words, the correlation of the methyl spins among themselves is no faster than the correlation between the methyl spins and the methylene 'core'.

There are two possible sources of this behavior, both of which probably contribute to the results reported above. First, the ends of the oriented molecule move more freely than the center [51], reducing the couplings between methyl and methylene spins. Second, the axis of free rotation in the methyl groups occurs at an angle to the external field, reducing the couplings between geminal spins in the groups by about half, as measured previously by Gochin, et al. [57]. The effect of weakened geminal

couplings in the methyl groups not only increases the time necessary to correlate all three spins, but it also decreases the coherence transfer rate between the methyl group and the rest of the molecule by reducing the strength of indirect coupling pathways, as discussed earlier in this chapter. While the couplings between methyl spins and the spins on the next nearest neighbor carbon are not much weaker than between next nearest neighbor methylene carbons, the geminal couplings in the methyl group are much weaker than those in the methylene group, reducing effect of indirect coupling mechanisms between the methyl spins and the methylene spins.

Similar behavior can be seen in $N_{app}(\tau)$ for n-octane, reported in Figure 4.14, and for n-decane, reported in Figure 4.15. In each case, there is a rapid initial rise in N_{app} corresponding to the methylene core of the molecule, followed by a slower rate of increase in N_{app} until the actual spin cluster size is reached. Dipole couplings between protium nuclei have been determined for both molecules [58-59], and have been found to be similar to those found in n-hexane. The strong couplings between geminal methylene spins cause them to correlate quickly, first to each other and then between other methylene sites. In other words, geminal methylene spins react to each other much more quickly than they react to spins on other carbons, so methylene groups correlate to one another as pairs of spins instead of as individual spins, speeding up the growth of N_{app}.

The last oriented n-alkane studied was 5,6-d_4-n-decane. The deuteration of the hydrogen sites on the central two carbon atoms was originally intended to separate the remaining protium nuclei into two weakly coupled spin clusters, for the strongest coupling between spins in the two clusters is ~ 0.7 kHz, weaker than the strongest methyl-methylene couplings. Instead, the results reported in Figure 4.16 for oriented

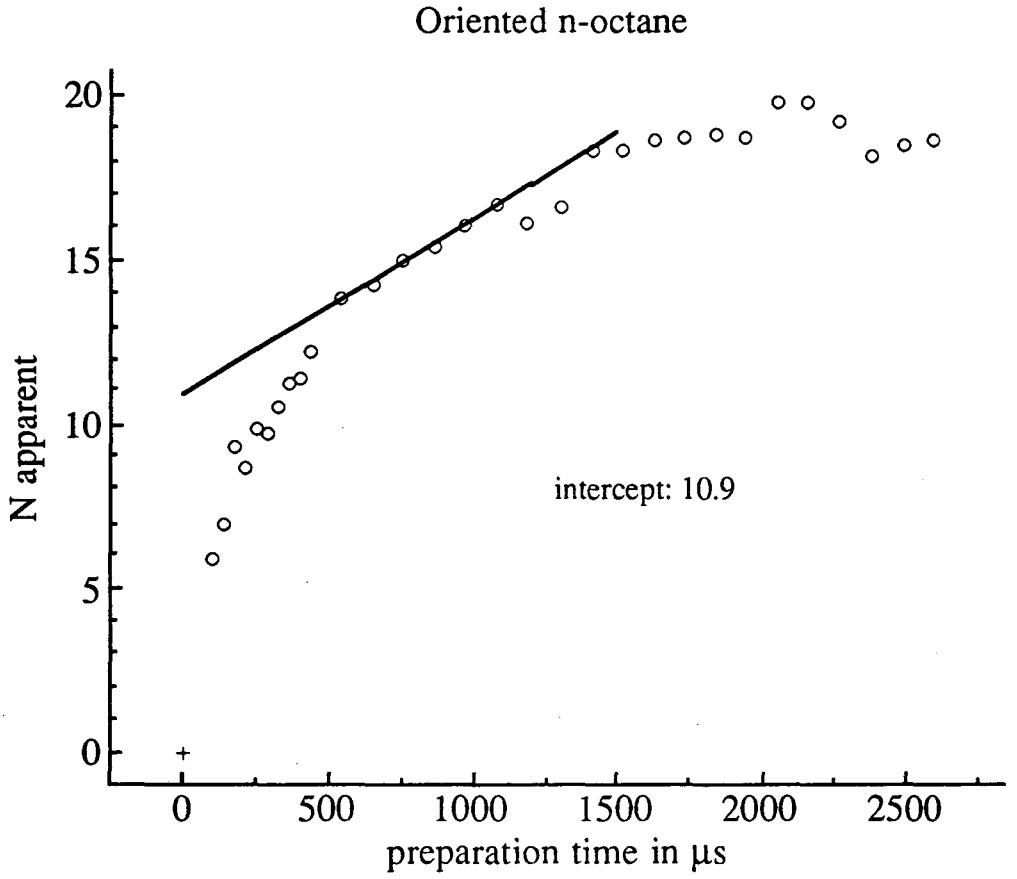

Figure 4.14. The apparent size of the spin network as a function of preparation time for n-octane oriented in a nematic liquid crystal, as described in the text. Behavior at preparation times longer than ~1500 μs indicates a spin cluster of 18-19 protium nuclei, and the intercept of the least-squares fit line to times from 600μs - 1300μs indicates a strongly coupled subgroup of ~11 spins.

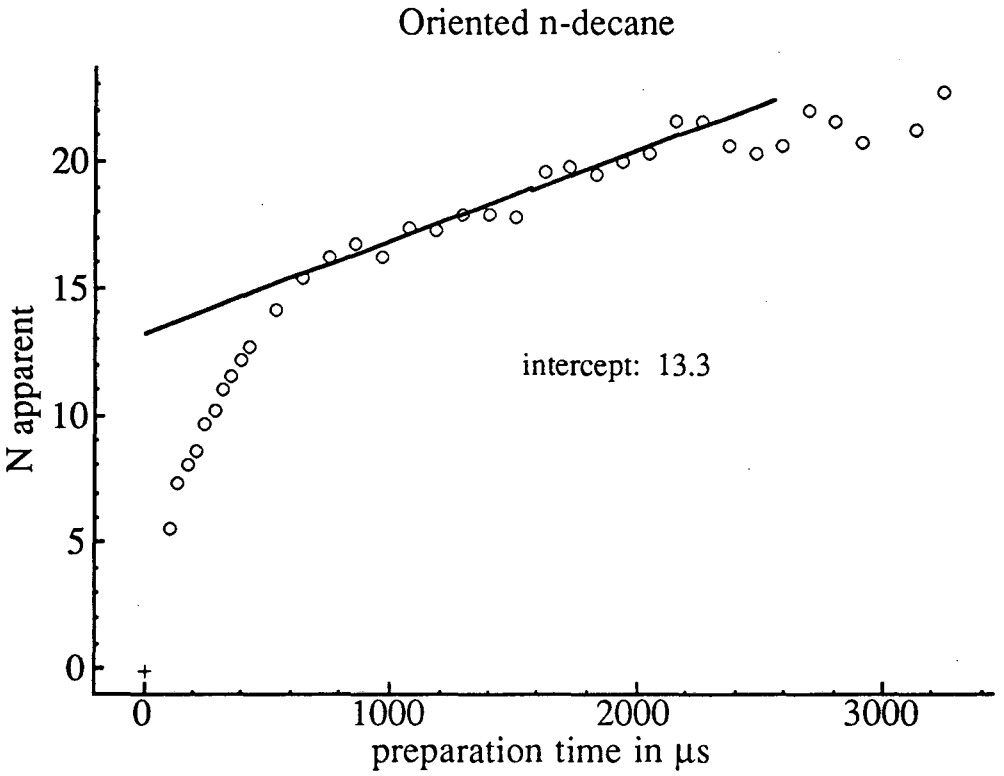

Figure 4.15. The apparent size of the spin network as a function of preparation time for n-decane oriented in a nematic liquid crystal, as described in the text. Behavior at preparation times longer than ~2300 μs indicates a spin cluster of 21-22 protium nuclei, and the intercept of the least-squares fit line to times from 800μs - 2300μs indicates a strongly coupled subgroup of ~13-14 spins.

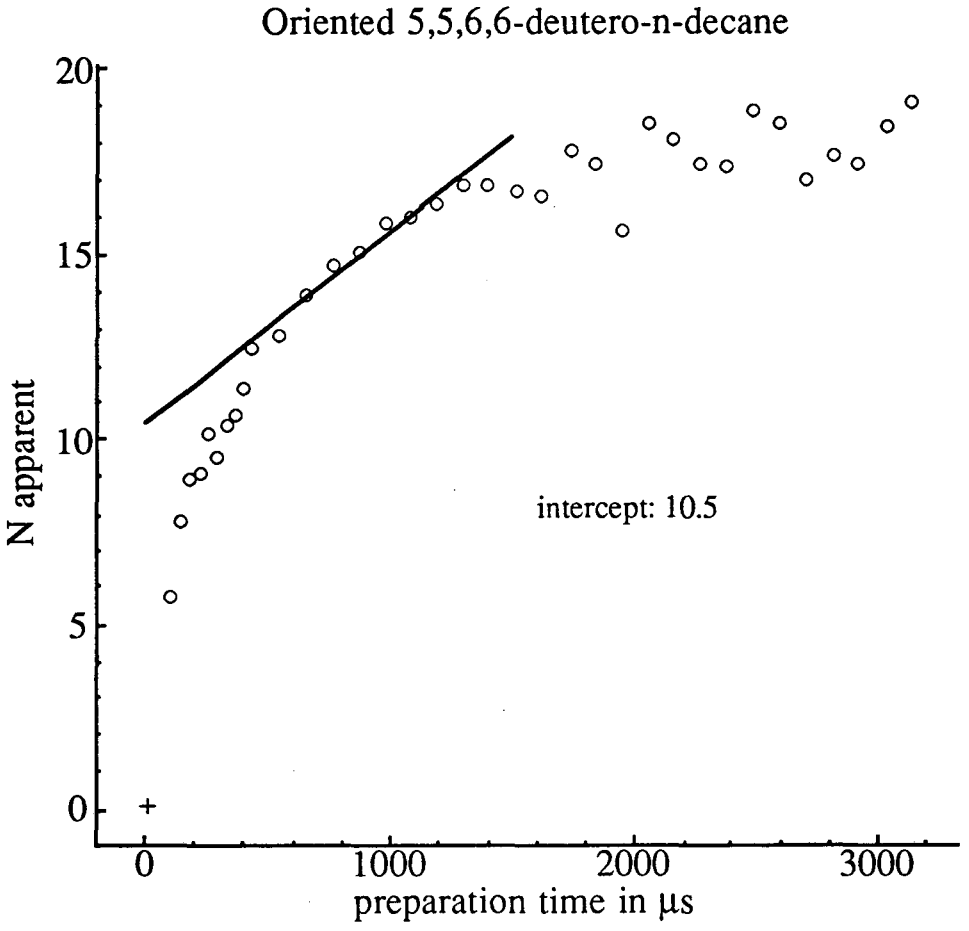

Figure 4.16. The apparent size of the spin network as a function of preparation time for 5,5,6,6-deutero-n-decane oriented in a nematic liquid crystal, as described in the text. Behavior at preparation times longer than ~1500 μs indicates a spin cluster of 17-19 protium nuclei, and the intercept of the least-squares fit line to times from 400μs - 1300μs indicates a strongly coupled subgroup of ~10-11 spins.

5,6-d_4-n-decane illustrate the importance of indirect coupling mechanisms in the approach to the statistical limit. The behavior observed is similar to that for the n-alkanes with hydrogen isotopes at natural abundance. The major difference is a decrease in the initial rate of increase in N_{app}, indicating weaker coupling within the methylene core of the molecule. The slower rate of increase after ~ 600 μs appears to be due to the methyl spins lack of strong geminal couplings, even though couplings between individual methyl spins and spins bonded to the next nearest neighbor carbon are stronger than those between individual spins bonded to the fourth and seventh carbon atoms.

4.5.2 $N_{app}(\tau)$ for Cyanobiphenyl Liquid Crystals

Liquid crystalline materials were prepared and sealed in glass envelopes. Systems chosen for study were 4-pentyl-4'-cyanobiphenyl (5CB), 4-hexyl-4'-cyanobiphenyl (6CB), 4-octyl-4'-cyanobiphenyl (8CB), and a solution containing 95 mole % 8CB and 5 mole % deuterochloroform ($CDCl_3$). These materials posses nematic, nematic, smectic A, and nematic mesophases at room temperature and will be referred to as 5CB, 6CB, smectic 8CB, and nematic 8CB, respectively. All cyanobiphenyl compounds were commercially obtained from BDH Chemical Corporation. Sample temperature was regulated by passing dry N_2 gas through the temperature control apparatus and over the sample. The eight ($\pi/2$) pulse sequence of Baum and Pines was used to create an effective Hamiltonian proportional to the double quantum operator during the preparation period. The preparation period was incremented by integer multiples of the cycle time, t_c, with the resulting MQ spectra approximated by a gaussian least-squares fit to determine $N_{app}(\tau)$. Cycle times were 58.8 μs, 66.0 μs, and 61.2 μs for the 5CB, 6CB, and both 8CB experiments,

respectively.

4.5.2.1 $N_{app}(\tau)$ for Nematic Cyanobiphenyl Liquid Crystals

The apparent cluster size as a function of preparation time, $N_{app}(\tau)$, was determined for 5CB and 6CB as reported in Figures 4.17(a&b). In both cases, the spin systems quickly approach the statistical limit with a relative uniform rise in the apparent cluster size. The observed cluster limit closely corresponds to the actual cluster size for both molecules, and the effect of methyl rotation appears small to negligible in both cases. The $N_{app}(\tau)$ curve for 5CB hints at a weaker correlation between the methyl spins and those on the rest of the molecule than between spin pairs in the rest of the molecule, while 6CB shows no signs of weak methyl couplings. Weakening of dipole couplings between methyl protium nuclei should be most apparent in 5CB, for alinement of the C_3 rotation axis along the external field fixes the angle between the internuclear vector of the spin pairs and the external field to ~90 degrees, reducing the dipole couplings to half the maximum. The methyl group on a 6CB molecule would aline ~75 degrees off the director, fixing the angle between the internuclear vector and the external field at ~15 degrees, keeping the dipole coupling between methyl spins near the maximum. The small size of a single methyl group and the absence of methyl orientation near the magic angle makes observation of methyl rotation difficult in both cases.

The apparent cluster size as a function of preparation time, $N_{app}(\tau)$, was determined for nematic 8CB and is reported in Figure 4.18(a). The spin system quickly approaches the statistical limit, and the observed cluster limit approximates the 25 hydrogen sites in each molecule. The smooth rise and plateau of $N_{app}(\tau)$ indicates

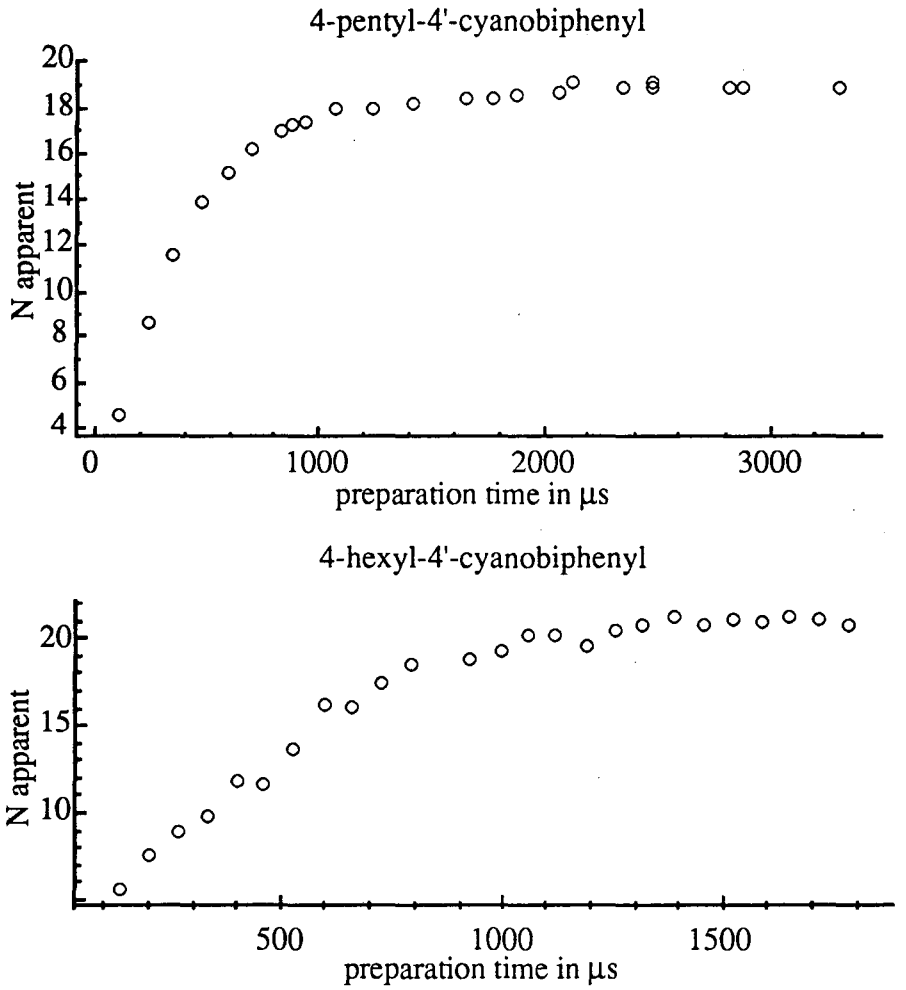

Figure 4.17. a) N apparent as a function of preparation time for 4-pentyl-4'cyanobiphenyl nematic liquid crystal
b) N apparent as a function of preparation time for 4-hexyl-4'-cyanobiphenyl nematic liquid crystal

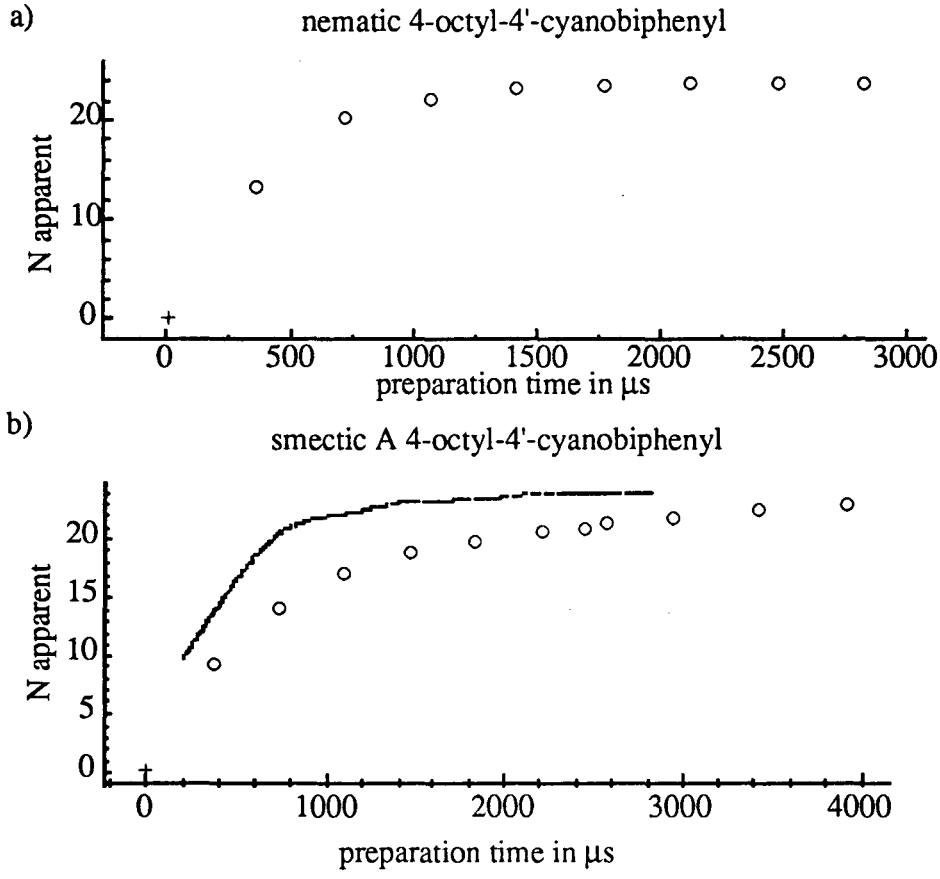

Figure 4.18 a) N apparent as a function of preparation time for 4-octyl-4'cyanobiphenyl nematic liquid crystal
b) N apparent as a function of preparation time for 4-octyl-4'-cyanobiphenyl smectic (A) liquid crystal

that dipole coupling strengths between spins in the molecule are fairly uniform over the different sections of the compound (i.e., cyano-aromatic and alkyl regions), as was seen above for the smaller nematic liquid crystalline molecules.

4.5.2.2 $N_{app}(\tau)$ for Smectic A Cyanobiphenyl Liquid Crystals

8CB posses two liquid crystalline mesophases: nematic and smectic A. The smectic mesophase occurs at room temperature for pure 8CB, with the nematic phase occurring at higher temperatures (i.e., ~34 C).

$N_{app}(\tau)$ for smectic 8CB is reported in Figure 4.18(b). The dotted curve in the approximates $N_{app}(\tau)$ for nematic 8CB as reported in Figure 4.18(a). Although smectic 8CB is a more ordered material than nematic 8CB, comparing $N_{app}(\tau)$ for both substances suggest that spins on the less ordered nematic molecules are more strongly coupled, or at least correlate faster to one another. Also, $N_{app}(\tau)$ for smectic 8CB indicates the presence of two distinct regions in the molecules: a more rapidly evolving region of ~16 spins and a more slowly evolving region of ~8 spins, corresponding to the 17 hydrogen sites on the alkyl tail and the 8 hydrogen sites on the polar head. The weakened interaction between the two parts of the molecule is probably caused by alignment of one of the parts away from the external field. Slow evolution of the aromatic part of the spin network is probably due to the lack of geminal spin pairs to create indirect coherence transfer routes, as described earlier.

Probable bilayer structures either place the aromatic heads at the center of the layer, as proposed in [55] and depicted in Figure 4.5(a), or placing the intermeshed chains in the center with the polar groups parallel at the interfaces, as depicted in Figure 4.5(b). The former seems more likely, for the electric dipole-dipole interaction would be more favorable in this configuration. In both cases, the 8CB molecules assume a bent confirmation, alining the alkyl chain away from the director by an angle of ~35

degrees.

5

Hydrocarbon Molecules in NaY Zeolite

5.1 Introduction

The last chapter focused on the use of MQ-NMR spin counting to study isolated unimolecular spin clusters oriented in liquid crystalline mesophases. The spin clusters were isolated from one another due to the lack of long range translational order in two and three dimensions, for molecules in smectic A and nematic mesophases respectively. The experiments discussed in this chapter focus on the use of MQ-NMR spin counting to study the dispersion of aromatic hydrocarbons in NaY zeolite, a synthetic analog of faujacite.

The dispersion and distribution of aromatic hydrocarbons, especially benzene, in faujacitic zeolites have been studied by several techniques, among them neutron diffraction [61-62], several single-quantum NMR techniques [63-67], and Monte Carlo simulations [68]. Two different molecular distribution modes for benzene in faujacitic zeolites are suggested by the results of the above studies; a uniform distribution [63] as depicted in Figure 5.1(a), and an aggregated distribution [62] as depicted in Figure 5.1(b). It should be possible to determine the average number of molecules per supercage using MQ-NMR, since the zeolite matrix separates the guest molecules into molecular clusters. Determination of the average number of spins (i.e., protium nuclei) in each supercage over a range of guest molecule concentrations will indicate the actual distribution of aromatic molecules, for different distributions will have widely differing average spin cluster sizes.

Before discussing each series of experiments, it will be useful to review the

a)

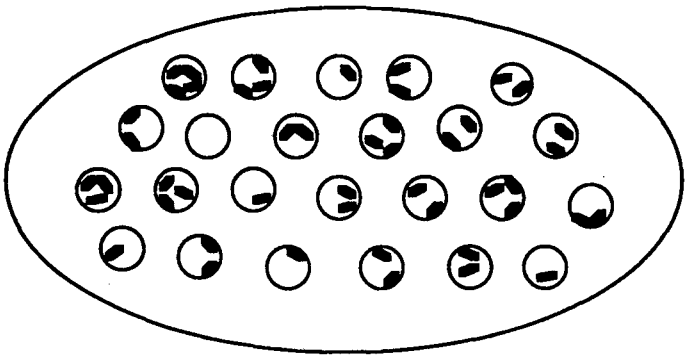

b)

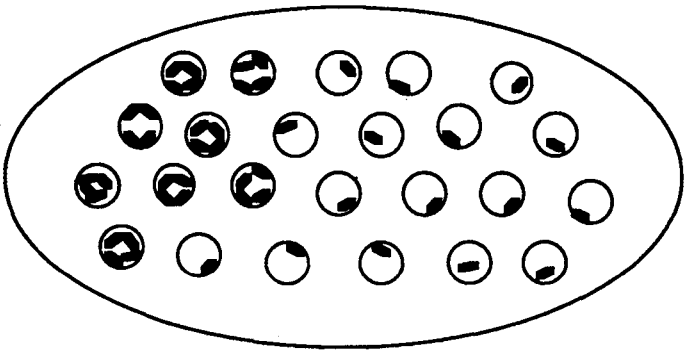

Figure 5.1. Schematic diagrams depicting possible distributions of benzene molecules in NaY zeolite. Both diagrams depict samples containing an average of two molecules per supercage.

a) Random distribution of molecules between supercages.

b) Aggregate distribution - a few cages contain a majority of the benzene molecules.

structure of both NaY zeolite and the aromatic guests used in the experiments (i.e., benzene and hexamethylbenzene). In particular, interactions between the guest molecules and the zeolite matrix due to electrostatic and steric considerations will be of interest. This will be followed by a description of the sample preparation method used to produce materials with desired guest molecule concentration and spin-lattice relaxation properties. The experimental conditions and observed results for samples containing varying concentrations of hexamethylbenzene in NaY zeolite will be presented, with a discussion of possible distribution modes congruent with the experimental results. The same will be done for samples containing varying concentrations of benzene in NaY zeolite, with particular attention devoted to determining if either of the suggested distribution modes depicted in Figure 5.1 match the observed behavior of the spin networks as a function of preparation time.

5.2 Structures and Interactions

Two substances, benzene and hexamethylbenzene, will be placed in NaY zeolite in varying concentrations. Benzene is a planar aromatic hydrocarbon possessing six-fold symmetry and six hydrogen atoms per molecule, with each molecule being about 7.4 Å wide in the plane normal to the C_6 axis [69]. Hexamethylbenzene is a planar aromatic hydrocarbon possessing six-fold symmetry and 18 hydrogen atoms per molecule, with each molecule being about 9.8 Å wide in the plane normal to the C_6 axis [69].

NaY (Sodium Y) zeolite is a synthetic aluminosilicate isomorphic with the naturally occurring faujacite, and is therefore said to have a faujacite structure. The faujacite structure is well known, having been determined by X-ray diffraction [71]. A schematic diagram of a faujacite supercage is shown in Figure 5.2(a), with the line

intersections representing a silicon or aluminum site and a bridging oxygen atom being located near the center of each line segment. The substitution of aluminum atoms for silicon atoms in the zeolite framework requires the presence of cations to maintain charge balance, Na^+ in the case of NaY zeolite. These ions are dispersed throughout the zeolite matrix at differing sites and are not strongly bound to any one site [70]. The discussion which follows is intended only as a brief review of structural aspects which are important to the latter spin counting experiments. One may find a more thorough description of faujacitic and other zeolites in Breck [72] and Barrar [74].

NaY zeolite is composed of a series of sodalite cages connected to one another by hexagonal prisms, as depicted in Figure 5.2(b) [74]. Sodalite cages occur in many zeolites, such as Zeolite A, and by using x-ray diffraction techniques are found to be 8.9 Å across [71]. Sodalite cages are hollow, but with apertures < 3 Å wide neither benzene or hexamethylbenzene can fit inside the cage. The prisms are smaller yet, with little open space for guest molecules. However, the open structure of faujacite allows guest molecules to move over the surfaces of both structures. The void between, and defined by, the sodalite cage network is called the supercage, also depicted in Figure 5.2(b) [74]. Guest/host interactions within the supercages are of great interest, in part due to the importance of faujacitic zeolites in the catalytic cracking and separation of aromatic hydrocarbons. Supercages with their adjoining windows comprise the accessible volume for both benzene and hexamethylbenzene in faujacitic zeolites. A supercage is roughly 13 Å across with the apertures or 'windows' between supercages being about 7.4 Å wide [71].

Each supercage contains four cationic Na^+ binding sites, known as S_{II} sites [73]. These sites are located on the faces of four sodalite cages in the surrounding framework, arranged at the vertices of a tetrahedron. The physisorption of an aromatic molecule here is favorable due to the tendency of Na^+ ions to occupy the sodalite cage

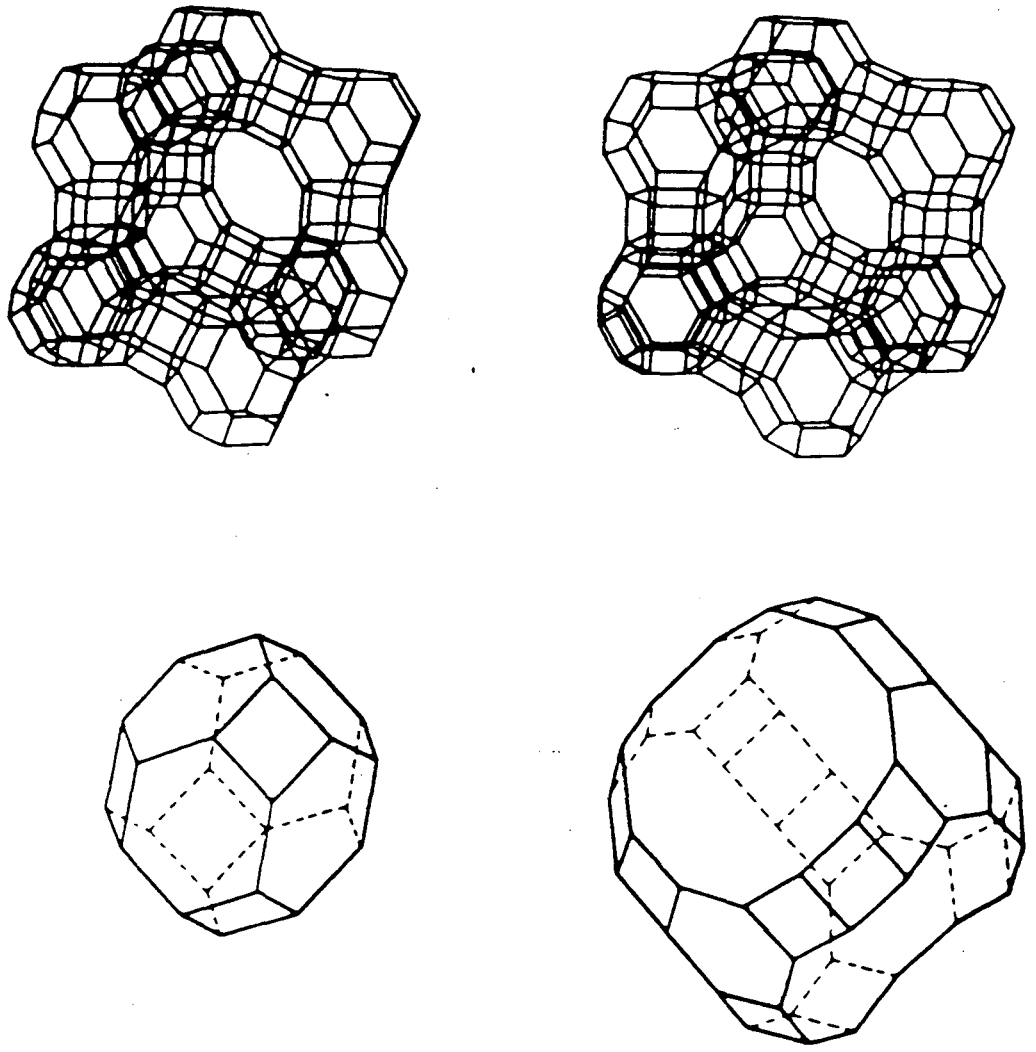

Figure 5.2. a) Stereo images of the framework structure for faujacite, viewed along the [111] axis (from ref. [74]).

b) Framework structures of a sodalite cage and a supercage. An S_{II} site is located at the center of each of the four hexagons in the supercage framework structure (from ref. [74]).

aperture at this site. Interaction between the cation and the polarizable electron cloud of an aromatic molecule will bind both the ion and the molecule to the site, for the Na^+ ions are also attracted to the oxygen atoms that ring the sodalite cage aperture. Benzene occupation of S_{II} sites in NaY zeolite has been predicted by Monte Carlo simulations [68] and directly observed in neutron diffraction experiments [61].

Each supercage also shares a window with each of the four surrounding supercages, and each of these windows is a potential physisorption site [72]. Here the attractive potential is due to the oxygen atoms which ring the large aperture, similar to the central void of a crown ether. This window site (W) interacts with the edges of aromatic molecules approximately the same size as the window, such as benzene. Benzene occupation of W sites in NaY zeolite has also been predicted by Monte Carlo simulation [68] and observed by neutron diffraction [61], but in both cases the occupancy the W sites was found to be less favorable than occupancy of the S_{II} sites.

Additionally, the Monte Carlo simulations of benzene molecular dynamics in NaY zeolite referred to above predict rapid rotation of the benzene molecule about its C_6 axis and translation of the benzene molecule from site to site along the zeolite surface, avoiding the center of the supercage. The guest molecules can be pictured as diffusing randomly through the accessible regions of the zeolite matrix along the matrix surface. This compares well with ^{13}C studies of benzene in NaY zeolite [63], which suggest a quasi-uniform distribution of guest molecules throughout the zeolite. The suggested distribution is quasi-uniform in that the observed results could be explained by either a uniform or rapidly averaging random distribution of molecules.

A small angle neutron diffraction study of benzene in NaY zeolite [62] suggests a different distribution of guests between supercages. This study found evidence of the formation of molecular aggregations at average concentrations of more

than one guest molecule per supercage. In order for this to be true, benzene molecules would initially spread uniformly throughout the zeolite matrix until every supercage contained one guest molecule, then additional guest molecules would aggregate at sites centered upon a few supercages, as depicted in Figure 5.1(b).

5.3 Experiments

5.3.1 Sample Preparation

The NaY zeolite used in this study was purchased from Union Carbide (LZY-52). The guest-NaY zeolite samples were prepared in 8mm pyrex tubes connected to a vacuum apparatus through a teflon high-vacuum stopcock. Before addition of the adsorbate species, the NaY samples were dehydrated in the pyrex tubes by heating at 723 K under vacuum (ca. 10^{-5} torr) overnight. After dehydration, a known amount of either benzene or hexamethylbenzene was introduced to the zeolite to achieve the desired bulk concentration. Adsorbate loadings were calculated from mass balances utilizing NaY supercage density and the masses of zeolite, hexamethylbenzene and benzene. Guest substances were introduced to the NaY zeolite samples at room temperature either in a glove box filled with dry nitrogen gas, in the case of benzene, or by mechanical transfer from a side arm while under vacuum, in the case of hexamethylbenzene. The samples were then placed in a furnace equipped with a programmable temperature controller and reheated to assure an even macroscopic distribution of adsorbate molecules throughout the zeolite matrix [75]. After re-evacuating each sample, oxygen gas was introduced to the samples containing benzene to shorten the spin-lattice relaxation times of the protium nuclei in adsorbed molecules at reduced temperatures. Each 8mm sample tube was then flame sealed while the majority of the sample was immersed in a liquid N_2 bath.

5.3.2 $N_{app}(\tau)$ for Hexamethylbenzene in NaY Zeolite

NaY zeolite samples were prepared containing a bulk average of 0.5, 1.0, and 2.0 hexamethylbenzene molecules per supercage. All experiments were performed at 303 ±1 K, with temperature regulation achieved by flowing dry N_2 gas through the temperature control apparatus and over the sample. The eight ($\pi/2$) pulse even-order selective sequence of Baum et al [37] was used to create an effective Hamiltonian during the preparation period proportional to the double quantum operator:

$$\mathcal{H} = 1/3 \sum D_{ij}(I_{i+}I_{j+}+I_{i-}I_{j-}),$$

with a $\pi/2$ pulse length of 3.0 μs and a cycle time t_c of 66 μs. The phase of the preparation period was incremented in 32 steps from 0 to 2π in order to generate the phase shift $\Delta\phi$. Each period from 0 to 2π contained two MQ interferogram echoes, and the signal $S(\Delta\phi)$ was averaged over sixteen MQ interferogram echoes ($0 \leq \Delta\phi \leq 16\pi$), as depicted in Figure 5.3. Spectra were approximated by a gaussian least-square fit, as described in chapter three with modifications detailed below, to obtain the apparent size of the spin network as a function of preparation time, $N_{app}(\tau)$. The behavior of $N_{app}(\tau)$ was analyzed for each sample to determine the average spin cluster size as a function of hexamethylbenzene concentration in order to find possible guest distributions for hexamethylbenzene in NaY zeolite at various loadings.

Protium nuclei on hexamethylbenzene molecules disbursed within NaY zeolite do not approximate ideal isolated spin clusters as well as spins on molecules oriented in liquid crystalline mesophases. The dispersion of hexamethylbenzene within the zeolite

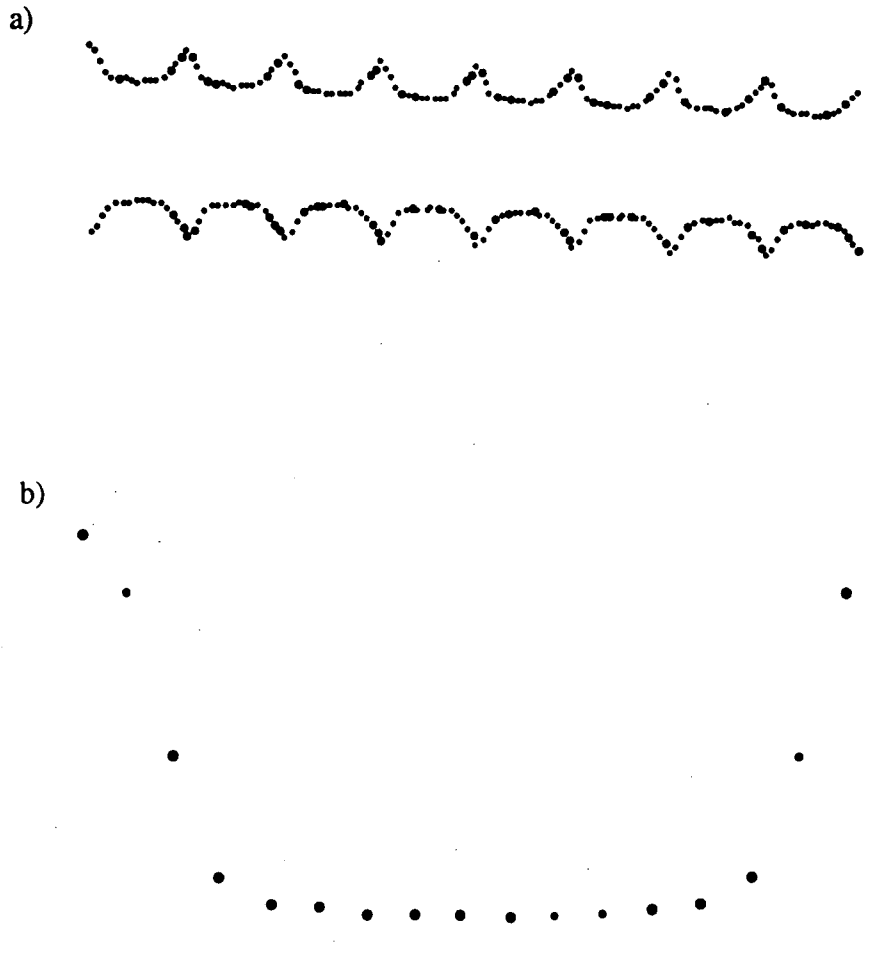

Figure 5.3. a) Simulated multiple-quantum interferograms as acquired in the experiments described in the text. The even order MQ signal inverts between the two interferograms while the error terms remain constant.

b) Difference between the two interferograms averaged to one echo (0 -> π). Subtracting one interferogram from the other reduces the effects of spectrometer drift.

is not trivial, for the diameter of the guest molecule is ~ 2 Å larger than the room temperature diameter of the windows between supercages. The actual clearance between supercages is somewhat larger, due to lattice distortions and vibrations, as explained in ref. [73]. The samples must be heated to 573 K for four hours to assure an even macroscopic distribution of the adsorbate throughout the zeolite [75]. Even then, it is possible that a small amount of hexamethylbenzene is still adsorbed only to the external surface of the zeolite crystallites, generating a continuous spin network in addition to the spatially isolated spin networks within the zeolite supercages. The spin clusters themselves are more complex than was found for spin clusters oriented in liquid crystals. First, they are not truly isolated, for physical separation of the spin clusters into separate supercages only reduces the dipole couplings between spins in different molecular clusters, whereas the translational motion of oriented molecules in a liquid crystal averages the couplings between spins on different molecules to zero. Additionally, the dipole couplings between pairs of spins vary from cluster to cluster, for the microcrystalline zeolite matrix provides no long range orientational order for the adsorbate molecules. The variation in spin couplings between clusters will cause the spin networks to approach the statistical limit at different rates, so the observed N_{app} will be averaged over spin networks at varying degrees of evolution toward the statistical limit.

The influence of two of the above mentioned non-idealities can be observed in the MQ spectrum of hexamethylbenzene in NaY zeolite at an average concentration of two guest molecules per supercage, reported in Figure 5.4(a). The circles represent the MQ transition peak intensities for each even order, $2 \leq n \leq 16$. Note that the two quantum intensity is much higher than would be found in a gaussian distribution, due to the presence of spin clusters with couplings much weaker than average due to molecular orientation. The seven higher order points appear to be well

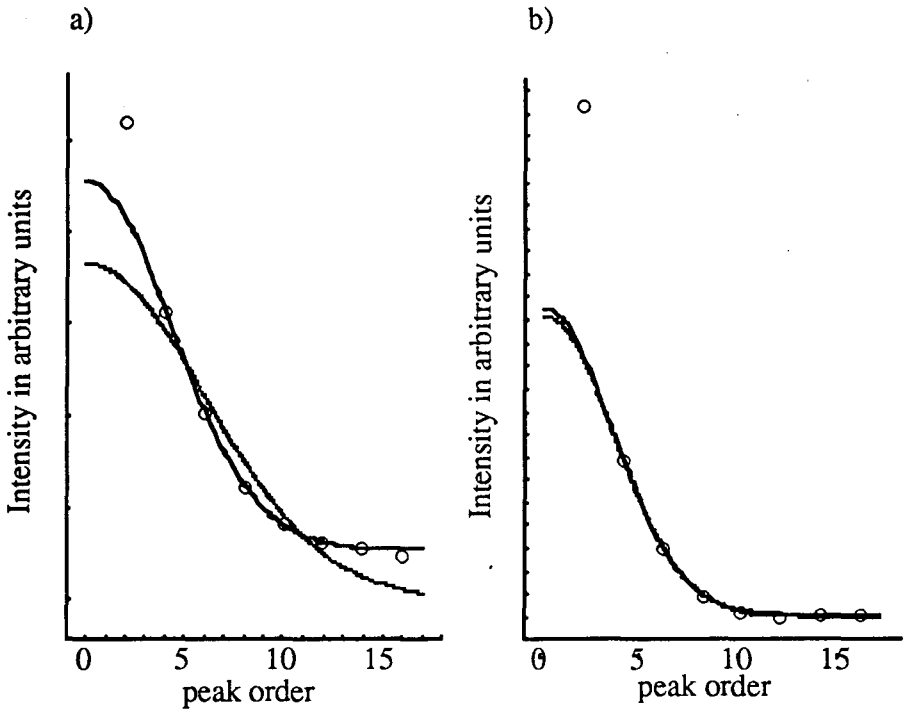

Figure 5.4. MQ spectra and gaussian least-squares fits for:

a) NaY zeolite with an average of 2HMB molecules per supercage, and

b) NaY zeolite with an average of 1 HMB molecule per supercage.

In both cases, the displayed curves were determined with and without a constant offset, as described in text.

approximated by a gaussian curve, so it will be assumed that only n = 2 order transition intensities are strongly affected by the variation in molecular orientation. A gaussian least-squares fit of the seven higher order transition intensity sums is depicted by the dotted line. The inaccuracy of the fit is most likely due to the presence of a small amount of adsorbate located on the external surfaces of the zeolite crystallites, for this behavior is not seen at lower guest concentrations, as shown in Figure 5.4(b). The spins located on the external surface of the crystallites will form an effectively infinite spin network, with transition order intensities of equal magnitude (i.e., an infinitely broad gaussian). The effects of the much larger exterior spin network may be accounted for by adding an adjustable baseline parameter to the least-squares fitting routine. The resulting three parameter fit for the seven higher order MQ peak intensities is quite good and is depicted by the solid curve in Figure 5.4(a). The gaussian curve has a standard deviation of $(N_{app}/2)^{1/2}$, where N_{app} is the apparent cluster size of the spin clusters *in* the zeolite supercages, excluding those molecules which happen to be oriented with their C_6 axis inclined near the magic angle with respect to the external field.

Results of MQ-NMR spin counting experiments for hexamethylbenzene adsorbed in NaY zeolite are reported in Figure 5.5, with 5.1, 10.2 and 20.4 wt % hexamethylbenzene corresponding to bulk averages of 0.5, 1.0 and 2.0 guest molecules per supercage. Note the nearly identical behavior of $N_{app}(\tau)$ for the two lower loadings, indicating a primarily uniform distribution of adsorbate molecules between the supercages of the zeolite. A nonuniform distribution of adsorbate molecules is not indicated, for the doubling of the guest concentration between the two samples would then be expected to increase the average actual cluster size of the second sample. Both curves indicate an actual cluster size of about 24 spins, comparing

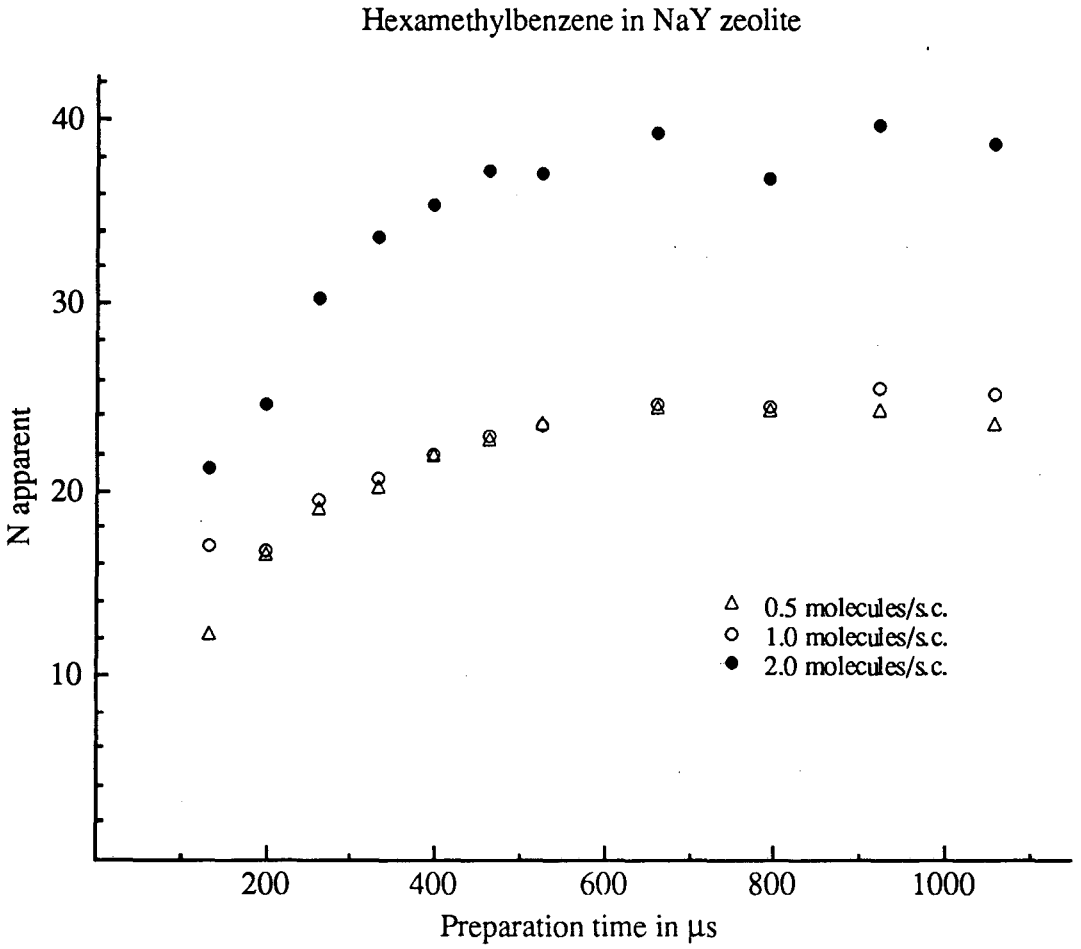

Figure 5.5. N apparent as a function of preparation time for NaY zeolite samples containing bulk averages of one half, one, and two hexamethylbenzene molecules per supercage. Methods used to determine N apparent are described in the text.

favorably with an cluster size of 18 spins expected for unimolecular clusters. The discrepancy in size is possibly due to the use of MQ peak intensities of sufficiently high order that (N-n) < 6, where N is the cluster size and n is the transition order. For N=18, the two highest order MQ peak intensities satisfy the preceding condition, invalidating the assumption made in chapter three that Stirling's approximation holds for the points approximated by the gaussian least-squares fit. This should not be a problem for the sample containing a bulk average of two hexamethylbenzene molecules per supercage, for the highest observed transition order, 16, is well below the range of average cluster sizes expected, 36 and up. Indeed, the actual cluster size indicated by $N_{app}(\tau)$ for the sample containing 20.4 wt % hexamethylbenzene is about 38 spins, in good agreement with bimolecular hexamethylbenzene clusters containing 36 protium nuclei.

The above results indicate that the distribution of hexamethylbenzene molecules between faujacitic zeolite supercages is uniform, with each cage containing a single guest molecule before an appreciable number of the supercages become doubly occupied. The presence of guest molecules adsorbed to the exterior of the zeolite crystallites after extensive heat treatment for the sample containing 20.4 wt % hexamethylbenzene indicates that a maximum of two molecules may occupy each supercage. This is not surprising, due to the large size of hexamethylbenzene molecules and the repulsion of the aromatic centers on these molecules, as can be seen in the crystal structure of solid hexamethylbenzene [69].

5.3.3 $N_{app}(\tau)$ for Benzene in NaY Zeolite

NaY zeolite samples were prepared containing a bulk average of 0.5, 1.0, 2.0, 3.0 and 4.0 benzene molecules per supercage. All experiments were performed at 190±1 K, with temperature regulation achieved by flowing dry N_2 gas through the

temperature control apparatus and over the sample. The eight ($\pi/2$) pulse sequence of Baum et al. [37] was used to create an effective Hamiltonian during the preparation period proportional to the double quantum operator:

$$\mathcal{H} = 1/3 \sum D_{ij}(I_{i+}I_{j+}+I_{i-}I_{j-}),$$

with a $\pi/2$ pulse length of 2.5 μs and a cycle time t_c of 60 μs. The phase of the preparation period was incremented in 32 steps from 0 to 2π in order to generate the phase shift $\Delta\phi$. Each period from 0 to 2π contained two MQ interferogram echoes, and the signal $S(\Delta\phi)$ was averaged over sixteen MQ interferogram echoes ($0 \leq \Delta\phi \leq 16\pi$), as shown in Figure 5.3 for hexamethylbenzene in NaY zeolite. Spectra were approximated by a gaussian least-square fit, as described in chapter three with modifications detailed below, to obtain the apparent size of the spin network as a function of preparation time, $N_{app}(\tau)$. The behavior of $N_{app}(\tau)$ was analyzed for each sample to determine the average spin cluster size as a function of benzene concentration, in order to find possible guest distributions for benzene in NaY zeolite at various loadings.

As was found for hexamethylbenzene, spin clusters formed by the collection of benzene molecules in faujacite supercages do not approximate ideal spin clusters as well as those found on oriented molecules in liquid crystalline mesophases. Benzene molecules are relatively small, allowing them to pass easily from supercage to supercage at room temperature. The molecules are expected to adhere to the cationic (S_{II}) *and* window (W) sites at lower temperatures [63-66, 68], possibly creating strongly coupled spin networks between adjoining supercages. The smaller molecular size when compared to hexamethylbenzene allows it to adhere more closely to the wall

of the supercage, shortening the distance between molecules in adjoining supercages and weakening the spin cluster isolation. Again, the molecules possess no long range orientational order, so the excitation time necessary to approach the statistical limit will vary between the spin clusters. Finally, the number of benzene molecules in a supercage can vary from zero to five [64-66], so samples at some loadings may contain a mixture of molecular cluster sizes which will appear as an *averaged* spin cluster size. The observed size is not the *average* size, for the larger spin clusters will contribute proportionally more signal to the MQ spectrum and raise the *averaged* size above the *average* spin cluster size.

Bulk benzene is not expected to adhere to the exterior of zeolite crystallites as hexamethylbenzene did, so the original two parameter gaussian least-squares fit will be used. The small spin cluster size expected at low loadings, 6 to 12 spins, will invalidate the assumption of Stirling's approximation made in the fitting procedure, and may affect the indicated actual spin cluster size as was seen for low loadings of hexamethylbenzene. Again, this problem can be circumvented by comparing the behavior of $N_{app}(\tau)$ for samples with different loadings, as above. A second consequence of small cluster size is the inclusion of the two quantum peak in the gaussian fitting procedure, due to the small number of transition orders with appreciable intensity. While this may cause some uncertainty to N_{app} in small clusters due to an appreciable number of molecules rotating about their C_6 axis at or near the magic angle with respect to the external field, clusters containing more than one benzene molecule will not be strongly affected by the lack of long range orientational order. This is due to the impossibility of arranging both C_6 axis and the intermolecular vector at or near the magic angle.

Results of MQ-NMR spin counting experiments for NaY zeolite samples

containing bulk concentrations of 0.5 and 1.0 benzene molecules per supercage are reported in Figure 5.6. Note that the behavior of $N_{app}(\tau)$ for the two loadings is not identical, indicating a primarily random distribution of adsorbate molecules between the supercages of the zeolite. The average cluster size indicated for the more lightly loaded sample is about four or five spins, corresponding to unimolecular spin clusters. The average cluster size indicated for the more heavily loaded sample is about eight or nine spins, corresponding to a mixture of unimolecular and bimolecular spin clusters. The small size of the clusters in both cases invalidates Stirling's approximation for all the transition orders, so the reported numbers are probably inaccurate compared to the real average cluster sizes. However, the increase in the observed cluster size upon increase of the guest concentration from a bulk average of 0.5 to 1.0 molecules per supercage indicates an appreciable number of supercages containing two or more benzene molecules at the higher guest concentration.

Results of MQ-NMR spin counting experiments for benzene adsorbed in NaY zeolite at a bulk concentration of 2.0 molecules per supercage are reported in Figure 5.7. Note that $N_{app}(\tau)$ for this sample appears to be composed of three regions: a rapidly rising initial region, a more slowly rising central region, and a nonrising final region as τ increases. The difference between the slopes in the first two regions of $N_{app}(\tau)$, if real, could be due to the difference in couplings between spins in the same benzene molecule and spins on different benzene molecules in the same supercage. The final region of $N_{app}(\tau)$ indicates an average cluster size between 10 and 12 spins, indicating a relatively uniform distribution of guest molecules as bimolecular clusters. Again, the small size of the spin networks make this cluster size uncertain, but the averaged size is somewhat larger than that found for the sample containing an average

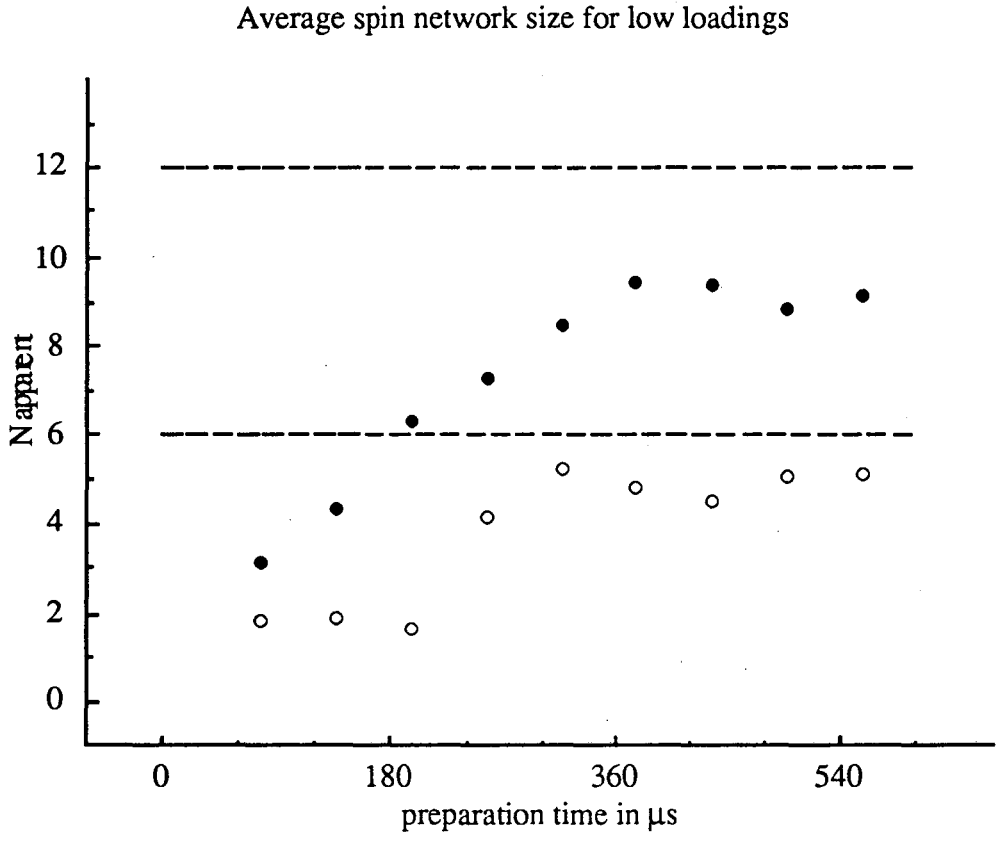

Figure 5.6. Apparent average spin cluster size as a function of preparation time for NaY zeolite samples containing one-half and one benzene molecules per supercage (open and filled circles, respectively).

concentration of one molecule per supercage and is not markedly higher than 12, as would be expected for a purely random mixture. The existence of isolated clusters at this concentration, as evidenced by $N_{app}(\tau)$ becoming relatively constant at long excitation times, indicates that the molecules are adsorbed primarily within the supercages, probably at the S_{II} sites. Appreciable occupancy of the W sites would lead to either a much larger average cluster size or a continuous spin network, depending upon the rate of window occupancy.

Increasing the benzene concentration further should show the effects of molecular competition for the cationic S_{II} adsorption sites, since bulk loadings of more than two benzene molecules per cage will occupy more than half of these sites. Figure 5.8(a) reports the results of MQ-NMR spin counting experiments for a NaY zeolite sample with a bulk concentration of three benzene molecules per supercage. The spin network grows at a constant rate over the interval 300 $\mu s \leq t_p \leq$ 540 μs, and then grows at a slower constant rate from 540 μs to the end of the experimental range. The dotted lines were determined by a linear least-squares fit to the respective regions of the $N_{app}(\tau)$ curve. As in Figure 5.7, the growth rate of the spin network for preparation times $\tau \leq 540$ μs is dominated by the coupling of spins within the same supercage. The growth rate of the spin network after 540 μs is likely due to the coupling of spins in neighboring supercages, since the size of the spin network shows no upper limit.

The difference between the slope of $N_{app}(\tau)$ before and after 540 μs of excitation must be due to the large differences in dipole-dipole couplings between *intra*supercage and *inter*supercage proton pairs, for the geometry of the interacting spin groups is the same. In both cases, six protium nuclei on an adsorbed benzene molecule dipole-dipole couple to six protium nuclei on another benzene molecule, with the only

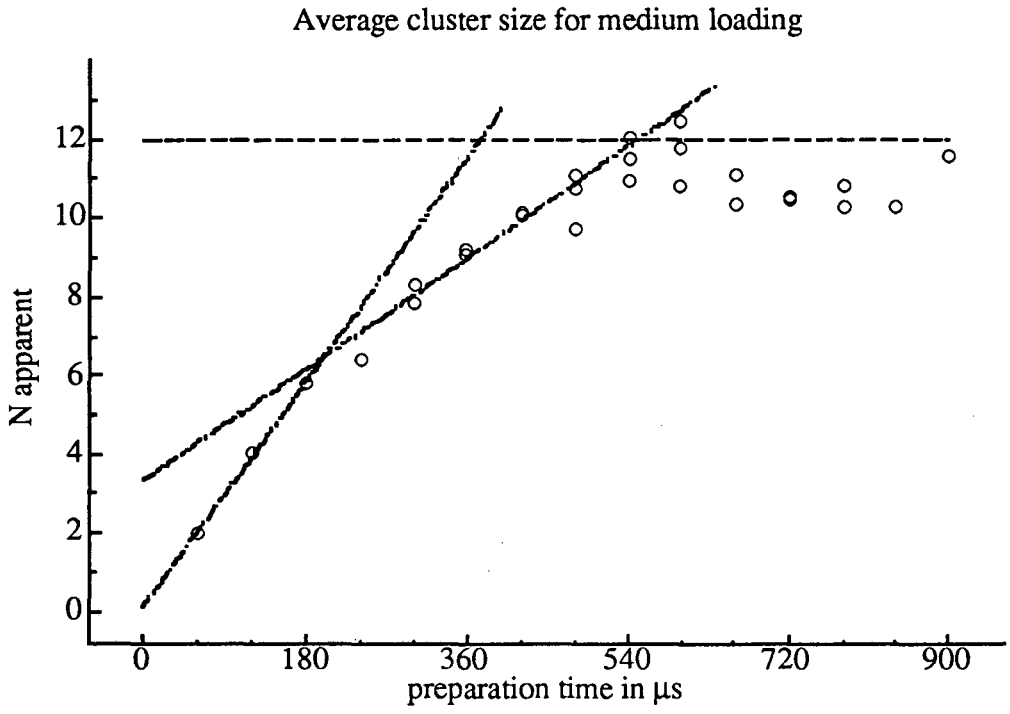

Figure 5.7. Apparent average spin cluster size as a function of preparation time for NaY zeolite containing a bulk average of two benzene molecules per supercage. The dashed line marks the level of 12 spins, while the two other lines were determined by least-squares fits of regions of the experimental data, as described in the text.

difference being that molecules in the same supercage are closer to one another than molecules in adjoining supercages [71]. The contribution from *inter*supercage dipole-dipole couplings to the growth rate of the spin network is found by examining the slope of the $N_{app}(\tau)$ curve after 540 μs of excitation, since the spin network growth at this point is due primarily to *inter*supercage couplings. Evolution of $N_{app}(\tau)$ due to *inter*supercage dipole-dipole couplings can be modeled as a line passing through the origin and having a slope identical to that of the $N_{app}(\tau)$ after 540 μs of excitation. Subtracting this line from the $N_{app}(\tau)$ curve removes the *inter*supercage dipole-dipole contribution to the evolution of the spin network, leaving only the contribution due to the *intra*supercage dipole-dipole couplings. Figure 5.8(b) reports the difference between the data shown in Figure 5.8(a) and a line passing through the origin with a slope identical to that of the least-squares fit to the data for preparation times (τ) greater than or equal to 540 μs. The curve depicted by the data in Figure 5.8(b) therefore represents the evolution of the spin networks decoupled from the effects of molecules in neighboring supercages. The indicated average spin cluster size of 18 spins corresponds to three benzene molecules per occupied supercage, consistent with a uniform distribution of benzene molecules among the zeolite supercages. A random molecular distribution would generate a markedly higher average spin cluster size. Appreciable occupation of the W sites at this relatively high benzene concentration would generate very large spin clusters, as the spins in several supercages would be strongly coupled to one another.

Investigation of the effects of guest competition for adsorption sites was continued by increasing the guest concentration to a average concentration of four benzene molecules per supercage. Figure 5.9(a) reports the results of MQ-NMR spin

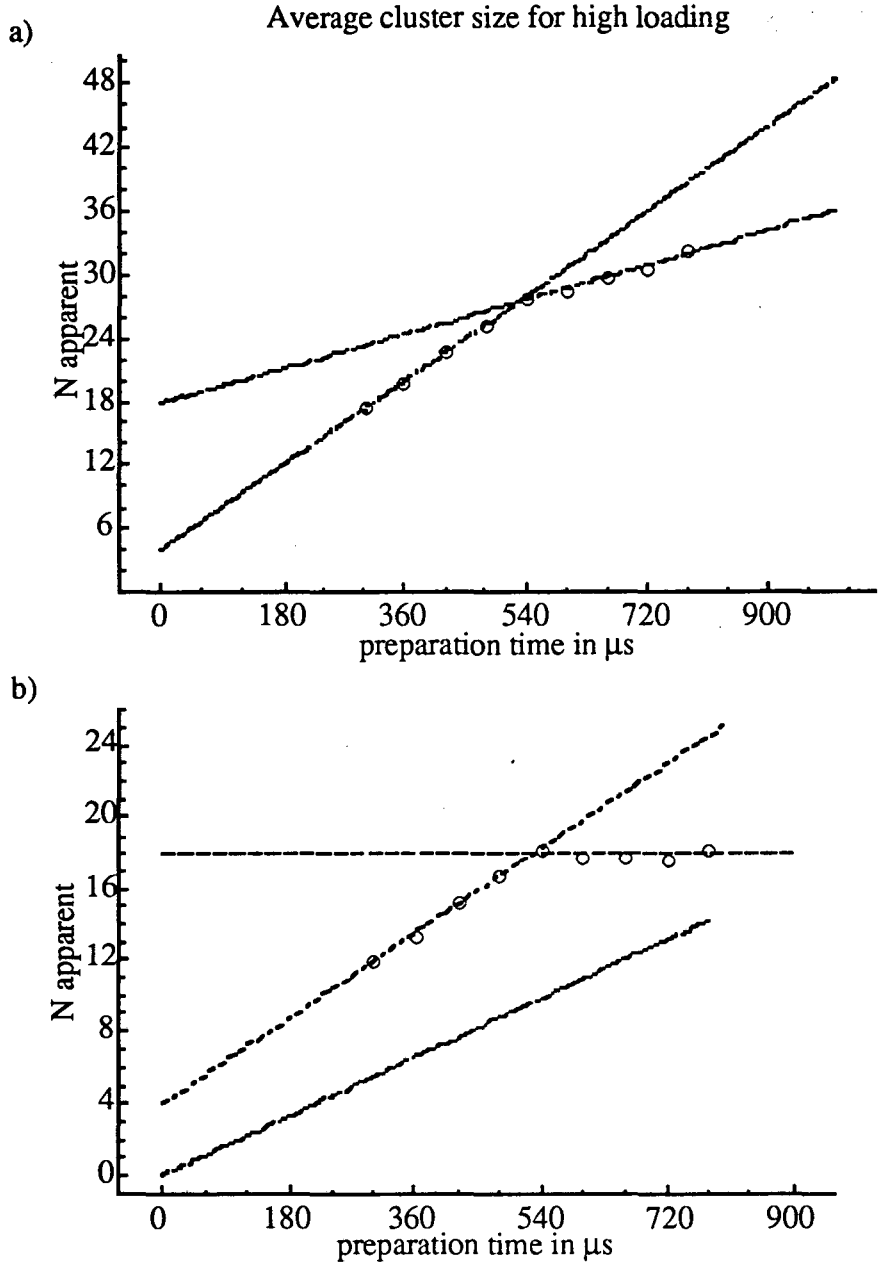

Figure 5.8. a) N apparent as a function of preparation time for NaY zeolite containing a bulk concentration of three benzene molecules per supercage. b) The difference between the data in a) and a line drawn through the origin with a slope determined by a least-squares fit of the data acquired after 500 μs.

counting experiments for a NaY zeolite sample with a bulk concentration of four benzene molecules per supercage. The absence of any limit on $N_{app}(\tau)$ or any obvious decrease in the spin network's growth rate is characteristic of the spin cluster being infinite in size. Such a result occurs when there is little or no difference in the magnitude of dipole-dipole couplings between spins or groups of spins throughout a sample. In the case of benzene molecules adsorbed in NaY zeolite, this would indicate a lack of spatial isolation between supercages.

Inspection of the MQ spectra obtained at long preparation times show the peak intensities to be the sum of two gaussians: one approximately the same width as found for the sample containing three benzene molecules per supercage, the other much wider. This reflects clustered spin networks mixed with a continuous spin network, as was seen above for high bulk loadings of hexamethylbenzene in NaY zeolite. Assuming that the size of the continuous spin network is infinitely larger than that of the clustered spin network, the influence of the continuous spin network can be accounted for by adding the amplitude of this "infinitely" wide gaussian to each of the peak intensities. This is done by adding a constant offset parameter to the gaussian least-squares fitting program, shifting the gaussian curve to account for the continuous spin network's contribution to each spectrum. Figure 5.9(b) depicts $N_{app}(\tau)$ after accounting for the contribution of the continuous spin network to each spectrum. The values of $N_{app}(\tau)$ are essentially the same as in Figure 5.9(a) until $\tau \sim 540$ μs, at which point the diminished slope reflects a lessening of the spin network growth rate. This is characteristic of weakly coupled clusters, as shown above for an average concentration of three benzene molecules per supercage. The $N_{app}(\tau)$ curve derived for the molecular spin clusters within the supercages is not quantitative, for the sample most

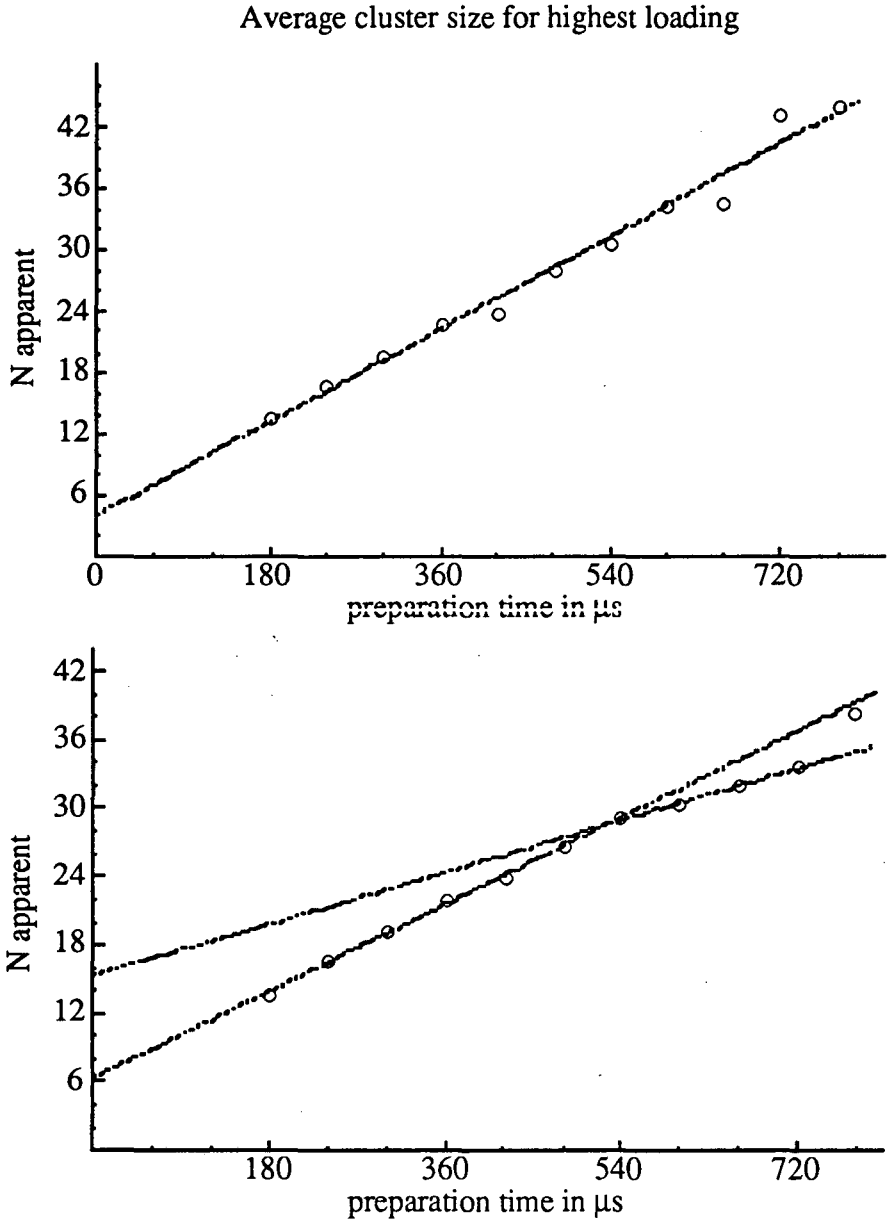

Figure 5.9. a) N apparent as a function of preparation time for NaY zeolite containing benzene at an average concentration of four molecules per supercage.

b) Same as in a), except N apparent was determined by a least-squares gaussian fit with a constant offset parameter, as described in the text.

likely contains a range of spin cluster sizes spanning one, two, three or more supercages, instead of a bimodal distribution of spin clusters spanning either one (isolated) or very many (continuous) supercages as was assumed in the process leading to Figure 5.9(b).

The continuous spin network is most likely the result of a significant number of benzene molecules occupying window sites (W) between two adjacent supercages. Sample loadings above three benzene molecules per cage can trap molecules in these energetically less favorable window sites through prior occupation of all the adjacent cation (S_{II}) sites. The magnitude of the intermolecular dipole-dipole couplings would be approximately the same throughout such a continuous spin network due to molecules in W sites bridging the gaps between adjacent supercages. In contrast to hexamethylbenzene, it is not likely that an appreciable amount of bulk adsorbate is located on the exterior surface of the zeolite crystallite, for the molecular dimensions of benzene are small enough to allow easy access to the zeolite interior [69, 71].

The above results indicate that the distribution of benzene molecules in NaY zeolite is dependent upon the bulk concentration of the aromatic guest. Initially, the introduction of a small amount of benzene into dehydrated NaY zeolite allows the molecules to move randomly throughout the sample, translating along the interior supercage surfaces from site to site. The cationic S_{II} sites appear to be preferred over the W sites, as predicted by Monte Carlo simulation [68]. As the bulk concentration increases above one guest molecule per supercage the distribution appears to become more uniform, with the distribution of benzene molecules between zeolite supercages becoming definitely uniform at a bulk concentration of three molecules per supercage. Increasing the benzene concentration further leads to the occupation of an appreciable number of the less energetically favorable W sites, probably due to competition for the

few remaining S_{II} and crowding of the supercages themselves. In no instance was any evidence of large molecular aggregations at low guest loadings observed, contrary to the results of the above sited neutron diffraction study [62].

The geometry of adsorbate positions within the zeolite supercages can also be inferred from the spin network growth rates measured when weakly coupled clusters are observed. In the case of molecular adsorbates, the growth rate of $N_{app}(\tau)$ is approximately proportional to the product of the intermolecular homonuclear dipole-dipole coupling strength and the number of spins being incorporated into the network [76]. The relative dipolar coupling strengths involved in each of the growth mechanisms can therefore be found by dividing each slope by the number of spins in the respective subnetworks, in this case 6, for a benzene molecule, and 18, for a benzene cluster in a supercage:

$$\frac{|D_1|}{|D_2|} \approx \left(\frac{m_1}{6} \times \frac{18}{m_2}\right) = 4.34 \quad , \tag{5.1}$$

where the D_i's are the respective dipole couplings and the m_i's are the growth rates (slopes), taken from Figure 5.8 for the case of benzene in NaY zeolite. To calculate the distances between spins on different benzene molecules we note that benzene adsorbed in NaY zeolite rotates rapidly about its six-fold axis at temperatures between 125 K and 250 K [65], allowing us to treat the center of each benzene molecule as a group of six protons. The ratio of distances between molecular centers within the same supercage and between those in adjacent supercages can be approximated by taking the cube root of the relative dipolar coupling strength estimated from expression (5.1). This indicates relative benzene-benzene distances of ~ 1:1.6 between benzene molecules adsorbed in the same supercage and benzene molecules adsorbed in adjacent

supercages.

Assuming benzene guests adsorb at S_{II} sites within the zeolite at a bulk concentration of three benzene molecules per supercage, and also assuming an average displacement from the Na^+ ion of about 3Å [65, 67-68], we find the molecular centers to be arranged on the vertices of two sets of tetrahedra, as shown in Figure 5.10. The edges of the smaller tetrahedra represent the distance between molecular centers within the *same* supercage, while the edges of the larger tetrahedra represent the distance between the nearest neighbor molecular centers in *adjacent* supercages. NaY sodalite cages are located within the large tetrahedra, with the hexagonal S_{II} faces about 3Å from the vertices. Since the supercages are ~ 13Å across, this model reflects an outer diameter for the sodalite cage of ~10Å. This is consistent with the symmetry and lattice parameters of the sodalite structure obtained from diffraction experiments [71] after accounting for the finite dimensions of the sodalite cage's constituent atoms. This confirms the assumption that benzene molecules primarily occupy the cationic S_{II} sites in the NaY zeolite supercages at a bulk concentration of three molecules per supercage, for the occupation of different types of sites would generate different homonuclear dipole-dipole coupling ratios from those observed.

It is now possible to postulate a model for the distribution of benzene in a faujacitic zeolite based upon the results reported above. As benzene is added to dehydrated NaY zeolite the guest molecules diffuse freely between the supercages, adsorbing at and hopping between cationic sites (S_{II}) randomly, as predicted by Monte Carlo simulations [68]. The absence of uniform or aggregated benzene distributions at low loadings show a lack of discrimination against multiply occupied supercages and

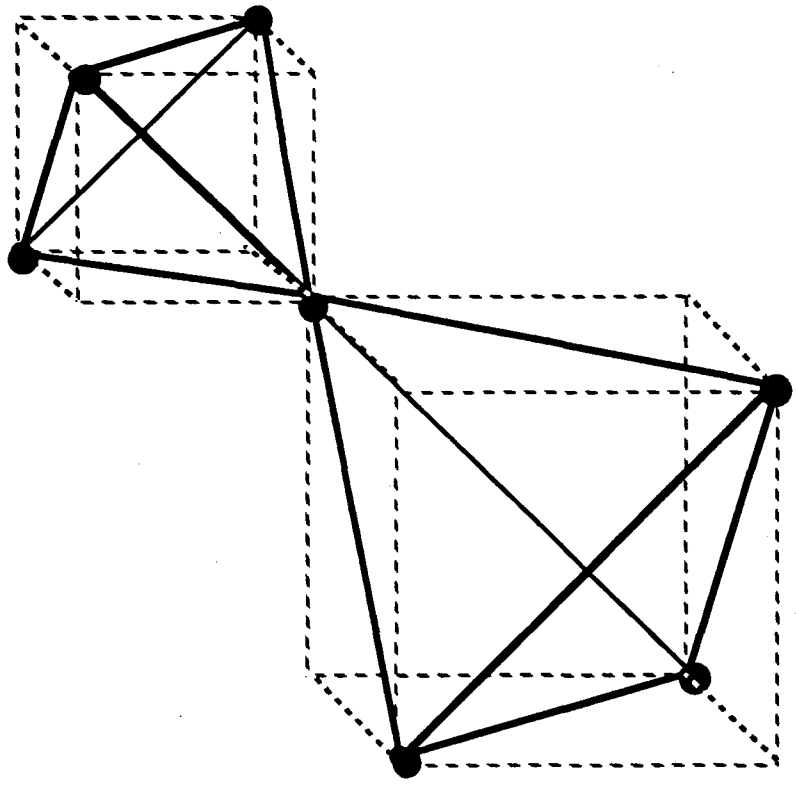

Figure 5.10. Schematic depiction a cationic adsorption site in NaY zeolite and the nearest neighboring sites within the same supercage and in adjacent supercages. The vertices of the small tetrahedron indicate the adsorption sites in the same supercage while the vertices of the large tetrahedron indicate adsorption sites on the same sodalite cage and in adjoining supercages.

also refutes the existence of a preferential molecular cluster size. The uniform molecular clustering of benzene seen at a bulk concentration of three molecules per supercage demonstrates a preference against adsorption of four benzene molecules per supercage. The clear bimodal behavior of the spin network growth rate indicates the existence of only two distances for guest-guest separation, confirming the predominate occupation of S_{II} sites at this concentration. Adsorbing benzene molecules at all four S_{II} sites within a supercage appears to be sufficiently unfavorable for large number of benzene molecules to be directed to window sites (W), as evidenced by the continuous spin network observed in NaY zeolite with a bulk concentration of four molecules per supercage. There are half as many W sites as S_{II} cation sites, since each of the four windows adjoining a supercage is shared with a neighboring supercage [71]. An extrapolation of the linear least-squares fit of the >540 μs region of Figure 5.9(b) indicates that the only supercages without at least one W site occupied are those that have only two or three S_{II} sites occupied by benzene guests. Bulk loadings of more than four benzene molecules per supercage generate an infinite spin network spanning the entire sample and therefore are not suited to investigation by MQ-NMR. It seems evident that additional molecules, up to the maximum sorption capacity of 5.4 molecules per supercage, would probably fill the remaining S_{II} and W sites, as has been previously suggested [63-64, 78].

6

Spin Clusters in the Irreducible Tensor Basis

6.1 Introduction

The chosen operator basis set throughout this work has been the eigenoperator basis of **I** and I_z, with ρ expressed in terms of operators $|i\rangle\langle j|$ such that:

$$[I_z, |i\rangle\langle j|] = n_{ij} |i\rangle\langle j| , \tag{6.1}$$

where n_{ij} is the order of ρ_{ij}. An alternate set of basis operators are the irreducible representations of the full rotation group SO(3), T_{lm}, otherwise known as irreducible tensor operators [17, 80]. The relationship between the eigenoperator basis and the irreducible tensor basis can be seen by comparing equation (6.1) with the property:

$$[I_z, T_{lm}] = m T_{lm} , \tag{6.2}$$

where l and m are the angular momentum and magnetic quantum numbers. While the eigenoperator basis was convenient for depicting elements of ρ coupled by a single dipole-dipole coupling, T_{lm}'s model the evolution of ρ as the evolution of groups of spins. The results of MQ-NMR spin counting experiments on both oriented n-alkanes and benzene molecules adsorbed on NaY zeolite suggest that spin clusters do evolve in terms of groups of spins, spanning either a region of a molecule or whole molecules in a molecular cluster.

A brief review of the expression of ρ in terms of irreducible tensor operators

will be followed by description of the previous experiments in terms of tensor operators. A more comprehensive treatment of tensor operators can be found in texts by Silver [80] and others [81-83]. In addition, an experiment to measure both the m and l quantum numbers of multi-spin coherences in adamantane will be described.

6.2 Spin Clusters and Irreducible Tensor Operators

The density matrix for an isolated spin cluster may be expressed in terms of irreducible tensor operators T_{lm}[17]:

$$\rho = \sum_{l,m} a_{lm} T_{lm} , \tag{6.3}$$

where a_{lm} is a coefficient dependent upon both the l and m quantum numbers, l is limited by the number of coupled spins and the additional quantum numbers for the complete characterization are not written explicitly. The density matrix for two perfectly isolated spin clusters may be expanded into two sets of T_{lm}:

$$\rho = \sum_{l,m} a_{lm} T_{lm} + \sum_{l',m} b_{l'm} T_{l'm}, \tag{6.4}$$

where the ranges of l and l' are determined by the number of coupled spins in each cluster. Expansion of ρ in terms of one set of operators:

$$\rho = \sum_{L=0}^{L=l+l'} \sum_{m} a_{Lm} T_{Lm} , \tag{6.5}$$

while proper, is unnecessary, for the coefficients of all basis operators in equation (6.5)

not contained in equation (6.4) will be zero due to the isolation of the two spin clusters. The case of two isolated spin clusters may easily be generalized to an arbitrary number of isolated spin clusters, with the range of l for each determined by the number of spins in each cluster. A physical example of the above would be the treatment of 4-pentyl-4'-cyanobiphenyl molecules in the nematic mesophase as spin clusters of 19 spins with ρ containing $2^{2(19)}$ elements, instead of as a sample containing 10^{20} spins with ρ containing an effectively infinite number of elements.

The case of weakly coupled spin clusters is more complex. Generally, ρ for two weakly coupled spin clusters may still be expressed as:

$$\rho = \sum_{L=0}^{L=l+l'} \sum_{m} a_{Lm} T_{Lm} ,$$

where l and l' are determined by the number of spins in each cluster. Alternately, expression (6.4) may be expanded to include products of the tensors spanning the two clusters [16]:

$$\rho = \sum_{l,m} a_{lm} T_{lm} + \sum_{l',m} b_{l'm} T_{l'm} + \sum_{l,m,l',m'} c_{lml'm'} \left(T_{lm} \otimes T_{l'm'} \right) , \qquad (6.6)$$

where the coupling strengths and other properties are condensed into the coefficients a_{lm}, $b_{l'm'}$ and $c_{lml'm'}$. The difference between expressions (6.5) and (6.6) is that the latter separates the weak coupling between clusters from the relatively strong coupling within the clusters. The weakly coupled clusters may be either on separate molecules or in different regions of the same molecule.

6.2.1 Revisiting Benzene Adsorbed in NaY Zeolite

For the case of benzene molecules adsorbed in NaY zeolite at a bulk concentration of three molecules per supercage, there are three broad classes of dipole

couplings between protium nuclei. There are couplings between nuclei bonded to the same benzene molecule, couplings between nuclei bonded to separate molecules in the same supercage, and couplings between nuclei bonded to molecules in adjoining supercages. The effects of the first class of couplings are strongly dependent upon the orientation of the individual molecules with respect to the external magnetic field, due to the θ dependence of the individual D_{ij}'s. The effects of the latter two classes of couplings will be less variable, for the combination of a tetrahedral arrangement of cationic adsorption sites within and between the supercages and a high level of occupancy of these sites will provide a similar range of D_{ij}'s over many of the possible orientations of the zeolite matrix with respect to the external field. Modeling the system as weakly coupled spin clusters between supercages, expression (6.6) becomes:

$$\rho = \sum_{l,m}^{l=9} a_{lm}T_{lm} + \sum_{l',m}^{l'=9} b_{l'm}T_{l'm} + \sum_{l,m,l',m'}^{l=9,l'=9} c_{lml'm'}\left(T_{lm}\otimes T_{l'm'}\right) , \qquad (6.7)$$

for two neighboring supercages. Of course, ρ for a real system would involve the interaction of many weakly coupled clusters, as schematically depicted in Figure 6.1.

The density matrix of an isolated spin cluster approaches the statistical limit when:

$$\rho = \sum_{m=-l}^{m=l} c_m T^l{}_m , \qquad (6.8)$$

where $T^l{}_m$'s are the tensor operators for fixed l corresponding the size of the spin

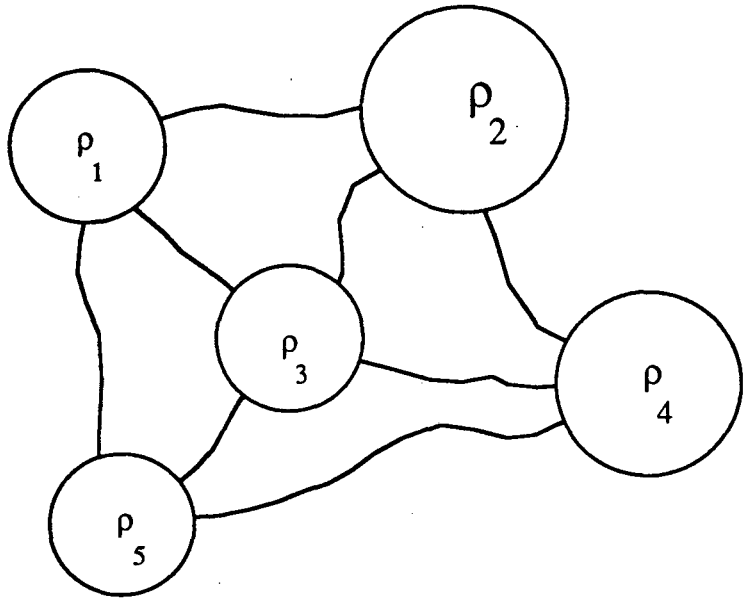

Figure 6.1. Schematic depiction of the interaction of many weakly coupled clusters, each described by a density operator ρ_i. The density operator describing the set of clusters is found to be:

$$\rho = \rho_1 \otimes \rho_2 \otimes \rho_3 \otimes \rho_4 \otimes \rho_5$$

cluster. The segregation of couplings in equation (6.7), with the stronger D_{ij}'s condensed into the a_{lm} and b_{lm} terms indicates that the spin clusters within each supercage will reach the statistical limit before the entire sample does (i.e., a_{lm} --> $c_m\partial(l\text{-}l_{max})$ and $b_{l'm}$ --> $c_m'\partial(l'\text{-}l'_{max})$ before $c_{lml'm'}$ --> $c_{m,m'}\partial(L\text{-}L_{max})$). This type of behavior can be seen in $N_{app}(\tau)$ for benzene adsorbed in NaY zeolite at a concentration of three molecules per supercage, as reported in Figure 5.8(a).

6.2.2 Revisiting n-Hexane Oriented in a Nematic Liquid Crystal

The case of oriented n-hexane is somewhat more complex than that described above for benzene, for there is no obvious separation of the spins into weakly coupled groups. The couplings between spin groups are either generally strong for nuclei bonded to the same molecule, or averaged to zero for nuclei bonded to different molecules. Yet the behavior of $N_{app}(\tau)$ for oriented n-hexane reported in Figure 4.13(a) clearly suggests the existence of weakly coupled spin clusters on the same molecule.

The reason for this behavior can be found in comparing the effects of the dipole couplings between geminal spins upon the evolution of ρ. Initially, ρ can be expanded in terms of 14 spins one half:

$$\rho = \sum_{i=1}^{14} \sum_{m} T_{\frac{1}{2},m}(i) \qquad (6.9)$$

where i denotes the ith spin. After infinite excitation (i.e., long τ), ρ can be expressed as in equation (6.8). The behavior between the two extremes can be modeled as a process of coupling progressively larger and larger T_{lm}'s. For example, immediately

after the beginning of the preparation period the evolution of ρ is dominated by the strongest spin-spin couplings, the dipole couplings between geminal spins. The spins bonded to methylene carbons will interact the fastest:

$$\rho = \sum_m T_{\frac{1}{2},m} \otimes T_{\frac{1}{2},m} \rightarrow \sum_m T_{1,m} \quad , \tag{6.10}$$

while the spins bonded to the methyl carbons will interact more slowly, due to weaker geminal couplings. The continuation of this process will consist of the couplings between spin groups on different methylene carbons and the coupling of individual spins on the methyl carbons to the next nearest methylene spins:

$$\rho = \sum_m T_{1,m} \otimes T_{1,m} \rightarrow \sum_m T_{2,m} \quad , \tag{6.11a}$$

$$\rho = \sum_m T_{\frac{1}{2},m} \otimes T_{1,m} \rightarrow \sum_m T_{\frac{3}{2},m} \quad , \tag{6.11b}$$

with the former process proceeding more quickly due to the larger number of couplings involved. Eventually, spins over the entire methylene 'core' will correlate to one another, with the methyl spins still requiring more time to correlate with the rest of the spin network, as depicted in Figure 6.2.

6.3 Use of SO(3) to Measure l and m Quantum Numbers of Spin Coherence

The expansion of ρ for a cluster of strongly coupled spins in terms of T_{lm}'s implies the possibility of directly measuring both the m and l quantum numbers.

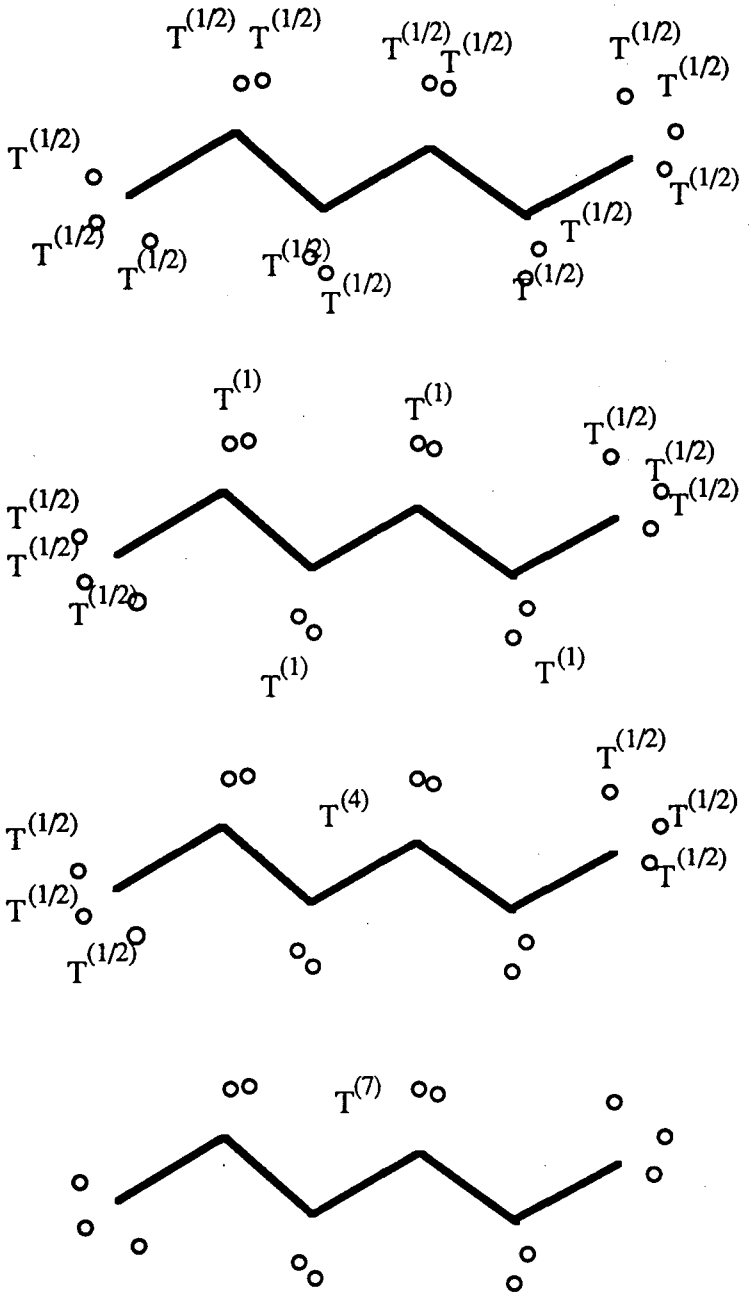

Figure 6.2. Tensorial picture of spin correlation in oriented n-hexane. ρ is spanned by product space of the tensor operators T^l_m, starting with 14 $T^{(1/2)}$ and ending with $T^{(7)}$.

Measurement of both quantum numbers requires the rotation of the spin system by at least two axis. Rotations of angle ϕ about the z axis have been used throughout this work to measure the m quantum number, as can be seen from equation (6.2). To measure l, rotations of angle θ about a second axis are required [80-83].

Experiments were performed upon solid adamantane at room temperature. Rotation about both axis was performed by modification of the all order time reversed sequence introduced in chapter three. A rf pulse parralel to the y axis and of variable duration was added to the evolution period of the sequence, immediately preceding the z rotation (phase shift), as depicted in Figure 6.3. Experimental interferograms were collected by advancing $\Delta\phi$ in 32 steps from 0 to 2π, and then advancing $\Delta\theta$ from 0 to 2π between interferograms. The preparation time remained constant at 386.4 μs, with the signal stored as a two dimensional matrix $S(\Delta\theta,\Delta\phi)$.

Fourier transformation of the two dimensional data set generates a two dimensional spectrum exhibiting resonance peaks in both dimensions, such as the spectrum reported in Figure 6.4, indicating dependence upon both the l and m quantum numbers. The dependence of the signal on the rotation angle θ can be found by noting that the effects of the rotation are governed by the Wigner rotation matrices:

$$S_m(\theta) = \sum_{l,m,m'} a_{lm}a_{lm'}D_{lmm'}(\theta) \ , \qquad (6.12)$$

where S_m is the standard MQ signal projected onto the $\Delta\theta = 0$ axis. This may be simplified by noting that the phase relationship between two elements a_{lm} is nonexistent unless they correspond to the same transition, therefore restricting the sum to $\pm m$:

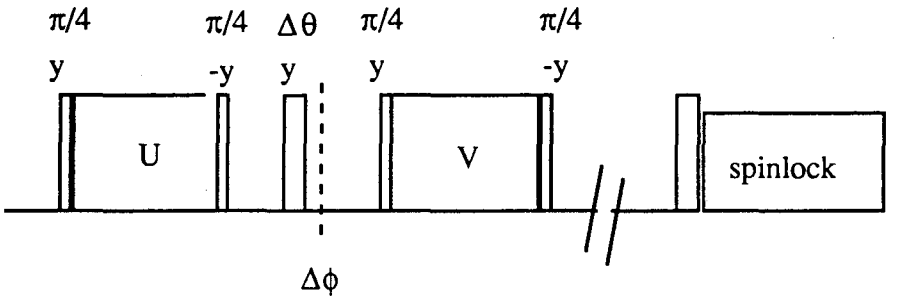

Figure 6.3 Schematic diagram of the pulse sequence used to measure both l and m quantum numbers. Rotation by a variable angle θ is caused by a y pulse during the evolution period, and rotation by a variable angle φ is caused by shifting the rf phase during the evolution period, depicted by the dotted line. Other than the additional y pulse, the sequence is identical to the one diagramed in Figures 3.5 and 3.6.

$$S_m(\theta) = \sum_{l,m} \left(a_{lm}a_{lm}D_{lmm}(\theta) + a_{lm}a_{l,-m}D_{lm,-m}(\theta)\right) , \qquad (6.13)$$

Since ρ is Hermitian,

$$S_m(\theta) = \sum_{l,m} \left((R^2+I^2)\, d_{lmm}(\theta) + d_{lm,-m}(\theta)\left[(R^2-I^2)\cos(2m) + 2RI\sin(2m)\right]\right) , \qquad (6.14)$$

where the complex coefficients have been expanded as $a_{lm}=R+iI$ and d_l represents the Wigner rotation matrices for rotations about the y axis. The matrix elements can be expressed as a Fourier series,

$$d_{lmm}(\theta) = \sum_k b_{lmk}\cos(k\theta) , \qquad (6.15)$$

with the two dimensional intensities becoming:

$$I_{mk} = \sum_{mk} b_{lmk}\left\{(R^2+I^2) + (-1)^{m+1}\left(1-\delta(0-m)\right)\left[(R^2-I^2)\cos(2m) + 2RI\sin(2m)\right]\right\} , \qquad (6.16)$$

Therefore, fitting the above expression to the measured spectrum allows determination of the real and imaginary part of the coefficients, a_{lm}. This was done for the spectrum reported in Figure 6.4, with results reported in Figure 6.5. The results indicate that there is a mixture of apparent cluster sizes in adamantane for τ=386.4 μs. This is expected, for solid adamantane contains an effectively infinite spin network, so no cluster limit will be observed.

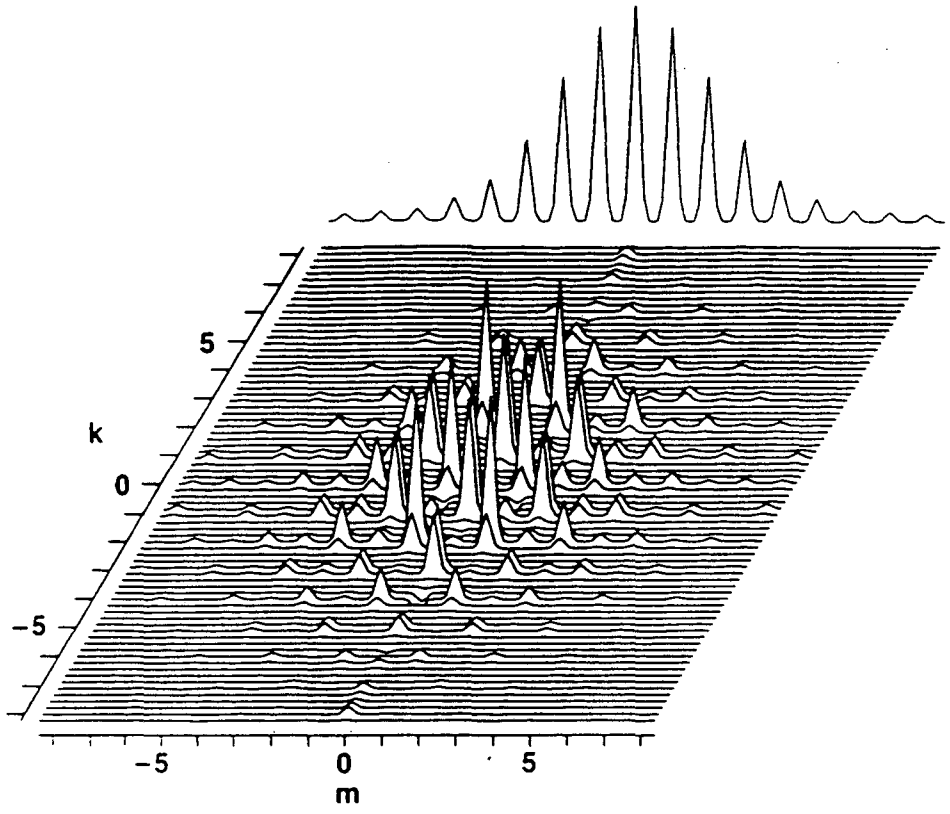

Figure 6.4. Two dimensional spectra for adamantane after 386.4 μs of excitation. The x axis shows the signal's dependence upon the m quantum number, and the y axis shows the signals dependence upon the Fourier coefficients k of the l quantum number. The projection to k = constant axis is the standard MQ spectrum.

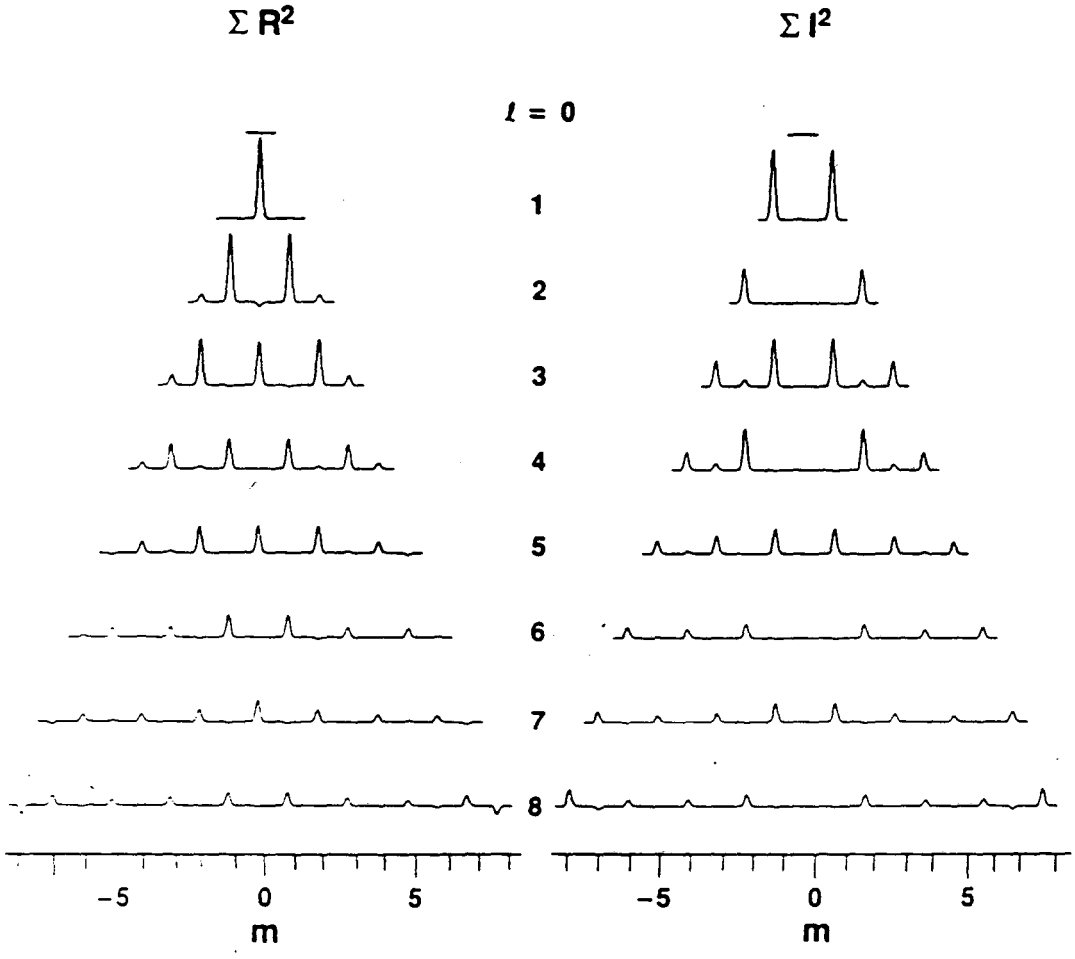

Figure 6.5. Real and imaginary parts of the complex coefficients a_{lm}. The choice of phases in the pulse sequence determined the relative phasing of the coefficients between the real and complex parts.

References

1. S. Yatsiv, *Phys. Rev.*, **113**, 1522 (1952).
2. J. Jeener, *Ampére International Summer School*, Basko Polje, Yugoslavia (1971).
3. W. P. Aue, E. Bartholdi and R. R. Ernst, *J. Chem. Phys.*, **64**, 2229 (1976).
4. R. Freeman, *Proc. R. Soc. Lond.*, **A 373**, 149 (1980).
5. A. Bax, *Two Dimensional NMR*, Delft University Press, 1982.
6. R. R. Ernst, G. Bodenhausen and A. Wokaun, *Principles of Nuclear Magnetic Resonance in One and Two Dimensions*, Oxford University Press (1987).
7. F. Bloch, W. W. Hansen and M. Packard, *Phys. Rev.* **69**, 127 (1946).
8. F. Bloch, *Phys. Rev.* **70**, 460 (1946).
9. F. Bloch, W. W. Hansen and M. Packard, *Phys. Rev.* **70**, 474 (1946).
10. E. M. Purcell, H. C. Torrey and R. V. Pound, *Phys. Rev.* **69**, 37 (1946).
11. E. M. Purcell, *Phys. Rev.* **69**, 681 (1946).
12. T. C. Farrar and E. D. Becker, *Pulse and Fourier Transform NMR*, Academic Press, New York (1971).
13. I. J. Lowe and R. E. Norberg, *Phys. Rev.* **107**, 46 (1957).
14. N.F. Ramsey, *Phys. Rev.* **78**, 699 (1950).
15. P. Bucci, G. Ceccarelli, and C.A. Veracini, *J. Chem. Phys.* **50**, 1510 (1969).
16. U. Fano, *Rev. Mod. Phys.* **29**, 74 (1957).
17. K. Blum, *Density Matrix Theory and Applications*, Plenum Press, New York (1981).
18. A. Abragam, *Principles of Nuclear Magnetism*, Oxford University Press (1961).
19. W.A. Anderson, *Phys. Rev.* **102**, 151 (1956).
20. G.E. Pake, *J. Chem. Phys.* **16**, 327 (1948).

21. W.S. Warren, D.P. Weitekamp and A Pines, *J. Chem. Phys.* **73**, 2084 (1980).

22. U. Haeberlen and J. S. Waugh, *Phys. Rev.* **175**, 453 (1968).

23. H. Hatanaka, T. Terao, and T. Hashi, *J. Phys. Soc. Japan* **39**, 835 (1975).

24. H. Hatanaka and T. Hashi, *J. Phys. Soc. Japan* **39**, 1139 (1975).

25. H. Hatanaka, T. Ozawa, and T. Hashi, *J. Phys. Soc. Japan* **42**, 2069 (1977).

26. H. Hatanaka and T. Hashi, *Phys. Lett.* **67A**, 183 (1978).

27. R. M. Wilcox, *J. Math. Phys.* **8**, 962 (1967).

28. U. Haeberlen, *High Resolution NMR in Solids, Adv. Magn. Reson.* , Suppl. 1 (1976)

29. E. L. Hahn, *Phys. Rev.* **80**, 580 (1950).

30. W. K. Rhim, A. Pines and J. S. Waugh, *Phys. Rev. Lett.* **25**, 218 (1970).

31. W. K. Rhim, A. Pines and J. S. Waugh, *Phys. Rev.* **B3**, 684 (1971).

32. D. E. Wemmer, *Some Double Resonance and Multiple-Quantum Studies in Solids*, Ph.D. dissertation, University of California at Berkeley (1978).

33. G. Drobney, A. Pines, S. Sinton, D. Weitekamp, and D. Wemmer, *Faraday Div. Chem. Soc. Symp.* **13**, 49 (1979).

34. S. Vega, T.W. Shattuck, and A. Pines, *Phys. Rev. Lett.* **37**, 43 (1976).

35. S. Vega, T.W. Shattuck, and A. Pines, *J. Chem. Phys.* **66**, 5624 (1977).

36. A. Pines, S. Vega, and M. Mehring, *Phys. Rev. B* **18**, 122 (1978).

37. J. Baum, M. Munowitz, A. N. Garroway and A. Pines, *J. Chem. Phys.* **83**, 2015 (1985).

38. J. B. Murdoch, W. S. Warren, D. P. Weitekamp and A. Pines, *J. Magn. Reson.* **60**, 205 (1984).

39. R. Bradford, C. Clay, and E. Strick, *Phys. Rev.* **84**, 157 (1951).

40. Y.-S. Yen and A. Pines, *J. Chem. Phys.* **78**, 3579 (1983).

41. A. Wokaun and R.R. Ernst, *Chem. Phys. Lett.* **52**, 407 (1977).

42. A. Pines, D. Wemmer, J. Tang, and S. Sinton, *Bull. of Amer. Phys. Soc.* **23**, 21 (1978)

43. D. Suter, S. B. Liu, J. Baum and A Pines, *Chem. Phys.* **114**, 103 (1987).

44. D.N. Shykind, G.C. Chingas, A.J. Shaka and A Pines, *Rev. Sci. Instrum.* **61**, 1474 (1990).

45. A.J. Shaka, D.N. Shykind, G.C. Chingas and A. Pines, *J. Magn. Reson.* **80**, 96 (1988).

46. U. Haubenreisser and B. Schnabel, *J. Magn. Reson. 35,* 175 (1979)

47. J. Baum, *NMR Studies of Selective Population Inversion and Spin Clustering*, Ph.D. dissertation, University of California at Berkeley (1986)

48. P. G. De Gennes, *The Physics of Liquid Crystals*, Clarendon Press, Oxford (1974).

49. E. Priestly (editor), *Introduction to Liquid Crystals*, Plenum Press (1975).

50. Chandrasekhar, *Liquid Crystals*, Cambridge University Press (1977).

51. P. J. Flory, *Statistical Mechanics of Chain Molecules*, Wiley (1969).

52. J. W. Emsley and G. R. Luckhurst, *Mol. Phys.* **41**, 19 (1980).

53. S. Diele et al, *Mol. Cryst. Liq. Cryst.* **16**, 105 (1972).

54. G. Gray, *Molecular Structure and Properties of Liquid Crystals*, Academic Press, London (1962).

55. A. J. Leadbetter, J. L. A. Durrant and M. Rugman, *Mol. Cryst. Liq. Cryst.* **34**, 231 (1977).

56. T. J. McMaster, H. Carr, M. J. Miles, P. Cairns and V. J. Morris, *Liquid Crystals*, **9**(1), 11 (1991).

57. M. Gochin, A. Pines, M. E. Rosen, S. P. Rucker and C. Schmidt, *Mol. Phys.*

69, 671 (1990).

58. S.P. Rucker, M.E. Rosen, C. Schmidt, P. Neidig and A. Pines, to be published.
59. S.P. Rucker, *Two Dimensional Nuclear Magnetic Resonance Studies of Molecular Structure in Liquids and Liquid Crystals*, Ph.D. Thesis, University of California at Berkeley (1991).
60. M. Lee and W. I. Goldburg, *Phys. Rev.* **A140**, 1261 (1965).
61. A. J. Renouprez, H. Jobic and R. C. Oberthür. *Zeolites* **5**, 222 (1985).
62. A. N. Fitch, H. Jobic and A. J. Renouprez. *J. Chem Soc.*, chem. commun., 284 (1985).
63. A. de Mallmann and D. Barthomeuf, *New Developments in Zeolite Science and Technology*, from the 7th International Zeolite Conference, Tokyo (1986).
64. H. Lechert and K.-P. Wittern, *Ber Bunsenges. Phys. Chem.* **82**, 1054 (1978).
65. B. Zibrowius, J. Caro and H. Pfeifer, *J. Chem. Soc., Faraday Trans. I*, **84**(7), 2347 (1988).
66. A. Germanus, J. Kärger, H. Pfeifer, N.N. Samulevic and S.P. Zdanov, *Zeolites* **5**, 91 (1985).
67. P.J. O'Malley, *Chem Phys. Lett.*, **166**(4), 340 (1990).
68. P. Demontis, S. Yashonath and M.C. Klein, *J. Phys. Chem* **93**, 5016 (1989).
69. R.W.G. Wyckoff, *Crystal Structures*, Interscience, New York (1948).
70. R.W. Hoffmann and G.W. Brindley, *Geochim. Cosmochim. Acta* **20**, 15 (1960).
71. W. Meier and D.H. Olson, *Atlas of Zeolite Structure Types*, Butterworths (1987).
72. D. W. Breck, *Zeolite Molecular Sieves*, Krieger: Malabar, Fl (1984).
73. R.M. Barrar and D.M. MacLeod, *Trans. Faraday Soc.* **51**, 1290 (1955).
74. R.M. Barrar, *Zeolites and Clay Minerals as Sorbents and Molecular Sieves*, Academic Press, London (1978).

75. B. F. Chmelka, J. G. Pearson, S. B. Liu, R. Ryoo, L. C. de Menorval and A. Pines, *J. Phys. Chem.* **95**, 303 (1991).

76. M. Munowitz and A. Pines, *Principles and Applications of Multiple-Quantum NMR*, Wiley (1987).

77. W.-D. Hoffmann, *Z. Phys. Chem. (Leipzig)* **257**, 315 (1976).

78. A. Loeffler, C. Penker and D. Kunath, *Adsorption of Hydrocarbons-II*, workshop Eberswalde (1982), supplement.

79. H. Lechert, K.-P. Wittern and W. Schweitzer. *Acta Physica et Chemica* **24**, 201 (1978).

80. B. Silver, *Irreducible Tensor Methods*, Academic Press, New York (1964).

81. A. Edmonds, *Angular Momentum and Quantum Mechanics*, Princeton (1968).

82. M. Rose, *Elementary Theory of Angular Momentum*, Academic Press, New York (1957).

83. M. Tinkham, *Group Theory and Quantum Mechanics*, Academic Press, New York (1964).

Appendix

This section of the dissertation contains designs for some of the home built components used in the multiple-quantum cluster counting experiments described in the main text. The components described here are: the fast, stable quadrature phase generator, the variable temperature probe, the temperature control apparatus, the high voltage power supply to the Henry amplifier, and the modifications to the Henry amplifier.

The fast, stable quadrature phase generator is described in detail in reference [44], and the diagram in Figure A.1 was lifted directly out of this publication. The design is for an adjustable phase modulator which relies entirely upon precision analog techniques to achieve high stability, fast switching, and very fine adjustments. Personal experience has shown that this design is stable for periods of one to two weeks with less than 0.01 degrees drift in phase or 0.05 dB drift in power, as determined by the 'Haubenreisser' sequence [46] described in the text.

Components for the variable temperature probe are diagramed in Figures A.2-A.6, with the probe assembly shown in Figure A.7. The aluminum rf shield and brass base are of a standard design in the Pines' lab. Macore and non-magnetic stainless steel were chosen for the components which experience the strong temperature gradients due to their nearly identical coefficients of thermal expansion. The coil was a six turn solenoid made of flattened copper wire, and was located in the void surrounded by the stainless steel dewar and the macore base. The rest of the tuned circuit was located between the brass and macore bases, with electrical connection between the coil and the rest of the circuit made by stainless steel jacketed coax. SS coax was used to improve thermal isolation of the VT cell, but blowing warm N_2 gas over the components in the lower section was still required. Cold N_2 gas for the VT cell was obtained by passing

house N_2 gas through a heat exchange coil in a tank of liquid N_2.

The temperature control apparatus was centered upon an Omega model 4201F temperature controller with a 100 Ω resistance thermometer. The variable output of 4-20 mA is amplified by the circuit shown in Figure A.8 and is dissipated in a heater placed in the cold N_2 gas stream just before the probe transfer line. Temperature regulation of ±0.1 K to temperatures 140 K below room temperature was readily achievable by use of this device in conjunction with careful variation of the cold gas flow rate.

The high voltage power supply to the Henry tuned amplifier was replaced by one designed and built in the LBL electronics shop. The circuit diagram for the power supply is shown in Figure A.9. The design is centered around the use of an EIMAC 4-1000 power tube to regulate the high voltage power supplied to the rf amplifier.

The modifications to the Henry 1002 rf amplifier are shown in figure A.10. The variable "plate" capacitor consists of a pivoting grounded plate beneath a high voltage plate connected to the tube output via 200 pf of capacitance. The output was coupled to the high voltage plate by placing a 3/8" copper strip above the HV plate and connecting this strip to the HV output. Deforming the strip allowed for course adjustment of the amplifier match, with fine adjustment achieved by use of the variable capacitors.

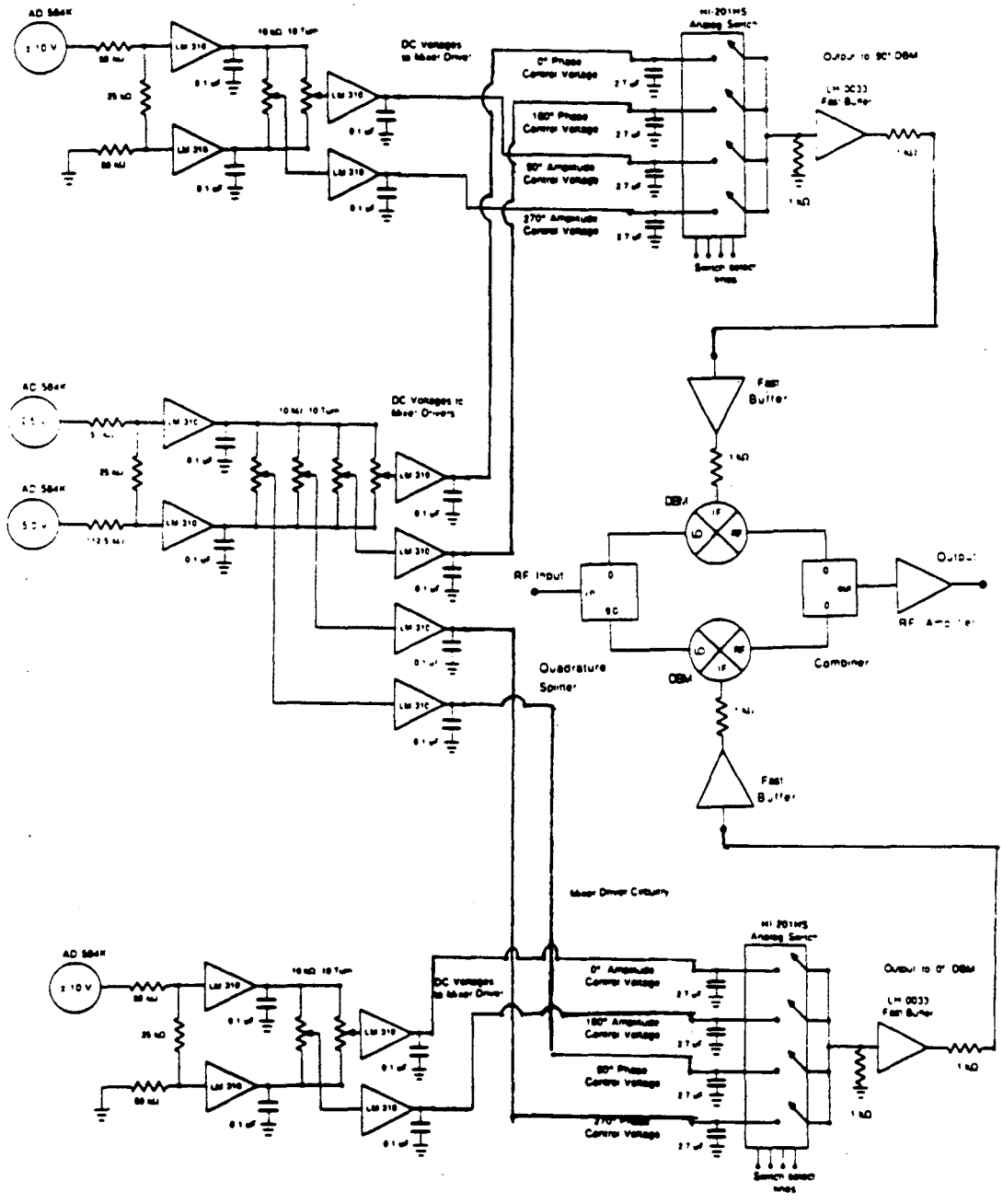

Figure A.1. Circuit diagram for the fast, stable quadrature generator [44].

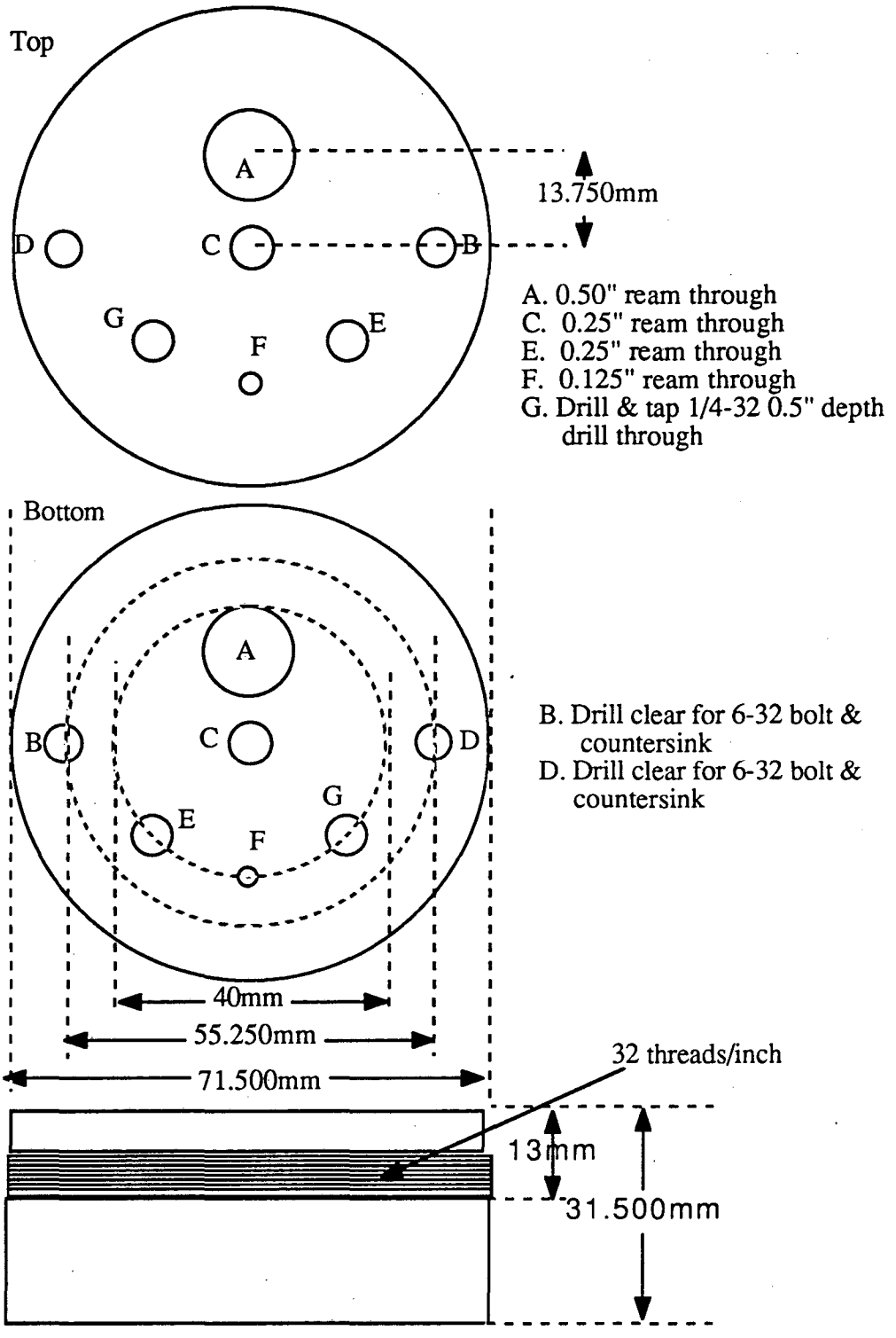

Figure A.2. Diagram of the brass base used in the VT probe. "A" is for the transfer line, "B"&"D" are for brass rods, "C" is for the glass warm gas tube, "E" is for the rf input, "F" is for the platinum resistance thermometer and "G" is for a polyflon resistor.

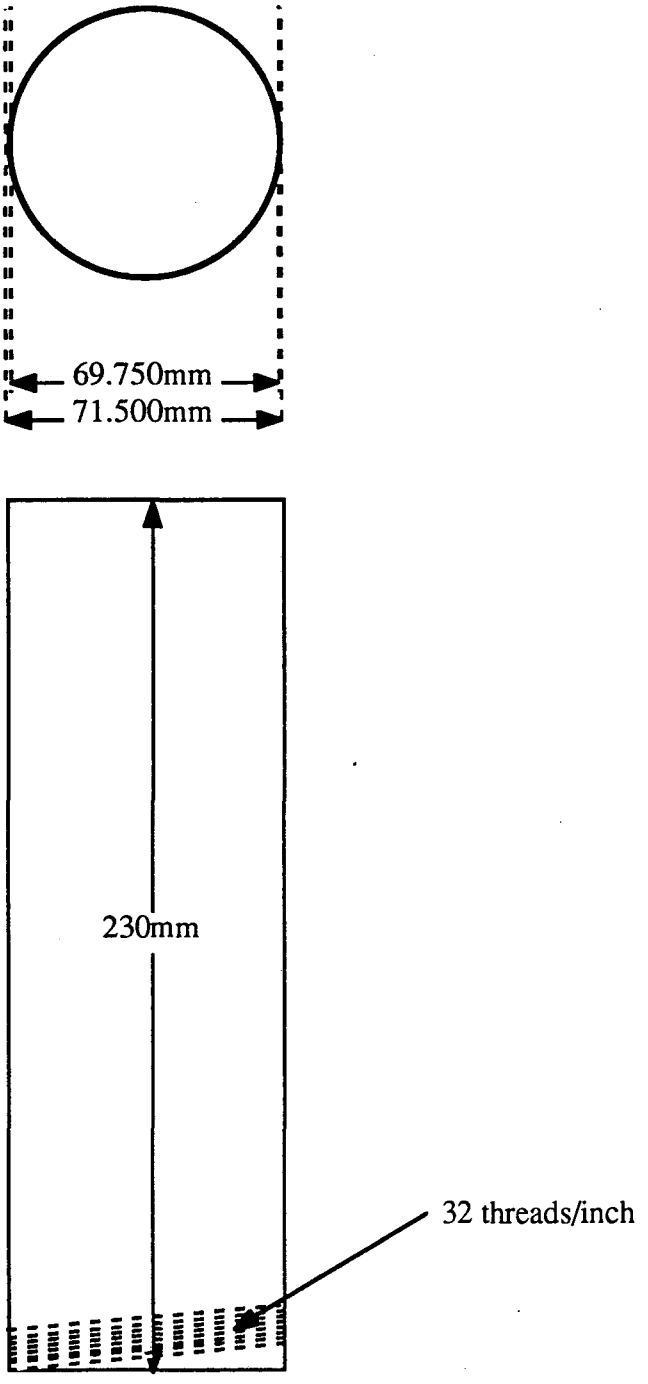

Figure A.3. Diagram of the aluminum rf shield used in the VT probe.

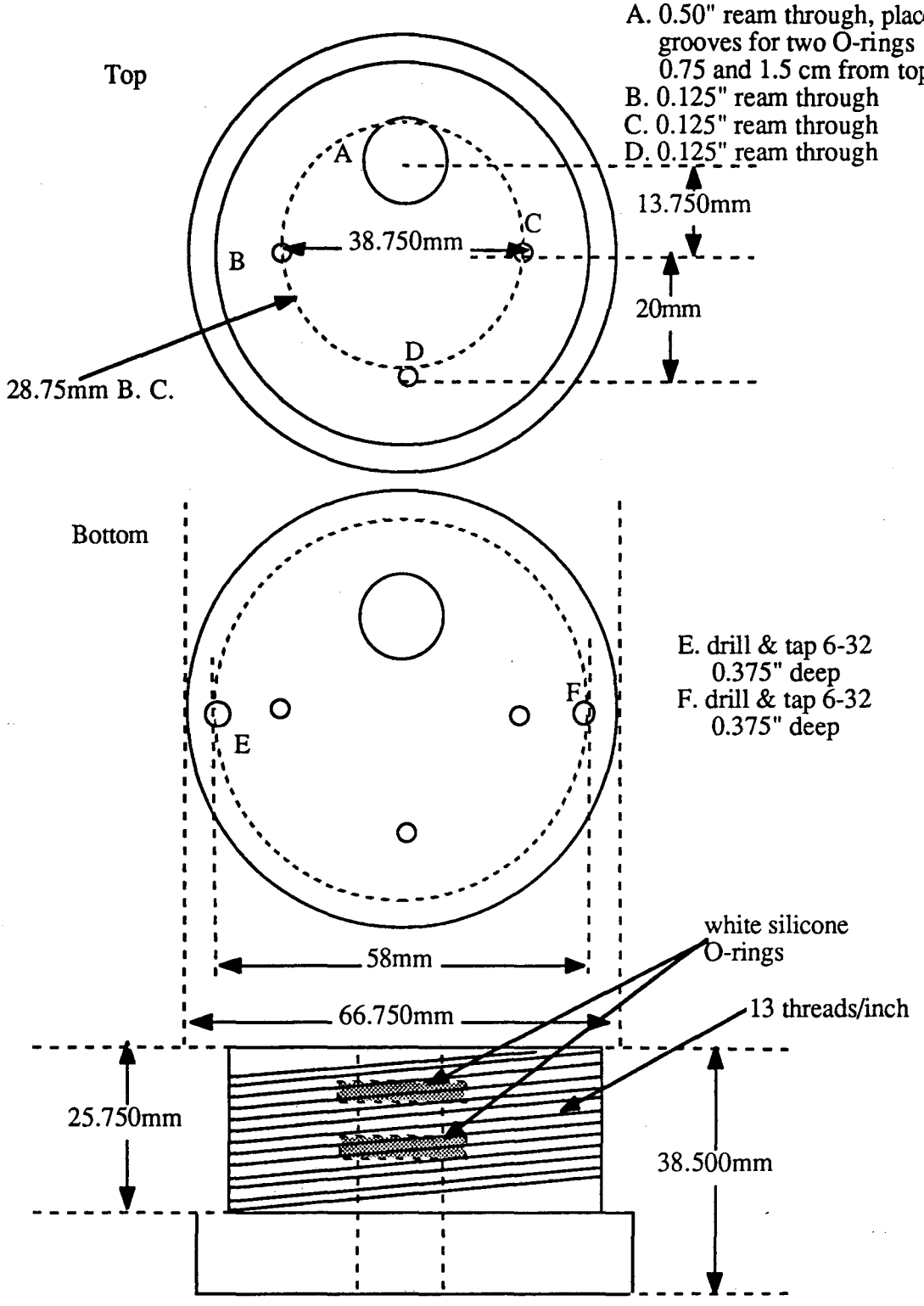

Figure A.4. Diagram of the macore base in the VT probe. "A" is for the transfer line, "B"&"C" are for the coax, "D" is for the thermometer and "E"&"F are for brass rods.

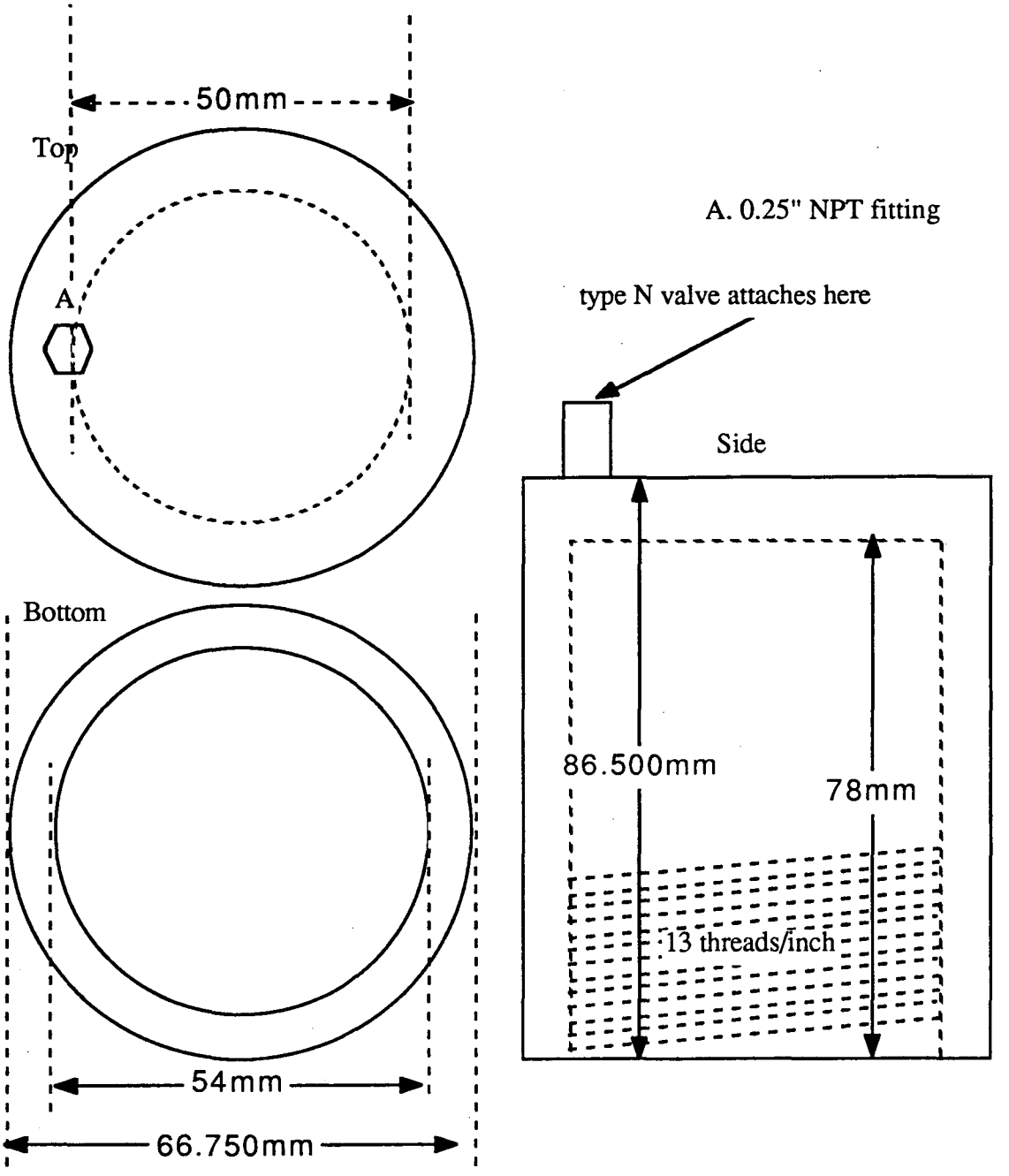

Figure A.5. Diagram of the 316 stainless steel dewar used in the VT probe. Dotted circle in top view is a bolt circle.

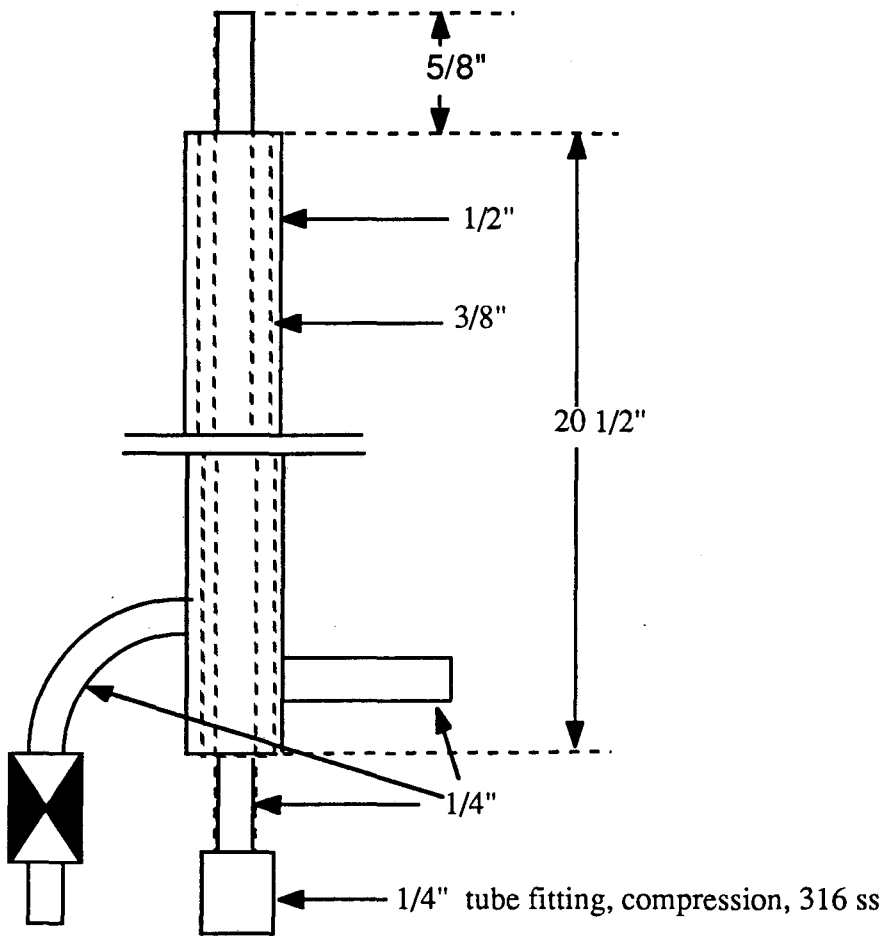

Figure A.6. Diagram of the 310 stainless steel transfer line used in the VT probe. 310 stainless steel contains no carbon, making it much easier to anneal and remove magnetic impurities from welding and working with machine tools. Cold gas enters through 1/4" tube in the center of the transfer line and flows out between the 1/4" and 3/8" tubes. The gap between the 3/8" and 1/2" tubes is maintained as a vacuum jacket.

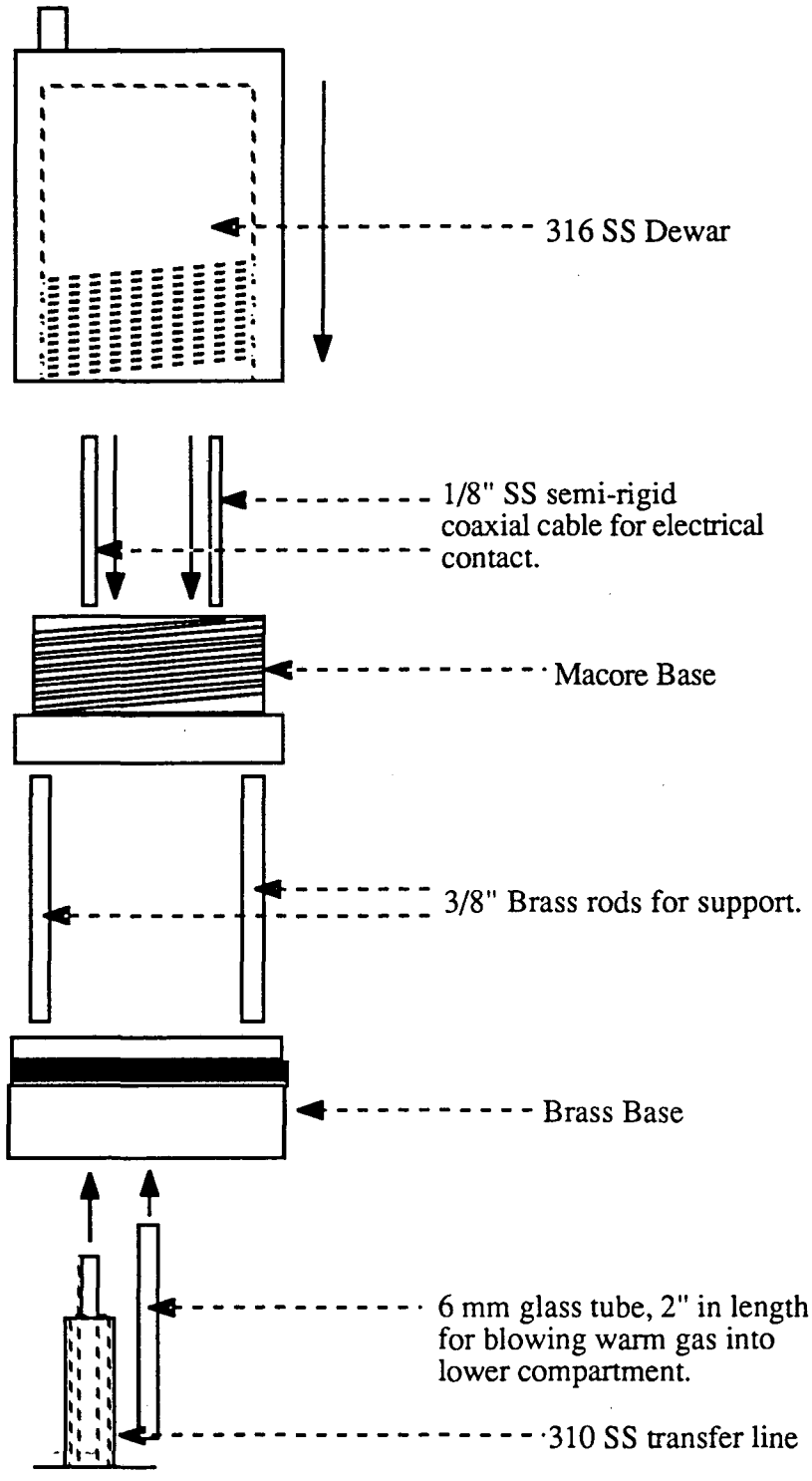

Figure A.7. VT probe head assembly. Tuned circuit components are not shown. Brass base design assumes use of polyflon tuning capacitor. RF shield (not shown) attaches to brass base and covers probe head.

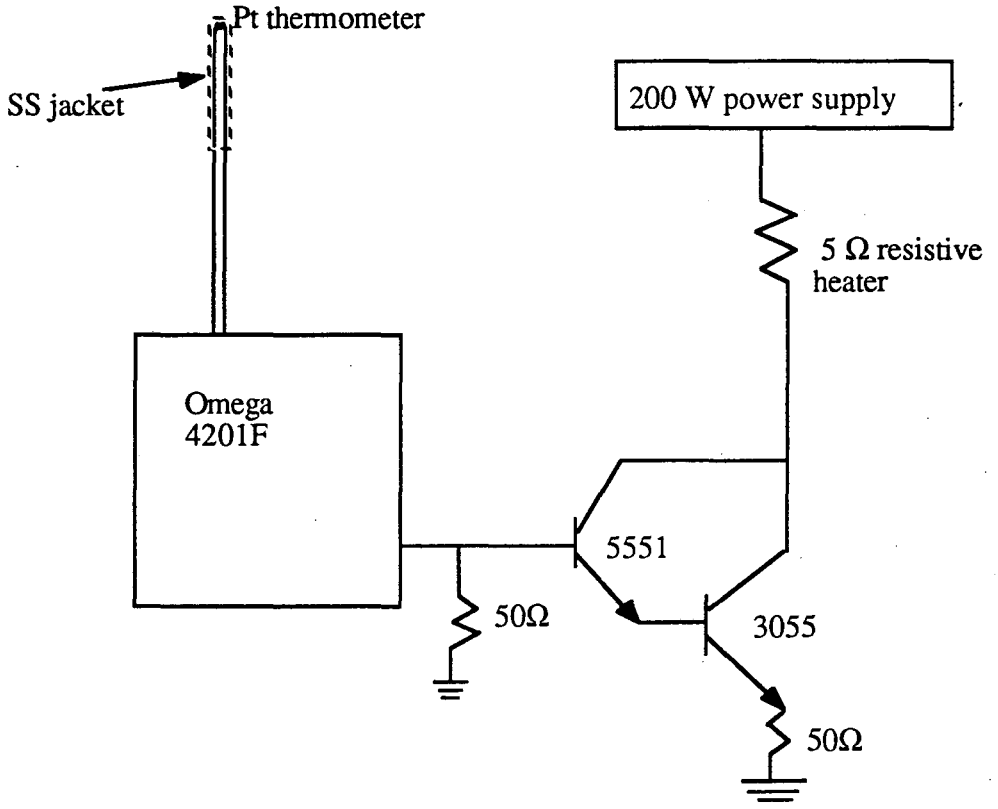

Figure A.8. Temperature control apparatus.

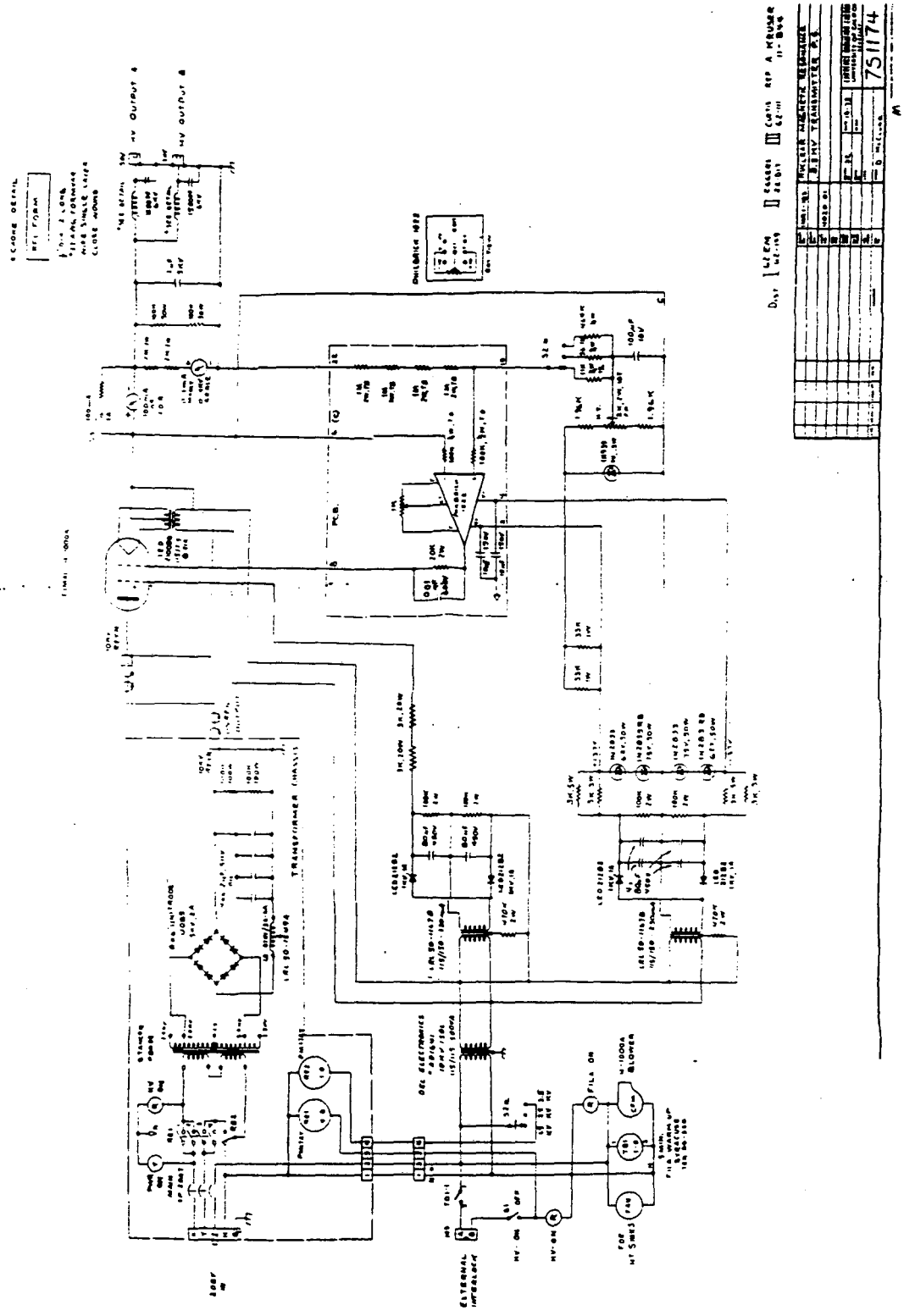

Figure A.9. High voltage power supply.

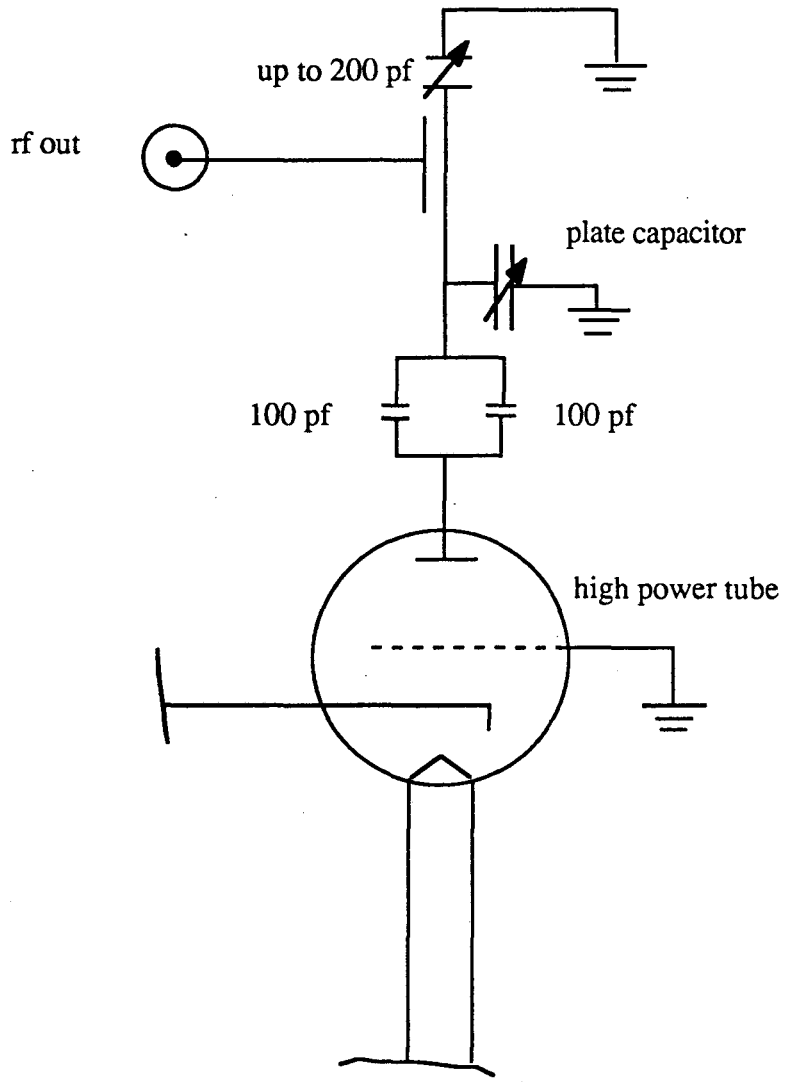

Figure A.10. Modifications to the Henry 1002 tuned rf amplifier. An ENI 4100L was used as the driver.

LAWRENCE BERKELEY LABORATORY
UNIVERSITY OF CALIFORNIA
INFORMATION RESOURCES DEPARTMENT
BERKELEY, CALIFORNIA 94720